DRY LIGHTNING IN THE WESTERN UNITED STATES: METEOROLOGICAL CONDITIONS, WILDFIRE IGNITION, AIR QUALITY IMPACTS, AND FUTURE PROJECTIONS

By

DMITRI A. KALASHNIKOV

A dissertation submitted in partial fulfillment of
the requirements for the degree of

DOCTOR OF PHILOSOPHY

WASHINGTON STATE UNIVERSITY
School of the Environment

MAY 2024

To the Faculty of Washington State University:

The members of the Committee appointed to examine the dissertation of DMITRI A. KALASHNIKOV find it satisfactory and recommend that it be accepted.

Deepti Singh, Ph.D., Chair

Kevan B. Moffett, Ph.D.

Von P. Walden, Ph.D.

Paul C. Loikith, Ph.D.

ACKNOWLEDGMENT

I wish to thank everyone who has helped me along my journey. I would like to start by thanking my advisor Dr. Deepti Singh. Dr. Singh skillfully balanced providing guidance with allowing me the freedom to explore my own research topics. Her trust in my skills really helped me excel, and I'm truly grateful for her support. Furthermore, her insistence on pushing me outside my comfort zone has been crucial to elevating my career to this point. I would like to thank all of the members of my lab, past and present, who were there to provide feedback that helped improve both my research and presentation skills. I would like to thank my numerous research collaborators for providing valuable feedback, as well as methodological and subject matter guidance. A special thank you to my committee members Drs. Kevan Moffett, Von Walden, and Paul Loikith, your guidance and feedback has been much appreciated. I would like to acknowledge and sincerely thank NASA for providing me the funding to undertake my Ph.D. research through the FINESST award. I would like to express my deepest gratitude to Christine Nguyen. Her love and unwavering support through the years inspired me to focus on my goals and allowed me to see this dissertation to its successful completion. This dissertation is dedicated to Christine and my two sons, Silas and Julian.

DRY LIGHTNING IN THE WESTERN UNITED STATES: METEOROLOGICAL CONDITIONS, WILDFIRE IGNITION, AIR QUALITY IMPACTS, AND FUTURE PROJECTIONS

Abstract

by Dmitri A. Kalashnikov, Ph.D.
Washington State University
May 2024

Chair: Deepti Singh

Cloud-to-ground lightning occurring with little to no rainfall – typically referred to as "dry lightning" – is a major source of wildfire ignition in the western United States (WUS) during summer months. Although lightning-caused wildfires occur naturally and are generally ecologically beneficial, changing climatic conditions are increasing the risk of large and severe wildfires. Motivated by these impacts, my dissertation aims to advance our understanding of dry lightning in the WUS and its associated meteorological conditions, wildfire ignitions, air quality impacts, and future projections. In the first chapter, I provide an overview of the motivations for undertaking this dissertation. In the second chapter, I use gridded air pollutant and population data to examine compound air pollution episodes in the WUS. This study demonstrates an increase in the co-occurrence of two harmful air pollutants (fine particulate matter and ground-level ozone) during the WUS wildfire season in the past two decades, and increasing population exposure to these co-occurrences of 25 million person-days per year largely driven by increasing wildfire activity. I show that the largest population exposure to co-occurring air pollution was

associated with the major outbreak of dry lightning that ignited hundreds of wildfires in California during August, 2020. To better understand dry lightning in this fire-prone region, in the third chapter I examine the meteorological and geographical factors associated with dry lightning in central and northern California. I apply *k*-means clustering to atmospheric reanalysis data to identify four types of meteorological patterns associated with the largest dry lightning outbreaks over this region, and quantify the spatial patterns of enhanced dry lightning risk associated with each pattern. In the fourth chapter, I use radar-derived rainfall data and gridded climatological variables to investigate the precipitation amounts and biophysical factors associated with lightning-caused wildfire ignitions across the WUS. Critically, my results refine the widely-used <2.5mm precipitation amount to define dry lightning by demonstrating that substantial regional variation exists in ignition-relevant precipitation amounts depending on local topography, vegetation, and climate. In the fifth chapter, I use Convolutional Neural Networks (CNNs) to predict cloud-to-ground lightning in the WUS at the grid cell level using a suite of reanalysis-derived meteorological variables as predictors. The CNNs are skillful at predicting lightning (domain-median AUC = 0.8) and realistically capture the year-to-year variation of lightning activity across the WUS (domain-median interannual correlation = 0.87). The CNN-based predictive models developed in this study can be applied to output from global climate models, thus enabling the ability to project future lightning and lightning-caused wildfires. In the final chapter, I summarize my findings from the four studies that comprise my dissertation. The outcomes of my research can be useful to forecasters and fire managers to anticipate possible wildfire ignitions in the present climate, and can be used to inform planning, management, and policy decisions around future lightning-caused wildfires in the WUS.

TABLE OF CONTENTS

Page

LIST OF TABLES

Page

LIST OF FIGURES

Page

CHAPTER ONE: INTRODUCTION

In the western United States (WUS), summertime thunderstorms are relatively rare and understudied compared to areas east of the Rocky Mountains. However, when these thunderstorms occur, they pose potential hazards ranging from flash flooding to wildfire ignition. In particular, "dry lightning" – defined as cloud-to-ground lightning occurring without significant accompanying rainfall – is a major wildfire ignition source across the WUS during summer months when fuels are seasonally dry, and account for the vast majority of burned area across the region. Furthermore, compared to most other areas of the world, dry lightning in the WUS represents a relatively large fraction of overall convective activity. This is due to the combination of mid-tropospheric moisture advection overlying a hot and dry lower troposphere that can evaporate rainfall before it reaches the ground. The lack of lower-tropospheric moisture outside of areas directly affected by the North American Monsoon generally suppresses summertime rainfall and fuel moisture thus posing an increased risk of wildfire ignition when thunderstorms do occur. A recent and prominent example is the major outbreak of dry lightning that occurred in central and northern California amid an ongoing drought in August of 2020, igniting numerous wildfires that ultimately contributed to the largest annual burned area in the state's modern history, with far-reaching air quality impacts due to smoke.

Although lightning-caused wildfires occur naturally and are generally ecologically beneficial, changing climatic conditions are increasing the risk of large and severe wildfires such as those in 2020. Consequently, these fires are more likely to produce negative impacts to ecosystems and society. Motivated by these impacts, my dissertation aims to advance our understanding of dry lightning in the WUS and its associated meteorological conditions, wildfire ignitions, air quality impacts, and future projections. In the second chapter, I use gridded air

pollutant and population data to examine summertime air pollution episodes in the WUS. Given the compounding human health impacts of air pollutant co-occurrences, I investigate the influence of wildfires and meteorological factors on the spatial and temporal characteristics of extreme $PM_{2.5}$/ozone co-occurrences across the WUS and assess the associated population exposure. Using gridded 1° x 1° datasets of observed $PM_{2.5}$ and ozone and atmospheric reanalyses, I (1) quantify trends in the frequency, persistence, and extent of widespread co-occurrence of $PM_{2.5}$/ozone extremes across the WUS in the past two decades, (2) identify the large-scale atmospheric patterns associated with widespread co-occurrences and population exposure, (3) examine trends in atmospheric patterns that amplify or mitigate co-occurrence risk across the region, and (4) investigate the relationship between the geographic extent of co-occurrence, wildfire activity and extreme heat during and preceding widespread $PM_{2.5}$/ozone co-occurrences. I also investigate these factors in the context of the exceptional widespread and long-lasting co-occurrence episode that resulted from the 2020 lightning-caused wildfires in California.

To better understand dry lightning in this fire-prone region, in the third chapter I examine the meteorological and geographical factors associated with dry lightning in central and northern California. In this study, I leverage three decades of gridded cloud-to-ground lightning and precipitation data (1987-2020) to compile the first long-term climatology of dry lightning for central and northern California. I utilize atmospheric reanalysis data to quantify the meteorological conditions that produce dry lightning and examine their differences compared to "wet" lightning. Due to their ability to produce widespread and costly wildfire outbreaks, I also analyze historical widespread dry lightning episodes and identify associated large-scale atmospheric patterns. As lightning climatology is strongly linked to topography in California, I

additionally explore the influence of elevation on dry lightning across this region. Understanding the characteristics and meteorological drivers of dry lightning is critical for anticipating fire ignitions in the present climate and for fully characterizing the changing risk of wildfires, including multiple fire ignitions, with ongoing and projected warming and drying in the region.

In the fourth chapter, I use radar-derived rainfall data and gridded climatological variables to investigate the precipitation amounts and biophysical factors associated with lightning-caused wildfire ignitions across the WUS between 2015-2020. Some lightning-caused wildfires are not discovered for multiple days or weeks following ignition and are known as "holdover" fires. For example, the 2021 Bootleg Fire in Oregon smoldered for more than one week before detection and ultimately grew into the state's third-largest wildfire on record. Such holdover fires might be associated with different environmental conditions and precipitation amounts. I therefore investigate ignition precipitation amounts and environmental conditions associated with holdover lightning-caused wildfires separately from those lightning-caused wildfires that were detected promptly. My findings advance the understanding of factors affecting lightning-caused wildfire risk and are relevant to wildland fire prediction, suppression, and management across WUS sub-regions.

In the fifth chapter, I use Convolutional Neural Networks (CNNs) to predict cloud-to-ground lightning in the WUS at the grid cell level using a suite of reanalysis-derived meteorological variables as predictors. By developing individual CNNs at each grid cell and predicting cloud-to-ground lightning at the daily scale, my approach offers two primary advantages over traditional lightning parameterization methods. *First*, my targeted approach provides refined spatial and temporal resolution compared to parameterization methods that assessed bulk lightning activity at national to global scales and at monthly to annual aggregation.

My strategy of developing predictor models at each grid cell is better suited for the WUS, since lightning climatology and associated meteorological patterns can vary considerably over short distances due to spatial heterogeneity of the terrain. *Second*, most previous studies have parameterized total lightning flash rate (including intra-cloud and cloud-to-ground) and occasionally estimated cloud-to-ground lightning in future projections using empirically-derived ratios. To reduce uncertainty, I train CNNs to explicitly predict cloud-to-ground lightning as only this type of lightning poses the risk of wildfire ignition. The CNN-based predictive models developed in this study can be applied to output from global climate models to predict lightning occurrence in the future based on the projected meteorological patterns, thus enabling the ability to project future lightning and lightning-caused wildfires.

In the final chapter, I summarize my findings from the four studies that comprise my dissertation. The outcomes of my research can be useful to forecasters and fire managers to anticipate possible wildfire ignitions in the present climate, and can be used to inform planning, management, and policy decisions around future lightning-caused wildfires in the WUS.

CHAPTER TWO: INCREASING CO-OCCURRENCE OF FINE PARTICULATE MATTER AND GROUND-LEVEL OZONE EXTREMES IN THE WESTERN UNITED STATES

Kalashnikov, D. A., Schnell, J. L., Abatzoglou, J. T., Swain, D. L., & Singh, D. (2022). Increasing co-occurrence of fine particulate matter and ground-level ozone extremes in the western United States. *Science Advances*, *8*(1), eabi9386. DOI: 10.1126/sciadv.abi9386

Originally published in *Science Advances* and reproduced here in its original format.

Attributions:

Dmitri A. Kalashnikov designed the research, performed all analyses, and wrote the manuscript. D. Singh provided supervision and research direction, and helped edit the manuscript. J.L. Schnell provided the air quality datasets used in this study, provided feedback on the research, and helped edit the manuscript. J.T. Abatzoglou and D.L. Swain provided feedback on the research and helped edit the manuscript.

Abstract:

Wildfires and meteorological conditions influence the co-occurrence of multiple harmful air pollutants including fine particulate matter ($PM_{2.5}$) and ground-level ozone. We examine the spatiotemporal characteristics of $PM_{2.5}$/ozone co-occurrences and associated population exposure in the western U.S. The frequency, spatial extent, and temporal persistence of extreme $PM_{2.5}$/ozone co-occurrences have increased significantly between 2001-2020, increasing annual population exposure to multiple harmful air pollutants by ~25 million person-days/year. Using a clustering methodology to characterize daily weather patterns, we identify significant increases in atmospheric ridging patterns conducive to widespread $PM_{2.5}$/ozone co-occurrences and population exposure. We further link the spatial extent of co-occurrence to the extent of extreme heat and wildfires. Our results suggest an increasing potential for co-occurring air pollution episodes in the western US with continued climate change.

INTRODUCTION

Air pollution is an urgent global health problem, and one that has gained additional attention during the COVID-19 pandemic due to the exacerbating effects of pollutant exposure on infectious disease spread and mortality (*1-3*). Two main air pollutants - fine particulate matter ($PM_{2.5}$, defined as particulate matter with diameter of ≤2.5 μm), and ground-level ozone (hereafter, 'ozone') - are linked to significant human health concerns including cardiovascular and respiratory illnesses and mortality (*4–7*). $PM_{2.5}$ and ozone have also been linked to negative ecosystem impacts via their detrimental effects on plants and the broader environment (*8–10*). Although few studies have quantified the compounding health impacts of co-occurring $PM_{2.5}$ and ozone, existing research indicates that simultaneous exposure to both pollutants can have disproportionately more severe health impacts beyond the individual effect of either pollutant (*11*, *12*).

Wildfires can cause simultaneous increases in both pollutants through the direct emission of $PM_{2.5}$ (*13*, *14*) and ozone precursor compounds (*15–18*) in smoke plumes, and recent research has shown that ozone concentrations in urban areas in the western United States (US) can be enhanced in the presence of wildfire smoke (*19-21*). During years of limited wildfire activity, most of the western US experienced annual maximum $PM_{2.5}$ concentrations during the cool season when stagnant air conditions are typically prevalent (*22*). This seasonality would typically minimize co-occurrence risk with high ozone concentrations, which peak during the warm season when hot and dry conditions facilitate the formation and build-up of ozone (*23*). Summertime wildfires therefore present a mechanism for $PM_{2.5}$ extremes to occur at a time of year when ozone levels are seasonally high, leading to increased chances of elevated concentrations of both air pollutants occurring simultaneously.

Smoke from the unprecedented wildfire activity in the western US during August and September of 2020 contributed to several weeks of extremely hazardous air quality over a large area (*3*, *24*). Similar conditions, although on a smaller scale, occurred during the 2015, 2017 and 2018 wildfire seasons (*25*, *26*), and extensive wildfire smoke affected the region again in 2021. Such widespread hazardous conditions acutely affected vulnerable communities in the region – those at enhanced risk due to socio-economic or demographic factors and underlying health conditions – contributing to an increased burden on the healthcare system through increased hospitalizations and emergency department visits (*26*). In addition, recent research has linked wildfire smoke in 2020 to higher risk and mortality associated with COVID-19 in many western states (*3*). As recurrent and prolonged exposure to air pollution can exacerbate the public health impacts of wildfire smoke (*27–31*), recent wildfire seasons have thus raised significant concerns regarding the trajectory of air quality in the region.

Historical and projected climate and wildfire trends in the western US both point toward increasing risk of exposure to poor air quality. Increased wildfire activity has already contributed to rising extreme $PM_{2.5}$ concentrations in fire-prone regions of the western US (*32*, *33*), offsetting national-level air quality improvements following the Clean Air Act. Indeed, wildfires have contributed up to 50% of annual $PM_{2.5}$ in parts of the western US in recent years (*34*). Annual burned area across the western US has experienced exponential growth in recent decades (*35*, *36*), partially due to drying of vegetation in the region tied to anthropogenic climate change (*37–39*). These observed trends are projected to continue in a warming climate (*24*, *40–42*).

Long-term climate and daily-scale meteorological conditions both influence the formation, accumulation, and transport of air pollutants. Large-scale high-pressure systems (or 'ridges') during the summer enhance surface temperatures, promote air stagnation, and can

contribute to both increased wildfire activity and ozone production in the western US (*23*). Previous work has shown that such high-pressure systems are expected to increase in frequency and persistence due to climate change (*43*, *44*), raising the potential for increased warm-season co-occurrence of $PM_{2.5}$/ozone extremes in the future. These conditions are amplified in the western US by topography that promotes air stagnation in populated regions adjacent to fire-prone lands (e.g. the Los Angeles Basin and the Willamette Valley near Portland).

Despite rising public health and air quality concerns, the influence of increasing wildfire activity and changing meteorology on widespread hazardous air quality conditions across the geographic extent of the western US has not yet been investigated. Schnell and Prather (*45*) systematically demonstrated the influence of meteorology on the co-occurrence of $PM_{2.5}$, ozone, and temperature extremes over eastern North America. Western North America, however, has fundamentally different seasonality and drivers of these pollutants, and previous studies investigating air pollutant co-occurrences have been restricted to urban areas [e.g. (*19-21*)]. Understanding how regional factors influence air pollutant characteristics and contribute to their changing risks is critical for assessing their public health impacts and anticipating future trends associated with climate variability and change.

Given the compounding human health impacts of air pollutant co-occurrences, we investigate the influence of wildfires and meteorological factors on the spatial and temporal characteristics of extreme $PM_{2.5}$/ozone co-occurrences across the western US and assess the associated population exposure. Using gridded 1° x 1° datasets of observed $PM_{2.5}$ and ozone developed by Schnell et al. (*46*) and atmospheric reanalyses, we (1) quantify trends in the frequency, persistence, and extent of widespread co-occurrence of $PM_{2.5}$/ozone extremes across the western US in the past two decades, (2) identify the large-scale atmospheric patterns

associated with widespread co-occurrences and population exposure, (3) examine trends in atmospheric patterns that amplify or mitigate co-occurrence risk across the region, and (4) investigate the relationship between the geographic extent of co-occurrence, wildfire activity and extreme heat during and preceding widespread $PM_{2.5}$/ozone co-occurrences. We also investigate these factors in the context of the exceptional widespread and long-lasting co-occurrence episode during the record-breaking 2020 wildfire season.

RESULTS

Increasing trends in the spatial and temporal characteristics of $PM_{2.5}$/ozone co-occurrence

Extremes in individual air pollutant concentrations are defined at each grid cell as exceedances of their annual 90th percentiles (~37 days each year). We find that the simultaneous, spatially co-located occurrence of local $PM_{2.5}$ and ozone extremes (hereafter 'co-occurrence') has become significantly more frequent over large areas of the western US during the late-summer wildfire season - July-September - between 2001-2020, driven largely by the changing seasonality of extreme $PM_{2.5}$ concentrations (Fig. 1). High $PM_{2.5}$ concentrations typically peaked during cool-season months across much of this region during the early 2000s (Fig. S1A). However, the fraction of the annual $PM_{2.5}$ extremes occurring during July-September has increased significantly in the past two decades (Fig. 1B). Parts of the region experienced a >80% increase in this fraction, indicating that in these grid cells a majority of $PM_{2.5}$ extremes are now concentrated during this season that previously rarely experienced $PM_{2.5}$ extremes. In contrast, ozone concentrations typically peak during warm-season months (Fig. S1C-D) and the fraction of annual ozone extremes occurring during July-September remains largely unchanged with the exception of small decreases over parts of the Rocky Mountains, High Plains, and coastal

California (Fig. 1C). Therefore, the increased occurrence of $PM_{2.5}$ extremes during a time of year when ozone concentrations are seasonally high has largely driven the observed increases in $PM_{2.5}$/ozone co-occurrence during the late-summer wildfire season across the western US (Fig. 1A).

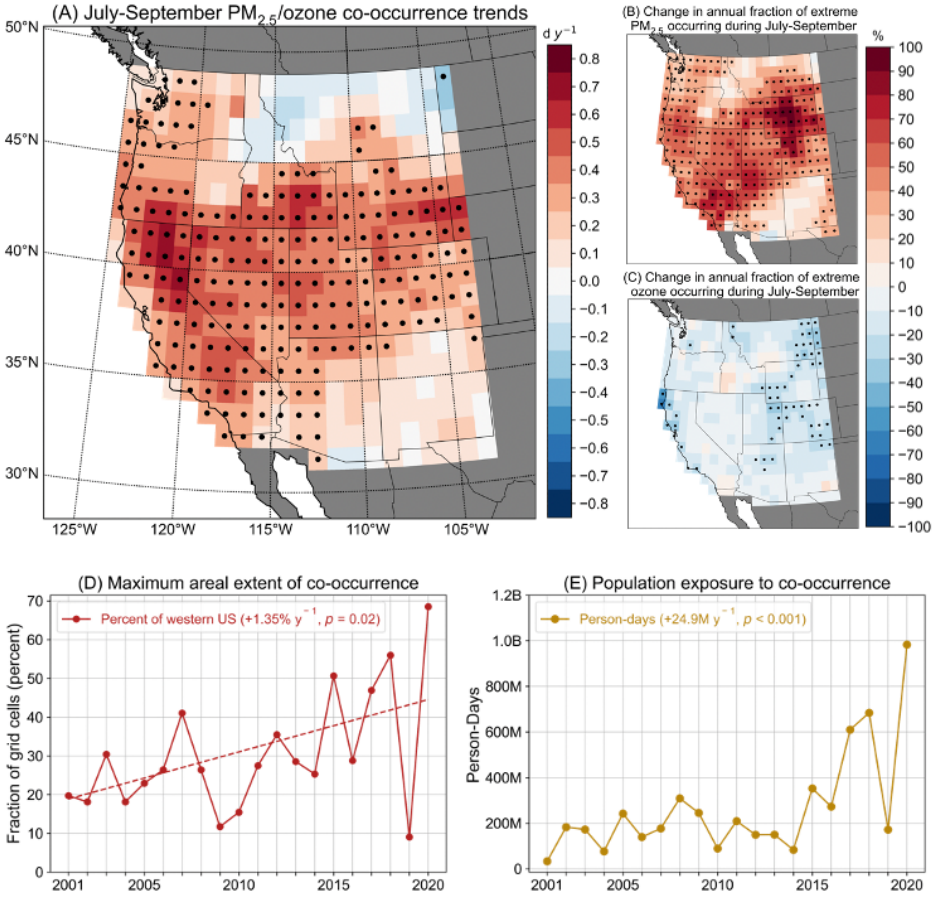

Fig. 1. $PM_{2.5}$/ozone co-occurrence trends during 2001-2020 and population exposure. (A) Trends in the number of days (d y^{-1}) with $PM_{2.5}$/ozone co-occurrences at each grid cell during July-September. Co-occurrences are defined as values of each pollutant exceeding their respective local annual 90th percentile daily concentrations simultaneously. Trends in the annual fraction of (B) $PM_{2.5}$ extremes and (C) ozone extremes occurring at each grid cell during July-September relative to rest of year (October – June). The maximum possible number of co-occurrences is 37 per year in each grid cell, equal to the number of days above local annual 90th percentile daily concentration values for each pollutant. Black dots denote statistical significance of trends at $p < 0.05$ based on a non-parametric permutation test. (D) Maximum daily extent of western US grid cells simultaneously experiencing co-occurrences of local $PM_{2.5}$/ozone extremes during July-September each year. (E) Total

population exposure to all local $PM_{2.5}$/ozone co-occurrences during July-September measured in million person-days (M) per year. Text in panels (D) and (E) indicates the linear trends and *p*-values based on a permutation test.

In addition to occurring more frequently, local $PM_{2.5}$/ozone co-occurrences are increasingly occurring across a larger geographic region simultaneously. The maximum daily fraction of western US grid cells with simultaneous $PM_{2.5}$/ozone co-occurrence during July-September has more than doubled (from 18.9% to 44.6%) over the past two decades, with an increasing trend of ~1.35% per year (*p-value* = 0.02) (Fig. 1D). The largest spatial extents of co-occurrence were observed in 2015, 2017, 2018 and 2020 – coincident with hot, dry summers and widespread fire activity, including the largest burned areas across the western US wildland-urban interface (*20*, *24, 25*, *29*, *36*, *47*). Increases in the frequency and spatial extent of co-occurrences are associated with an increasing trend in July-September population exposure of ~24.9 million person-days per year (*p-value* < 0.001) in the western US during 2001-2020 (Fig. 1E). Cumulative population exposure over the season to $PM_{2.5}$/ozone co-occurrences exceeded 600 million person-days during the 2017, 2018, and 2020 wildfire seasons (Fig. 1E). Daily population exposure exceeded 35 million people during the most widespread air pollution conditions in these three seasons, peaking at ~46 million people (>50% of the western US population) on August 21st, 2020 (Table S1).

Widespread $PM_{2.5}$/ozone co-occurrences, defined as days on which at least 25% of grid cells covering the western US simultaneously experience local $PM_{2.5}$/ozone co-occurrence, have occurred almost exclusively during July-September (72 of 75 total days; Fig. S2). Widespread co-occurrences have become significantly more frequent and persistent (Fig. 2A-B), with an increase of ~12.4 widespread co-occurrence days over 2001-2020 and the longest consecutive-day occurrence persisting for an additional ~6.2 days. The frequency of widespread co-

occurrences was highest during the recent active wildfire seasons (Fig. 2A; Fig. S3). Of the 72 July-September widespread co-occurrence days during 2001-2020, 59 occurred during 2015, 2017, 2018, and 2020. In addition, the longest persistence (12 consecutive days) of widespread $PM_{2.5}$/ozone co-occurrences on record occurred in 2020 (Fig. 2B), during which the daily maximum extent of co-occurrence peaked at ~68.5% of the western US on August 24th, 2020 (Fig. 1D; Table S1).

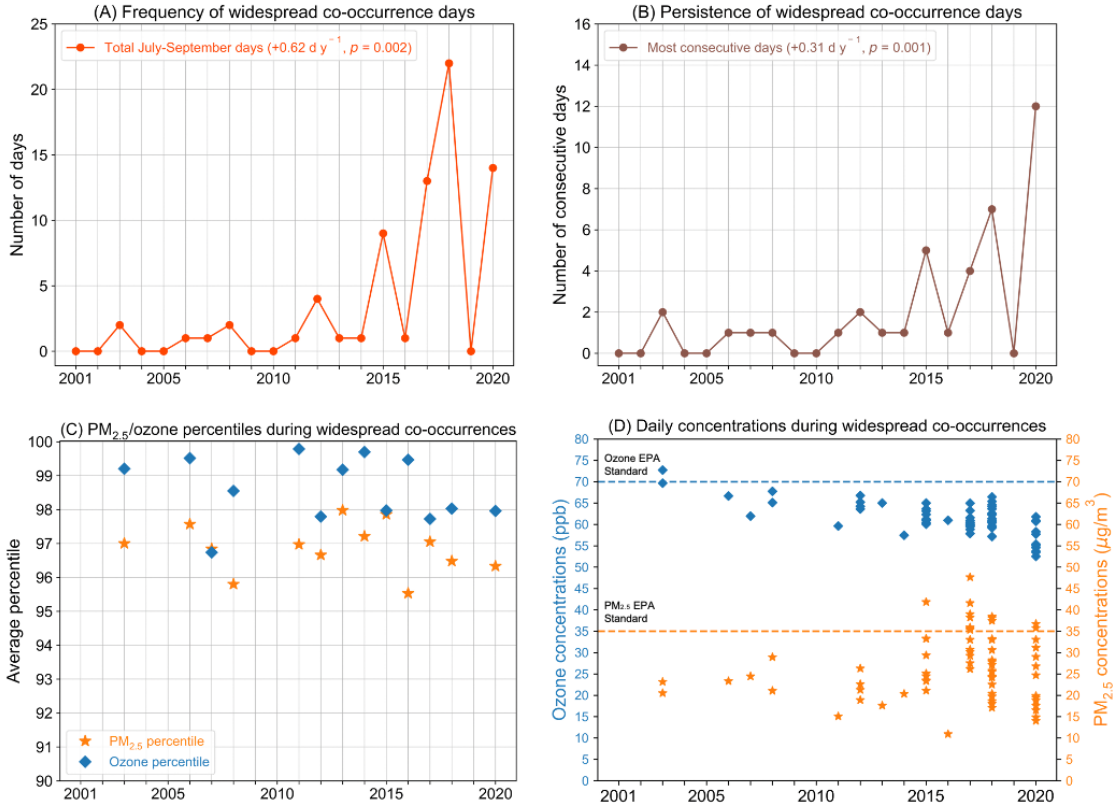

Fig. 2. Widespread $PM_{2.5}$/ozone co-occurrences. Timeseries of (A) the total number and (B) longest consecutive-day persistence of widespread July-September co-occurrence days, defined as days with simultaneous local $PM_{2.5}$/ozone co-occurrence in ≥25% of western US grid cells. Text in panels (A) and (B) indicates linear trends (d y^{-1}) with *p*-values based on a permutation test. Characteristics of the individual pollutants during widespread co-occurrences are shown through (C) percentiles of $PM_{2.5}$ and ozone daily concentrations averaged across all affected grid cells, and (D) pollutant concentrations averaged across affected grid cells on widespread co-occurrence days (*n* = 72). Note percentiles in panel (C) are calculated based on the distribution of concentrations in each year (refer to *Materials*

***and Methods)*. Dashed lines in panel (D) show concentrations corresponding to the EPA regulatory health standards for each pollutant (70 ppb for ozone and 35 μg/m^3 for $PM_{2.5}$).**

During widespread co-occurrences the concentrations of both pollutants are elevated relative to co-occurrence conditions of smaller geographic extent. Although co-occurrences are defined as values above the local, annual 90th percentiles for both $PM_{2.5}$ and ozone in each grid cell, average observed concentrations on all widespread co-occurrence days exceeded the 95th percentile for $PM_{2.5}$ and the ~97th percentile for ozone across all grid cells experiencing local $PM_{2.5}$/ozone co-occurrence (Fig. 2C). These findings are consistent with Schnell and Prather (*45*), who reported enhancements in $PM_{2.5}$ and ozone concentrations over eastern North America during large, multi-day pollution episodes well above the statistical thresholds used to define individual extremes (e.g. 90th or 95th percentiles). During widespread co-occurrence days in recent seasons (2015, 2017, 2018, and 2020), $PM_{2.5}$ concentrations averaged across all constituent grid cells experiencing $PM_{2.5}$/ozone co-occurrence exceeded the EPA regulatory limit of 35 μg/m^3 on 13 individual days (Fig. 2D, orange markers), peaking at 47.7 μg/m^3 on September 3rd, 2017 during a period of widespread fire activity and smoke conditions in the western US (*25*). Ozone concentrations averaged across the same grid cells on these days (n = 13) ranged from 57-63 ppb (Fig. 2D, blue markers; see also Fig. S4 for average concentrations during all co-occurrences). Although below the EPA regulatory limit of 70 ppb, the fact that such high ozone concentrations were present when averaged over a large geographic area and for prolonged periods in combination with widespread $PM_{2.5}$ regulatory exceedances illustrates the magnitude of human and environmental exposure to harmful air pollutants during recent wildfire seasons, the health impacts of which are emerging (*3*, *26*, *30*, *31*).

Increasing trends in atmospheric patterns conducive to co-occurrence

Although wildfires are a key source of emissions of $PM_{2.5}$ and ozone precursor compounds during the late-summer season, the spatial extent, local concentrations, and temporal persistence of their co-occurrences are modulated by a suite of meteorological factors, including surface temperature and atmospheric patterns (*45*). To understand if and how atmospheric patterns that affect $PM_{2.5}$/ozone co-occurrence characteristics are changing, we use a spatial clustering approach known as Self-Organizing Maps (SOMs) (*48*, *49*). Our SOM implementation categorizes daily large-scale weather patterns during July-September into 12 representative clusters (or 'nodes') based on 500-hPa geopotential height anomalies from the European Centre for Medium-Range Weather Forecasts (ECMWF) ERA5 reanalysis product (1979-2020; refer to *Materials and Methods*).

Table 1. Summary statistics for all 12 nodes of the Self-Organizing Map (SOM).
$PM_{2.5}$/ozone co-occurrence data represents all July-September days from 2001-2020. Asterisks indicate statistical significance of node trends (1979-2020) at $p < 0.05$.

SOM Node	Number of Days	Cumulative $PM_{2.5}$./ozone co-occurrence exposure in million person-days	Number of widespread $PM_{2.5}$/ozone co-occurrence days ($n = 72$)	42-year change in SOM node frequency (days/year)	42-year change in maximum SOM node persistence (consecutive days/year)
1	151	441.7	5	-1.1	-0.6
2	98	78.2	0	-6.4*	-3.5*
3	130	77.9	0	-2.0	-0.2
4	63	4.4	0	-4.2*	-1.7
5	217	835.7	14	5.8*	1.2
6	198	529.2	6	0.0	-0.1
7	251	650.8	8	2.7	0.7
8	110	122.6	2	-2.2	-1.0
9	129	866.7	16	2.2	0.6
10	194	847.2	13	6.2*	2.1*
11	179	739.5	8	2.8	0.6
12	120	141.0	0	-3.7	-0.7

We quantify the number of widespread co-occurrence days and population exposure to co-occurrence associated with each node (Table 1; Fig. S5), and identify the 6 SOM nodes with the largest (Nodes 5, 9 and 10, hereafter 'high-exposure nodes') and smallest (Nodes 2, 3, and 4,

hereafter 'low-exposure nodes') $PM_{2.5}$/ozone co-occurrence risk (Fig. 3). High-exposure nodes are characterized by widespread positive geopotential height anomalies (hereafter, 'ridging') and high daily maximum surface temperature anomalies across the region, which are largely co-located with those grid cells experiencing the highest number of local $PM_{2.5}$/ozone co-occurrences during widespread co-occurrence days in that node (Fig. 3A-C). In contrast, low-exposure nodes are characterized by widespread anomalously low geopotential heights, cooler temperatures, and onshore airflow from the Pacific Ocean, providing critical natural ventilation for this region and suppressing widespread co-occurrence risk (Fig. 3D-F) (*50*).

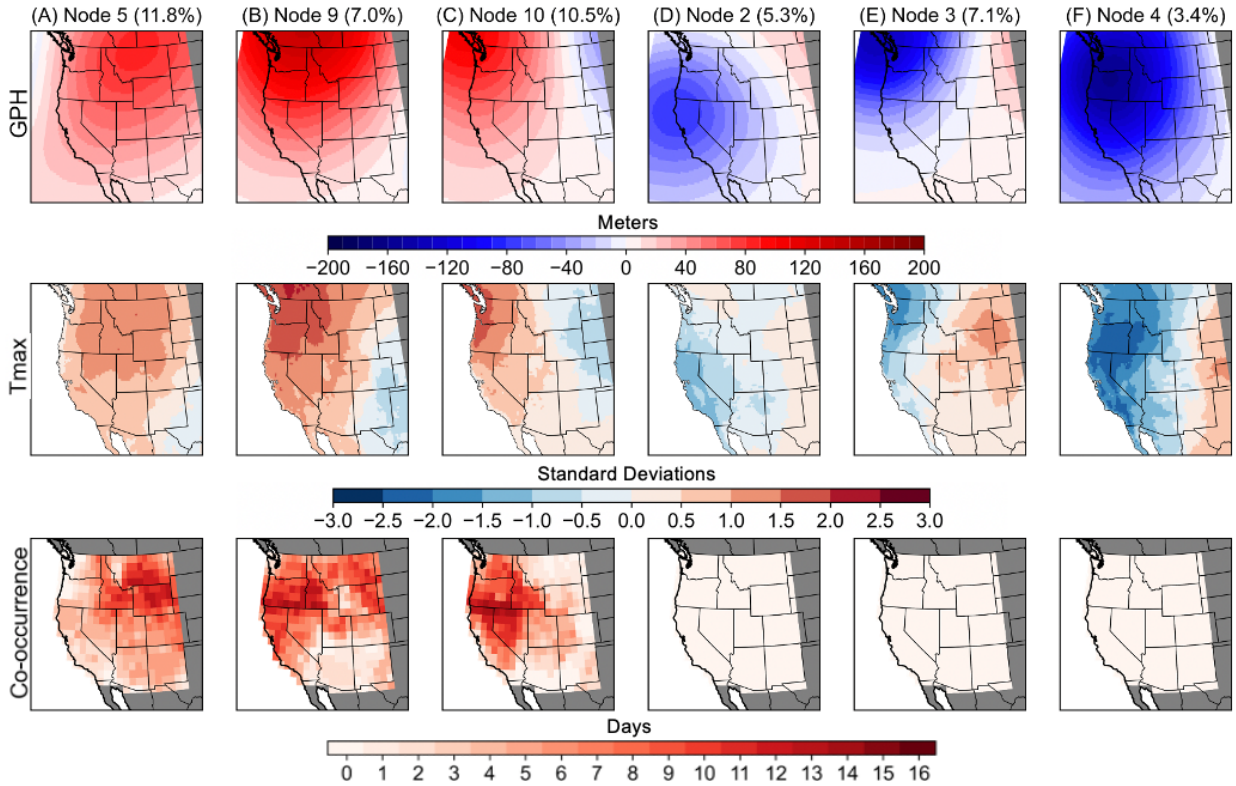

Fig. 3. The 6 SOM nodes with the largest (left three columns) and smallest (right three columns) $PM_{2.5}$/ozone co-occurrence risk. (Top) Geopotential height (GPH) anomalies for each SOM node trained over 1979-2020. (Middle) Composite standardized anomalies of daily maximum temperatures (Tmax) on all days associated with each node during the 2001-2020 period. (Bottom) Number of times each grid cell experienced local $PM_{2.5}$/ozone co-occurrences during all widespread co-occurrence days associated with that node. The

maximum possible number of co-occurrence days in a given grid cell is equivalent to the total number of widespread co-occurrence days associated with that node (Node 5: 14 days, Node 9: 16 days, Node 10: 13 days; Table 1). Values in parentheses on top row indicate the frequency of each SOM node relative to all July-September days during the period of overlap with air pollution data (2001-2020).

Large-scale atmospheric patterns represented by high-exposure nodes contributed 43 of the 72 widespread co-occurrence days (~60%), despite accounting for only ~29% of all July-September days since 2001, indicating an elevated risk of $PM_{2.5}$/ozone co-occurrence across the region when such patterns occur. We find robust increases in the frequency and persistence of high-exposure nodes since 1979. These nodes now occur on an additional ~14.2 days per year during July-September (*p-value* < 0.001) and the longest persistence of these nodes is an additional ~4.3 consecutive days longer (*p-value* = 0.008) compared to four decades ago (Fig. 4, orange lines). While the frequency of nodes relates to the frequency of pollutant exposure, the longer persistence of certain nodes can have additional impacts beyond that of single-day node occurrences. For example, previous research has shown that high ozone concentrations are more likely during prolonged, multi-day heat conditions than on single hot days (*22*, *45*). Of the 29 remaining widespread co-occurrence days not associated with the high-exposure nodes, 21 occurred in conjunction with atmospheric patterns favorable for widespread smoke transport across the region during periods of high wildfire activity (Nodes 1, 7 and 11; see Table 1 and Fig. S5). In contrast to the high-exposure nodes, the combined frequency and multi-day persistence of low-exposure nodes exhibit negative trends during 1979-2020, now occurring on ~12.6 fewer days per year (*p-value* < 0.001) and the longest consecutive-day occurrence of these nodes persisting for ~4.3 fewer days (*p-value* = 0.002) compared to four decades ago (Fig. 4, blue lines).

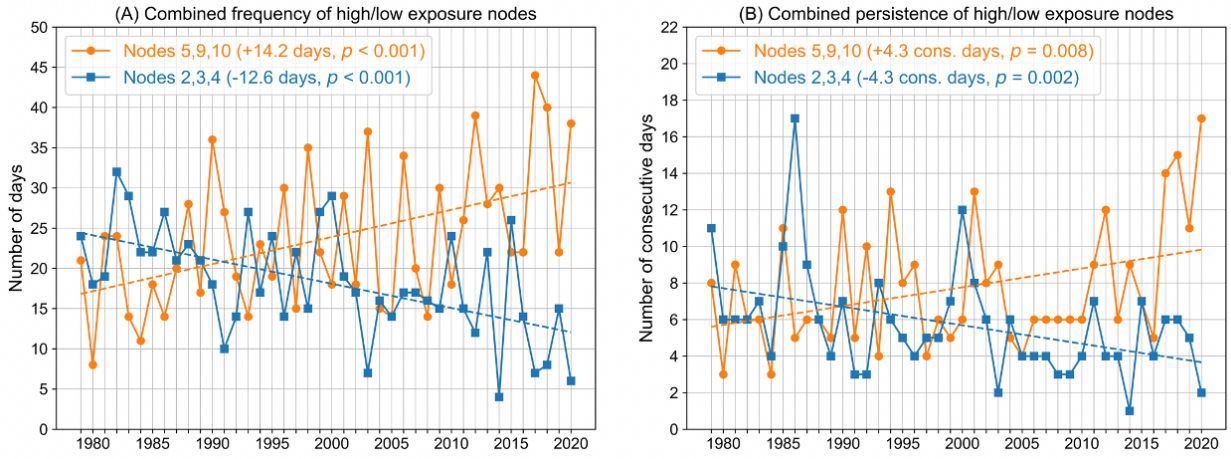

Fig. 4. Frequency and persistence of high/low exposure nodes. Timeseries of combined (A) total number of days and (B) longest multi-day persistence for high-exposure SOM nodes 5, 9, 10 (orange lines) and low-exposure SOM nodes 2, 3, 4 (blue lines), during July-September 1979-2020. In both plots, dashed lines show linear trends with numbers indicating corresponding changes over the 42-year period and *p*-values of the linear trends based on a permutation test.

Together, these results suggest that atmospheric patterns that are conducive to widespread local $PM_{2.5}$/ozone co-occurrences and larger population exposure across the western US are becoming more frequent and persistent during July-September. Recent active wildfire seasons have occurred in conjunction with record frequency and persistence of the high-exposure nodes (i.e. ridging), with the highest frequency since 1979 of 44 days observed in July-September 2017 and longest persistence of 17 consecutive days observed from September 3rd-19th, 2020 occurring simultaneously with historic wildfire activity across several western US states (Fig. 4) (*24*). The observed increase in ridging has co-occurred with and likely amplified increasing aridity and extent of wildfire burned area over the western US at least partially associated with anthropogenic warming, posing compounding hazards to the region (*37-39*, *51*). Further, increased persistence of ridging during wildfire smoke conditions can exacerbate ground-level pollution in topographically-constrained basins, as decreased sunlight and increased

atmospheric stability traps smoke and prolongs the air pollution conditions (*52*, *53*). Conversely, atmospheric patterns favoring decreased widespread $PM_{2.5}$/ozone co-occurrences across the western US (i.e. negative geopotential height anomalies and onshore airflow) are appearing less often and with shorter duration during the late-summer wildfire season.

Case study: Widespread co-occurrence episode of August 2020

The 'exceptional' 2020 wildfire season featured the second highest number of widespread $PM_{2.5}$/ozone co-occurrence days across the domain, along with the longest consecutive-day persistence of widespread co-occurrence (Fig. 2A-B), the single most widespread daily co-occurrence extent (~68.5%) across the western US (Fig. 1D), and the highest cumulative seasonal population exposure to all local $PM_{2.5}$/ozone co-occurrences of nearly 1 billion person-days (Fig. 1E) in the 20-year observed record. Widespread wildfire activity and extreme temperatures associated with atmospheric ridging both contributed to shaping the record multi-day co-occurrence episode observed during the second half of August 2020 (Fig. 5).

To examine their influence in shaping the multi-day widespread air pollution episode, we analyze the wildfire and meteorological conditions between August 15th and 29th, 2020. We find a sharp increase in the spatial extent of locally defined $PM_{2.5}$/ozone co-occurrences immediately following a peak in daily burned area aggregated over the western US and southwest Canada (brown line, Fig. 5A). This increase in burned area was associated with an extremely anomalous dry lightning outbreak that ignited hundreds of wildfires, leading to multiple large fires that burned for several weeks in central and northern California (Fig. 5B) (*24*). Grid cells in large areas of the interior western US, both near and downwind of fires, observed $PM_{2.5}$/ozone co-occurrences on a majority of days (>7) during this 15-day period (Fig. 5B, shading). The grid

cells that experienced a high number of co-occurrences are largely co-located with areas where wildfire smoke persisted during that period, which is identified by the National Oceanic and Atmospheric Administration's (NOAA) Hazard Mapping System (HMS) smoke product (Fig. 5B, contours). Notably, grid cells in northern Nevada immediately downwind of California fires observed local $PM_{2.5}$/ozone co-occurrences on at least 12 days and smoke was observed on at least 13 days of the 15-day episode. In addition, many grid cells in the interior western US observed record warmest 15-day average of daily maximum temperatures since 1979, conditions that likely enhanced ozone production and contributed to the widespread extent of $PM_{2.5}$/ozone co-occurrences (Fig. 5C) (*23*).

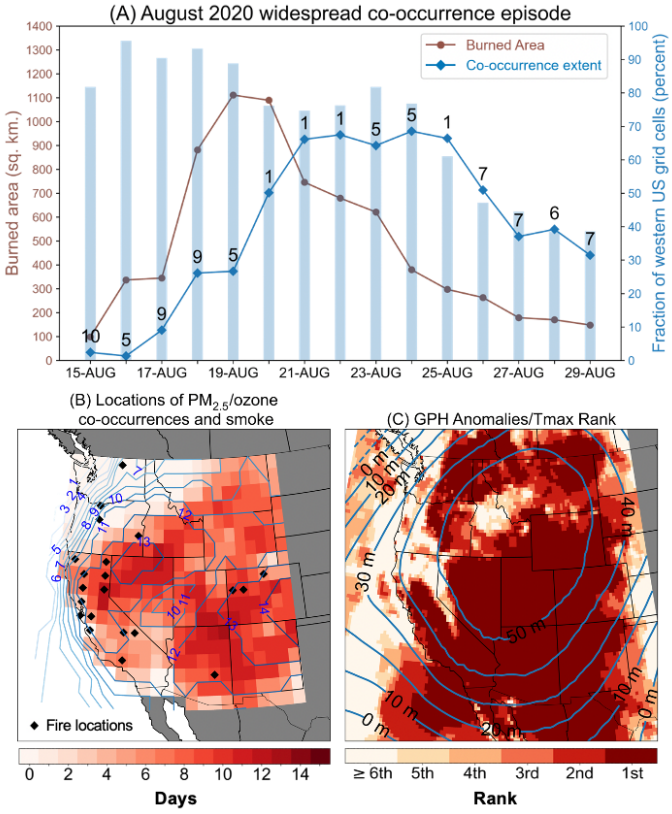

Fig. 5. Widespread co-occurrence episode during August 15th-29th, 2020. (A) Timeseries of daily burned area from MODIS in the western US and southwest Canada (brown line), fraction of western US grid cells with local $PM_{2.5}$/ozone co-occurrence (blue line), and fraction of western US grid cells with daily maximum temperature (Tmax) anomalies

exceeding 1 standard deviation above local daily climatology (blue bars). Numbers on the blue line indicate the best-matching SOM node for that day's atmospheric pattern. Note that widespread co-occurrence conditions begin on August 18th and persist through the 29th. (B) Total number of local $PM_{2.5}$/ozone co-occurrence days at each grid cell (shaded) and total number of days with presence of smoke from NOAA's Hazard Mapping System (contours) between August 15th-29th. Black markers indicate presence of wildfires from MODIS in at least 50 1-km grid cells contained within each of the 1° x 1° grid cells of the $PM_{2.5}$/ozone data. (C) Average geopotential height (GPH) anomalies (contours every 10 meters, as in Fig. 3 top row) and rank of the average Tmax during August 15th-29th, 2020, compared to all other similar two-week periods during 1979-2019 (shaded). The darkest red shading indicates that in 2020 those grid cells experienced their hottest average Tmax within the 42-year ERA5 dataset.

Large-scale atmospheric patterns shaped multiple aspects of this air pollution episode, including the high temperatures, wildfires, and smoke transport. Atmospheric ridging across the western US resembling the pattern of the high-exposure nodes contributed to the hot, dry, and stagnant air conditions conducive to wildfire ignition and pollutant accumulation from smoke during the first five days of the episode (August 15th-19th) (Fig. 5A). More than 75% of the western US experienced daily maximum temperature anomalies exceeding 1 standard deviation (σ) on all 5 days. Following the large increase in burned area during this time, a shift to an atmospheric pattern characterized by ridging centered in the interior West (Node 1, see Fig. S5A) developed on August 20th and persisted for three days, resulting in southwest-to-northeast atmospheric airflow in the western part of the domain (Fig. 5A). This pattern transported smoke from California fires across large areas of the interior western US, contributing to an increase in local $PM_{2.5}$/ozone co-occurrence extent from <30% to ~66% of the western US grid cells by August 21st (blue line, Fig. 5A).

The remote transport of wildfire smoke containing multiple pollutants including $PM_{2.5}$ and ozone to areas experiencing record warm conditions and enhanced photochemical ozone production (Fig. 5C) were critical to the widespread extent of this episode. Closer to active fires,

dense smoke blocks solar radiation and mitigates ozone production (*19*). In addition, previous studies have noted that aged smoke is more conducive to downwind ozone production (e.g. [*16*, *20*, *21*]), promoting local $PM_{2.5}$/ozone co-occurrences in remote areas where smoke is transported. However, the contribution of wildfire smoke to increased ozone concentrations, and thus increased $PM_{2.5}$/ozone co-occurrences needs to be further understood. Buysse *et al.* (*19*) found that the presence of wildfire smoke enhances ozone concentrations in urban areas of the western US, particularly in smoke plumes away from fire sources with $PM_{2.5}$ concentrations below 50 $\mu g/m^3$. Similarly, Brey and Fischer (*21*) and Gong *et al.* (*20*) noted general enhancement of ozone concentrations on smoke days in the western US. However, they also note distinct regional variation with some locations not observing increased ozone concentrations during smoke conditions.

Relationships between burned area, heat extremes, and $PM_{2.5}$/ozone co-occurrence

The dynamics of the August 2020 widespread co-occurrence episode highlight the importance of both meteorology and wildfire extent in shaping the extent of $PM_{2.5}$/ozone co-occurrences and therefore, exposure. We thus further characterize this relationship between wildfire burned area, meteorology, and the peak spatial extent of all temporally independent widespread co-occurrence periods (n = 21; refer to *Materials and Methods*) (Fig. 6). Given its relevance for ozone production, we specifically focus on relating daily maximum temperature anomalies to $PM_{2.5}$/ozone co-occurrence extent.

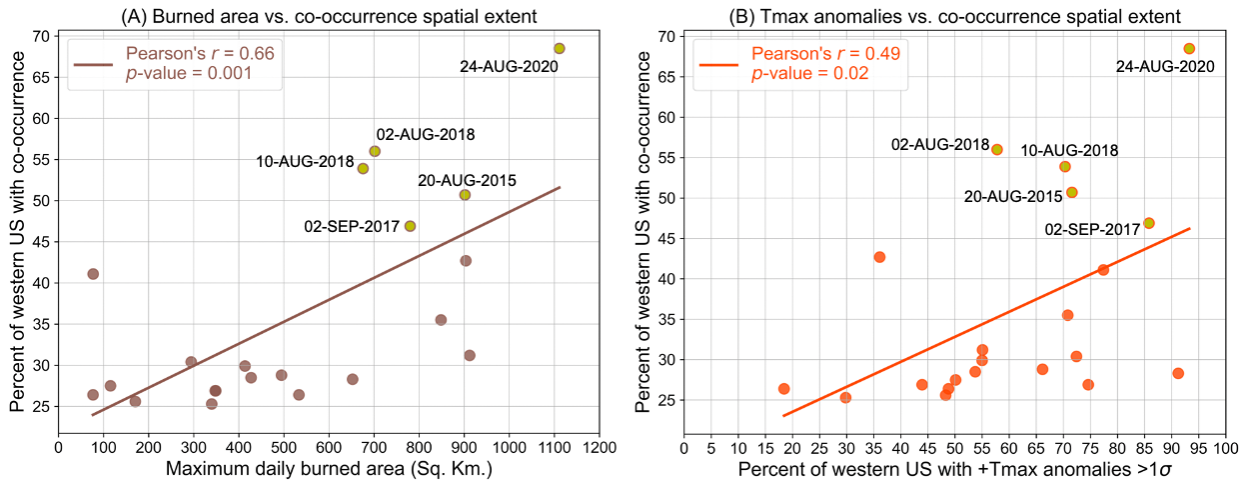

Fig. 6. Relationship between widespread $PM_{2.5}$/ozone co-occurrence extent, wildfire burned area and daily maximum temperatures. Scatterplots showing the spatial extent of the western US affected by $PM_{2.5}$/ozone co-occurrence with (A) 7-day lagged MODIS burned area in the western US and southwest Canada, and (B) 7-day lagged spatial extent of positive maximum temperature (+Tmax) anomalies >1 standard deviation above local daily climatologies in the western US during the period of overlap with available burned area data (2003-2020). For both burned area and +Tmax, the values represent the maximum daily extent in the 7 days preceding the peak spatial extent of $PM_{2.5}$/ozone co-occurrences. Only temporally independent widespread co-occurrence extent peaks during July-September are included (*n* = 21; refer to *Materials and Methods*). Dates for the top 5 largest extent peaks are shown. Text in panels indicates Pearson correlation coefficients (*r*) and *p*-values for the pairwise relationships.

Similar to the August 2020 episode, we find that the extent of wildfire activity and heat affect the spatial extent of other $PM_{2.5}$/ozone co-occurrences. The largest extents exceeding 45% of the western US (much larger than the threshold used to define a widespread co-occurrence day) occurred in 2015, 2017, 2018, and 2020 and were associated with extensive wildfire activity in the western US and southwest Canada (maximum daily burned area extent >650 km^2, Fig. 6A) and widespread positive daily maximum temperature anomalies exceeding 1σ (maximum daily extent ≥55% of the western US, Fig. 6B) in the 7 days preceding the peak spatial extent of temporally independent widespread $PM_{2.5}$/ozone co-occurrence periods (refer to *Materials and Methods*). Analyzing this relationship over these 21 independent co-occurrence spatial extent

peaks during 2003-2020, we find robust pairwise correlation between the $PM_{2.5}$/ozone co-occurrence extent and lagged burned area (r = 0.66, *p-value* = 0.001) as well as co-occurrence extent and 7-day lagged extent of anomalously high (>1σ) maximum temperature anomalies (r = 0.49, *p-value* = 0.02). These findings emphasize the role of simultaneous widespread heat and wildfire activity in shaping widespread $PM_{2.5}$/ozone co-occurrences, with high values of this combination of contributing factors in four of the six most recent July-September seasons in the western US.

DISCUSSION

Summary

Our analysis demonstrates an increasing risk of exposure of the western US population to more frequent and persistent extreme $PM_{2.5}$/ozone co-occurrences, defined at each grid cell as the simultaneous exceedance of the local annual 90th percentile concentrations of both pollutants, during the late summer wildfire season. These trends are largely driven by $PM_{2.5}$ extremes shifting toward the summer associated with increased wildfire activity in recent years (*24-26*, *32-39*) and coinciding with the season of high ozone concentrations. $PM_{2.5}$/ozone co-occurrences are also affecting larger areas, with more than a doubling of the maximum daily spatial extent (18.9% to 44.6%) of the western US experiencing simultaneous local co-occurrences over the past two decades. We find that increasing widespread pollutant co-occurrences are associated with increasing wildfire activity and increasing occurrence of conducive atmospheric patterns.

The increase in widespread $PM_{2.5}$/ozone co-occurrences during July-September highlights the role of increasingly severe and larger wildfires in contributing to compounding public health hazards in the western US. Although wildfire smoke can be transported to this

region from remote areas including Alaska (*54*) and Siberia (*55*), we find a robust correlation between burned area in the western US and adjacent southwest Canada and extent of local $PM_{2.5}$/ozone co-occurrence across the western US (Fig. 6A). Years with the maximum extent of co-occurrence (Fig. 1D, red line) and greatest frequency of widespread co-occurrence days (Fig. 2A) also experienced the highest mean burned area in the western US (see Fig. 7 in (*35*)). The largest spatial extents of co-occurrence in the observed record have all occurred since 2015 during particularly active wildfire seasons, with record co-occurrence extent and persistence in 2020 coinciding with record-breaking wildfire activity in several western US states. Given its ability to produce $PM_{2.5}$ extremes at a time of year when ozone concentrations are seasonally high, our results imply that increasing wildfire activity is a key mechanism by which simultaneous occurrences of local $PM_{2.5}$/ozone extremes are increasing in the western US despite declining background levels of these pollutants in response to the Clean Air Act (*23*, *32*, *56*, *57*).

Our results emphasize that atmospheric ridging patterns can affect widespread $PM_{2.5}$/ozone co-occurrences and associated population exposure by amplifying multiple direct physical drivers and sources of air pollutants. In addition to promoting conditions that are conducive for wildfires that produce multiple harmful air pollutants, persistent ridging results in widespread heat and air stagnation that enhances ozone production. Indeed, we identify a significant relationship between the extent of heat and local $PM_{2.5}$/ozone co-occurrences. Further emphasizing the importance of meteorology in influencing population exposure to widespread air pollution conditions, large-scale airflow around high pressure ridges can transport smoke and associated pollutants to remote areas. The presence of such favorable meteorological conditions was critical in shaping the 2020 widespread co-occurrence episode via record heat and atmospheric patterns conducive to smoke transport.

The increasing frequency and persistence of ridging during the late-summer wildfire season (Fig. 4) suggest an increased likelihood of the type of atmospheric conditions that contributed to the August 2020 co-occurrence episode, if these trends continue. While recent studies have shown an intensification of western US summer ridging since the 1980s using atmospheric reanalysis (*58*) and tree-ring records (*59*), identification of trends in ridging frequency and persistence over the western US prior to the present analysis had been restricted to other seasons (*60–62*). Our findings of changing late-summer atmospheric patterns agree with recent studies that have highlighted the role of increasingly warmer and drier summer seasons, which are strongly favored by atmospheric ridging, across the western US in driving increased wildfire burned area extent and severity (*38*, *39*). Further, drought and extreme heat events associated with persistent ridging can produce widespread dust and photochemical pollution-related health impacts across the western US (*63*, *64*), increasing the likelihood of compound stressors upon human health.

Limitations

We note multiple caveats to our findings. First, the derived gridded datasets of $PM_{2.5}$ and ozone used in this study are based on a relatively sparse observational network in some parts of the western US, which might result in uncertainties in identified trends in these areas. Enhancing spatial coverage of the monitoring network is critical to get more accurate and finer-scale air quality information, particularly over rural areas of the western US. While the PurpleAir network is rapidly enhancing the $PM_{2.5}$ observational coverage (*65*), it has notable measurement biases and a similar low-cost network is not currently available for ozone. Second, we mainly focus on identifying proximal relationships and do not directly link wildfire emissions with local

$PM_{2.5}$/ozone co-occurrences, and do not examine the dependence of pollutant and precursor concentrations on burn severity or types of fuel burned in different landscapes. Although we explicitly link the presence of wildfire smoke to local $PM_{2.5}$/ozone co-occurrences during the widespread episode of August 2020 using the NOAA HMS product, we do not systematically quantify the climatology of pollutant co-occurrences with or without presence of wildfire smoke due to the limited record, and do not link all individual fires to pollutant co-occurrences. Third, we investigate the relationship between the extent of $PM_{2.5}$/ozone co-occurrences and two main drivers – widespread heat and wildfire burned area - without explicitly accounting for hot, dry weather promoting further wildfires leading to enhanced co-occurrence extent. Hot temperatures are a common underlying driver of both wildfire activity and ozone production across the western US on different time scales (*23*), and high-resolution modeling would be required to disentangle the individual contributions of heat and wildfire smoke to local $PM_{2.5}$/ozone co-occurrences across this region.

Implications

In recent years, millions of people across the western US have been affected by hazardous air quality conditions caused by wildfire smoke. Although $PM_{2.5}$ concentrations are greatest in dense smoke plumes near wildfires, we find an increase in local $PM_{2.5}$/ozone co-occurrences over widespread areas of the western US not limited to the immediate proximity of active fires. These results highlight the potential for increasing population exposure to compounding human health stressors in fire-prone and remote regions, with projected increases in wildfire activity, smoke, and conducive meteorological conditions (*51*, *66*, *67*). Although more research is needed to assess the cumulative health outcomes of co-occurrences of $PM_{2.5}$/ozone

extremes as well other pollutants in wildfire smoke, it is very likely that these co-occurring air pollution extremes have compounding public health impacts (*29*). Their impacts are not only limited to the direct cardiovascular and pulmonary effects, but also extend indirectly to physical and mental health consequences arising from disruptions to outdoor activity, exercise, and normal social activities. Vulnerable communities in the western US that have limited access to healthcare or other resources needed to cope with poor air quality, have livelihoods that involve higher occupational exposure to polluted outdoor air, or have high rates of prevalence of medical conditions that can exacerbate the effects of air pollution exposure are likely to face increasing threats from such co-stressors. Understanding the likelihood and drivers of such co-occurring hazards is, therefore, critical for protecting communities through improved planning and management of human health impacts from projected warming, drying, and increasing wildfire activity in the western US.

MATERIALS AND METHODS

Datasets

We use 1° x 1° gridded $PM_{2.5}$ and ozone datasets spanning 2000-2020 for the United States developed using the methods of Schnell et al. (*46*) and subset to the western US domain (125°W-103°W, 31°N-49°N). These gridded datasets are derived from surface monitoring station data provided by the United States Environmental Protection Agency's Air Quality System (AQS; https://www.epa.gov/aqs, for $PM_{2.5}$ and ozone), Canada's National Air Pollution Surveillance Program (NAPS; https://open.canada.ca/data/en/dataset/1b36a356-defd-4813-acea-47bc3abd859b; for $PM_{2.5}$ and ozone), and the Clean Air Status and Trends Network (CASTNET; https://www.epa.gov/castnet, for ozone). Validated AQS data are used for $PM_{2.5}$/ozone spanning

October 2000 - July 2019, with preliminary data sourced from the AirNow online portal (https://www.airnow.gov) for August 2019 - September 2020. We use daily averages for $PM_{2.5}$ and the maximum daily 8-h average (MDA8) for ozone, reflecting the measures typically used for regulatory purposes and health impacts. For ozone, the hourly measurements are interpolated and MDA8 is calculated. For $PM_{2.5}$, daily averages are constructed prior to interpolation from any hourly reporting stations, and the daily average values are interpolated. The interpolation procedure is a hybrid inverse distance-weighted method that includes a declustering component designed to limit the influence of multiple clustered, typically urban observations. Parameters for the interpolation were optimized with a leave N-out cross-validation procedure. These gridded datasets were originally developed for the purpose of evaluating global chemistry models for their ability to simulate large-scale, multi-day air pollution episodes. They have also been used to analyze large-scale $PM_{2.5}$, ozone, and extreme temperature co-occurrences in the eastern US (*45*); thus, they are well-suited for similar analysis of $PM_{2.5}$/ozone co-occurrences across a large geographic region herein. $PM_{2.5}$/ozone data are analyzed over two seasons - July-September of the given year and October of the previous calendar year through June of the given year.

Meteorological data, consisting of 500-hPa geopotential heights and 2-m air temperature, were obtained from the ECMWF ERA5 reanalysis (https://www.ecmwf.int/en/forecasts/datasets/reanalysis-datasets/era5) on the native 0.25° x 0.25° resolution (*68*, *69*). For analyzing the co-location of wildfire smoke and $PM_{2.5}$/ozone co-occurrence during the August 2020 case study, daily wildfire smoke polygons for August 15th-29th, 2020, were obtained from NOAA's National Environmental Satellite, Data, and Information Service (NESDIS) Hazard Mapping System (HMS) smoke product (https://www.ospo.noaa.gov/Products/land/hms.html#data) (*19*, *54*). For each day, all polygons

representing smoke of any density were merged into a single polygon representing total smoke coverage for that day (*19*), and were overlaid with the 1° x 1° grid of the $PM_{2.5}$ and ozone datasets. Any grid cell spatially co-located with any portion of a smoke polygon is categorized as experiencing a 'smoke-day', enabling the computation of the total number of smoke-days during the 15-day episode in each grid cell. For visualization in Fig. 5B, the gridded values of smoke-day frequencies were interpolated to contours and smoothed with a Gaussian filter (*sigma* = 0.2), allowing for the preservation of large-scale spatial features of smoke-day counts while minimizing visual noise induced by local-scale variation.

The Moderate Resolution Imaging Spectroradiometer (MODIS) Aqua+Terra Thermal Anomalies/Fire Locations 1 km dataset (MCD14DL) was retrieved from NASA's Fire Information for Resource Management System (FIRMS) archive download portal (https://firms.modaps.eosdis.nasa.gov/download/). The MCD14DL product is used to identify the presence of wildfires (>95% confidence) in at least 50 1-km grid cells contained within each of the larger 1° x 1° grid cells during the August 2020 widespread co-occurrence episode. The 50 km^2 threshold was chosen to isolate large fire occurrences (*70*), as these fires are presumed to impact air quality on regional scales. To quantify the spatial extent of burned area in the western US and adjacent southwest Canada (Canadian data subset to <60°N, >115°W), we use the MODIS burned area product (2003-2020) (*71*).

We quantify population exposure to $PM_{2.5}$/ozone co-occurrences using estimated 2020 population counts from the Gridded Population of the World version 4 (GPWv4) dataset, obtained on a 1° x 1° grid from Columbia University's Socioeconomic Data and Applications Center (SEDAC; https://sedac.ciesin.columbia.edu) (*72*). Western US population is defined as the total population contained in all grid cells (n = 375) within the study domain, which includes

adjacent parts of the Great Plains and Mexico. We use person-days as a metric to quantify population exposure to local $PM_{2.5}$/ozone co-occurrence. It is obtained by multiplying the estimated 2020 population in each grid cell by the number of co-occurrences in that grid cell, and then aggregating it across the domain. We consider a fixed population to isolate the influence of changing physical hazards on changing exposure.

Defining $PM_{2.5}$/ozone co-occurrences

We seek to understand changes in simultaneous occurrence of extreme $PM_{2.5}$ and ozone concentrations, as co-occurrences of both pollutants have the potential to induce co-stressor effects on human and environmental health. We therefore define extremes for $PM_{2.5}$ and ozone at each grid cell individually as the exceedances of the local 90^{th} percentiles of their daily concentrations (average daily value for $PM_{2.5}$ and MDA8 for ozone) within each individual year. Therefore, we examine the co-occurrence of the top ~37 $PM_{2.5}$ and ozone extremes in each grid cell for each year. Instead of a fixed threshold to define extremes over the study period, this time-varying definition allows us to identify extremes relative to the overall improving air pollution due to emission reductions and stricter national air quality standards. Further, having a fixed number of individual occurrences of both pollutants in each year enables us to identify years with anomalous temporal co-occurrences driven by factors other than their climatology. Assuming independent distributions, in a given grid cell the joint probability of $PM_{2.5}$/ozone co-occurrence each with a 10% chance of occurrence is 3.65 days per year, if co-occurrences are truly random. However, nearly 86% of western US grid cells have a higher likelihood of co-occurrence relative to random chance alone (Fig. S6), suggesting the role of common physical drivers of such co-occurrences.

Characterizing large-scale atmospheric patterns

To investigate the influence of large-scale atmospheric patterns on local $PM_{2.5}$/ozone co-occurrences, we use Self-Organizing Maps (SOMs) to cluster daily geopotential height anomalies during July-September, 1979-2020 and identify typical atmospheric circulation patterns. SOMs are a type of artificial neural network commonly used in the climate sciences for spatial clustering of large-scale meteorological variables based on their similarity (*48*). The number and arrangement of SOM nodes is a subjective choice and depends on the application (*49*, *60*). We test three SOM node configurations comprising 6 (2 x 3), 12 (3 x 4), and 20 (4 x 5) nodes, to identify a configuration that minimizes similarity between clusters while also capturing the range of patterns that occur in this region.

To help inform our SOM configuration selection, we examined two sets of spatial correlation coefficients following Gibson et al. (*73*): 1) between each SOM node pattern and the individual constituent patterns in that node ('node-field' correlation, higher values are optimal), and 2) between every unique combination of node pairs ('node-node' correlation, lower values are optimal). See Fig. S7 for the distribution of both sets of correlation coefficients. We selected the 12-node (3 x 4) SOM configuration as the median node-field correlation is higher than in the 6-node configuration and the node-node correlation interquartile range is lower than in the 20-node configuration. The improvement in node-field correlation in the 20-node configuration is small (Fig. S7A), and this configuration qualitatively exhibits overlapping patterns due to the larger number of nodes. While the 6-node configuration does have a larger distinction amongst nodes (based on lower median; see Fig. S7B), it does not adequately represent the range of geopotential height patterns seen in the 12-node configuration. For SOM training, we use 200

initial iterations and 800 final iterations, and set the initial neighborhood radius to 3 with a final neighborhood radius of 1. SOM computation was performed using the MATLAB 'SOM Toolbox.'

Examining relationships between wildfires, extreme heat, and co-occurrence extent

Local co-occurrences of $PM_{2.5}$ and ozone extremes are a result of complex interactions between meteorology and wildfire smoke operating on multiple timescales. Our *a priori* assumption is that long-range transport of wildfire smoke can take several days to cover a large geographic extent of the western US. Further, our hypothesis is that multi-day heat waves can influence co-occurrence extent through both promoting wildfire activity that can produce air pollutants in following days, and through widespread photochemical production and accumulation of ozone. To account for such interactions, we examine the relationship between antecedent fire and heat conditions in the preceding week (7-day window) with local $PM_{2.5}$/ozone co-occurrence extent on a given day. We estimate the correlation between wildfire burned area preceding peak co-occurrence extent, and between the spatial extent of positive daily maximum temperature anomalies preceding peak co-occurrence extent.

To isolate conditions antecedent to peaks in the spatial extent of widespread co-occurrence, we extract the largest co-occurrence spatial extent in non-overlapping 15-day windows. This is done iteratively in descending order of co-occurrence extent for all July-September days during the period of overlap with burned area data (2003-2020). Starting with the largest spatial extent (68.5% of the western US on August 24th, 2020), a 15-day window, centered on that day, is used to exclude all other days in this window and this process is repeated

for each successive lower extent provided it is outside of all previous 15-day windows. This process yields 21 widespread co-occurrence extent peaks (out of 72 total widespread co-occurrence days; see Fig. S2) during July-September, 2003-2020, that we define as temporally independent and use in the correlation analyses to examine the relationship between the extent of burned area, heat and local $PM_{2.5}$/ozone co-occurrences.

The highest correlation between burned area and local $PM_{2.5}$/ozone co-occurrence extent ($r > 0.65$) for these 21 peak spatial extents occurs for lags of -3 to -7 days (Fig. S8, blue line), with peak correlation at -4 days ($r = 0.74$). The highest correlation between the extent of heat and co-occurrence ($r > 0.49$) occurs for lags of -6 to -13 days (Fig. S8, orange line), with peak correlation at -11 days ($r = 0.53$). We note that these lags are based on a relatively small number of peak dates and the time of peak extent of local $PM_{2.5}$/ozone co-occurrences following heat and fire conditions can vary for individual dates. Therefore, our use of the 7-day lagged window in this analysis captures the overlapping period of high correlation of co-occurrence extent with antecedent widespread heat conditions and burned area extent while accounting for differences in the timing of individual extent peaks.

References and Notes:

1. R. K. Chakrabarty, P. Beeler, P. Liu, S. Goswami, R. D. Harvey, S. Pervez, A. van Donkelaar, R. V. Martin, Ambient $PM_{2.5}$ exposure and rapid spread of COVID-19 in the United States. *Science of The Total Environment*. **760**, 143391 (2021).

2. S. B. Henderson, The COVID-19 pandemic and wildfire smoke: Potentially concomitant disasters. *Am. J. Public Health*. **110**, 1140-1142 (2020).

3. X. Zhou, K. Josey, L. Kamareddine, M. C. Caine, T. Liu, L. J. Mickley, M. Cooper, F.

Dominici, Excess of COVID-19 cases and deaths due to fine particulate matter exposure during the 2020 wildfires in the United States. *Sci. Adv*. **7**, eabi8789 (2021).

4. D. Schwela, Air pollution and health in urban areas. *Reviews on Environmental Health*. **15**, 13-42 (2000).

5. M. Ji, D. S. Cohan, M. L. Bell, Meta-analysis of the association between short-term exposure to ambient ozone and respiratory hospital admissions. *Environmental Research Letters.* **6**, 024006 (2011).

6. J. C. Liu, A. Wilson, L. J. Mickley, F. Dominici, K. Ebisu, Y. Wang, M. P. Sulprizio, R. D. Peng, X. Yue, J.-Y. Son, G. Brooke Anderson, M. L. Bell, Wildfire-specific fine particulate matter and risk of hospital admissions in urban and rural counties. *Epidemiology*. **28**, 77-85 (2017).

7. A. L. Goodkind, C. W. Tessum, J. S. Coggins, J. D. Hill, J. D. Marshall, Fine-scale damage estimates of particulate matter air pollution reveal opportunities for location-specific mitigation of emissions. *Proc. Natl. Acad. Sci. U. S. A.* **116**, 8775-8780 (2019).

8. J. Fuhrer, F. Booker, Ecological issues related to ozone: agricultural issues. *Environ. Int.* **29**, 141–154 (2003).

9. U. S. Environmental Protection Agency (EPA), OAR, Health and environmental effects of particulate matter (PM) (2016) (available at https://www.epa.gov/pm-pollution/health-and-environmental-effects-particulate-matter-pm).

10. J. Rahul, M. K. Jain, An investigation in to the impact of particulate matter on vegetation

along the national highway: A review. *Research Journal of Environmental Sciences*. **8**, 356-372 (2014).

11. D. R. Gold, A. I. Damokosh, C. A. Pope 3rd, D. W. Dockery, W. F. McDonnell, P. Serrano, A. Retama, M. Castillejos, Particulate and ozone pollutant effects on the respiratory function of children in southwest Mexico City. *Epidemiology*. **10**, 8–16 (1999).

12. N. Siddika, A. K. Rantala, H. Antikainen, H. Balogun, A. K. Amegah, N. R. I. Ryti, J. Kukkonen, M. Sofiev, M. S. Jaakkola, J. J. K. Jaakkola, Synergistic effects of prenatal exposure to fine particulate matter ($PM_{2.5}$) and ozone (O_3) on the risk of preterm birth: A population-based cohort study. *Environ. Res.* **176**, 108549 (2019).

13. B. Langmann, B. Duncan, C. Textor, J. Trentmann, G. R. van der Werf, Vegetation fire emissions and their impact on air pollution and climate. *Atmospheric Environment*. **43**, 107-116 (2009).

14. T. Strand, N. Larkin, M. Rorig, C. Krull, M. Moore, $PM_{2.5}$ measurements in wildfire smoke plumes from fire seasons 2005–2008 in the northwestern United States. *Journal of Aerosol Science*. **42**, 143-155 (2011).

15. M. V. Martín, R. E. Honrath, R. C. Owen, G. Pfister, P. Fialho, F. Barata, Significant enhancements of nitrogen oxides, black carbon, and ozone in the North Atlantic lower free troposphere resulting from North American boreal wildfires. *Journal of Geophysical Research: Atmospheres*. **111**, D23S60 (2006).

16. D. A. Jaffe, N. L. Wigder, Ozone production from wildfires: A critical review. *Atmospheric*

Environment. **51**, 1-10 (2012).

17. O. Moeini, D. W. Tarasick, C. T. McElroy, J. Liu, M. K. Osman, A. M. Thompson, M. Parrington, P. I. Palmer, B. Johnson, S. J. Oltmans, J. Merrill, Estimating wildfire-generated ozone over North America using ozonesonde profiles and a differential back trajectory technique. *Atmospheric Environment: X*. **7**, 100078 (2020).

18. C. D. McClure, D. A. Jaffe, Investigation of high ozone events due to wildfire smoke in an urban area. *Atmospheric Environment*. **194**, 146-157 (2018).

19. C. E. Buysse, A. Kaulfus, U. Nair, D. A. Jaffe, Relationships between particulate matter, ozone, and nitrogen oxides during urban smoke events in the western US. *Environmental Science & Technology*. **53**, 12519–12528 (2019).

20. X. Gong, A. Kaulfus, U. Nair, D. A. Jaffe, Quantifying O_3 impacts in urban areas due to wildfires using a generalized additive model. *Environ. Sci. Technol.* **51**, 13216–13223 (2017).

21. S. J. Brey, E. V. Fischer, Smoke in the city: How often and where does smoke impact summertime ozone in the United States? *Environ. Sci. Technol.* ***50***, 1288-1294 (2016).

22. P. Hou, S. Wu, Long-term changes in extreme air pollution meteorology and the implications for air quality. *Sci. Rep.* **6**, 23792 (2016).

23. M. Lin, L. W. Horowitz, R. Payton, A. M. Fiore, G. Tonnesen, US surface ozone trends and extremes from 1980 to 2014: quantifying the roles of rising Asian emissions, domestic controls, wildfires, and climate. *Atmospheric Chemistry and Physics*. **17**, 2943-2970 (2017).

24. P. E. Higuera, J. T. Abatzoglou, Record-setting climate enabled the extraordinary 2020 fire season in the western United States. *Global Change Biology*. **27**, 1-2 (2021).

25. Y. Xie, M. Lin, L. W. Horowitz, Summer $PM_{2.5}$ pollution extremes caused by wildfires over the western United States during 2017–2018. *Geophysical Research Letters*. **47** (2020).

26. Z. S. Wettstein, S. Hoshiko, J. Fahimi, R. J. Harrison, W. E. Cascio, A. G. Rappold, Cardiovascular and cerebrovascular emergency department visits associated with wildfire smoke exposure in California in 2015. *J. Am. Heart Assoc.* **7** (2018).

27. C. E. Reid, M. Brauer, F. H. Johnston, M. Jerrett, J. R. Balmes, C. T. Elliott, Critical review of health impacts of wildfire smoke exposure. *Environ. Health Perspect.* **124**, 1334–1343 (2016).

28. J. C. Liu, G. Pereira, S. A. Uhl, M. A. Bravo, M. L. Bell, A systematic review of the physical health impacts from non-occupational exposure to wildfire smoke. *Environ. Res.* **136**, 120–132 (2015).

29. C. E. Reid, E. M. Considine, G. L. Watson, D. Telesca, G. G. Pfister, M. Jerrett, Associations between respiratory health and ozone and fine particulate matter during a wildfire event. *Environ. Int.* **129**, 291–298 (2019).

30. S. Magzamen, R. W. Gan, J. Liu, K. O'Dell, B. Ford, K. Berg, K. Bol, A. Wilson, E. V. Fischer, J. R. Pierce, Differential cardiopulmonary health impacts of local and long-range transport of wildfire smoke. *GeoHealth*. **5**, e2020GH000330 (2021).

31. K. O'Dell, R. S. Hornbrook, W. Permar, E. J. T. Levin, L. A. Garofalo, E. C. Apel, N. J.

Blake, A. Jarnot, M. A. Pothier, D. K. Farmer, L. Hu, T. Campos, B. Ford, J. R. Pierce, E. V. Fischer, Hazardous air pollutants in fresh and aged western US wildfire smoke and implications for long-term exposure. *Environ. Sci. Technol.* **54**, 11838–11847 (2020).

32. C. D. McClure, D. A. Jaffe, US particulate matter air quality improves except in wildfire-prone areas. *Proc. Natl. Acad. Sci. U. S. A.* **115**, 7901–7906 (2018).

33. K. O'Dell, B. Ford, E. V. Fischer, J. R. Pierce, Contribution of wildland-fire smoke to US $PM_{2.5}$ and its influence on recent trends. *Environ. Sci. Technol*. **53**, 1797-1804 (2019).

34. M. Burke, A. Driscoll, S. Heft-Neal, J. Xue, J. Burney, M. Wara, The changing risk and burden of wildfire in the United States. *Proc. Natl. Acad. Sci. U. S. A.* **118** (2021).

35. K. T. Weber, R. Yadav, Spatiotemporal trends in wildfires across the western United States (1950–2019). *Remote Sensing*. **12**, 2959 (2020).

36. J. T. Abatzoglou, C. S. Juang, A. P. Williams, C. A. Kolden, A. L. Westerling, Increasing synchronous fire danger in forests of the western United States. *Geophysical Research Letters*. **48** (2021).

37. J. T. Abatzoglou, A. P. Williams, Impact of anthropogenic climate change on wildfire across western US forests. *Proc. Natl. Acad. Sci. U. S. A.* **113**, 11770–11775 (2016).

38. Z. A. Holden, A. Swanson, C. H. Luce, W. M. Jolly, M. Maneta, J. W. Oyler, D. A. Warren, R. Parsons, D. Affleck, Decreasing fire season precipitation increased recent western US forest wildfire activity. *Proc. Natl. Acad. Sci. U. S. A.* **115**, E8349–E8357 (2018).

39. S. A. Parks, J. T. Abatzoglou, Warmer and drier fire seasons contribute to increases in area

burned at high severity in western US Forests from 1985 to 2017. *Geophysical Research Letters*. **47** (2020).

40. M. A. Moritz, M.-A. Parisien, E. Batllori, M. A. Krawchuk, J. Van Dorn, D. J. Ganz, K. Hayhoe, Climate change and disruptions to global fire activity. *Ecosphere*. **3**, art49 (2012).

41. Y. Li, L. J. Mickley, P. Liu, J. O. Kaplan, Trends and spatial shifts in lightning fires and smoke concentrations in response to 21st century climate over the national forests and parks of the western United States. *Atmospheric Chemistry and Physics*. **20**, 8827-8838 (2020).

42. M. Goss, D. L. Swain, J. T. Abatzoglou, A. Sarhadi, C. A. Kolden, A. P. Williams, N. S. Diffenbaugh, Climate change is increasing the likelihood of extreme autumn wildfire conditions across California. *Environmental Research Letters*. **15**, 094016 (2020).

43. D. J. Jacob, D. A. Winner, Effect of climate change on air quality. *Atmospheric Environment*. **43**, 51-63 (2009).

44. D. E. Horton, C. B. Skinner, D. Singh, N. S. Diffenbaugh, Occurrence and persistence of future atmospheric stagnation events. *Nat. Clim. Chang.* **4**, 698–703 (2014).

45. J. L. Schnell, M. J. Prather, Co-occurrence of extremes in surface ozone, particulate matter, and temperature over eastern North America. *Proc. Natl. Acad. Sci. U. S. A.* **114**, 2854–2859 (2017).

46. J. L. Schnell, C. D. Holmes, A. Jangam, M. J. Prather, Skill in forecasting extreme ozone pollution episodes with a global atmospheric chemistry model. *Atmospheric Chemistry and Physics*. **14**, 7721-7739 (2014).

47. D. A. Jaffe, S. M. O'Neill, N. K. Larkin, A. L. Holder, D. L. Peterson, J. E. Halofsky, A. G. Rappold, Wildfire and prescribed burning impacts on air quality in the United States. *J. Air Waste Manag. Assoc.* **70**, 583–615 (2020).

48. S. C. Sheridan, C. C. Lee, The self-organizing map in synoptic climatological research. *Progress in Physical Geography: Earth and Environment*. **35**, 109-119 (2011).

49. R. Grotjahn, R. Black, R. Leung, M. F. Wehner, M. Barlow, M. Bosilovich, A. Gershunov, W. J. Gutowski, J. R. Gyakum, R. W. Katz, Y.-Y. Lee, Y.-K. Lim, Prabhat, North American extreme temperature events and related large scale meteorological patterns: A review of statistical methods, dynamics, modeling, and trends. *Climate Dynamics*. **46**, 1151-1184 (2016).

50. J. T. Abatzoglou, Contribution of cutoff lows to precipitation across the United States. *Journal of Applied Meteorology and Climatology*. **55**, 893-899 (2016).

51. A. G. Hallar, N. P. Molotch, J. L. Hand, B. Livneh, I. B. McCubbin, R. Petersen, J. Michalsky, D. Lowenthal, K. E. Kunkel, Impacts of increasing aridity and wildfires on aerosol loading in the intermountain western US. *Environmental Research Letters*. **12**, 014006 (2017).

52. A. K. Kochanski, D. V. Mallia, M. G. Fearon, J. Mandel, A. H. Souri, T. Brown, Modeling wildfire smoke feedback mechanisms using a coupled fire-atmosphere model with a radiatively active aerosol scheme. *Journal of Geophysical Research: Atmospheres.* **124**, 9099-9116 (2019).

53. A. Robock, Enhancement of surface cooling due to forest fire smoke. *Science*. 242, 911-913 (1988).

54. S. J. Brey, M. Ruminski, S. A. Atwood, E. V. Fischer, Connecting smoke plumes to sources using Hazard Mapping System (HMS) smoke and fire location data over North America. *Atmospheric Chemistry and Physics*. **18**, 1745-1761 (2018).

55. A. D. Teakles, R. So, B. Ainslie, R. Nissen, C. Schiller, R. Vingarzan, I. McKendry, A. M. Macdonald, D. A. Jaffe, A. K. Bertram, K. B. Strawbridge, W. R. Leaitch, S. Hanna, D. Toom, J. Baik, L. Huang, Impacts of the July 2012 Siberian fire plume on air quality in the Pacific Northwest. *Atmospheric Chemistry and Physics*. **17**, 2593-2611 (2017).

56. U. S. Environmental Protection Agency (EPA), OAR, Particulate matter ($PM_{2.5}$) trends (2016) (available at https://www.epa.gov/air-trends/particulate-matter-pm25-trends).

57. U. S. Environmental Protection Agency (EPA), OAR, Ozone trends (2016) (available at https://www.epa.gov/air-trends/ozone-trends).

58. L. Dong, L. R. Leung, Y. Qian, Y. Zou, F. Song, X. Chen, Meteorological environments associated with California wildfires and their potential roles in wildfire changes during 1984-2017. *Journal of Geophysical Research: Atmospheres*. **126**, e2020JD033180 (2021).

59. E. E. Montpellier, P. T. Soulé, P. A. Knapp, L. B. Perry, Reconstructing summer upper-level flow in the northern Rocky Mountains using an alpine larch tree-ring chronology. *Climate Research*. **79**, 207-218 (2020).

60. D. Singh, D. L. Swain, J. S. Mankin, D. E. Horton, L. N. Thomas, B. Rajaratnam, N. S.

Diffenbaugh, Recent amplification of the North American winter temperature dipole. *Journal of Geophysical Research: Atmospheres*. **121**, 9911–9928 (2016).

61. D. L. Swain, D. E. Horton, D. Singh, N. S. Diffenbaugh, Trends in atmospheric patterns conducive to seasonal precipitation and temperature extremes in California. *Sci. Adv*. **2**, e1501344 (2016).

62. P. B. Gibson, D. E. Waliser, B. Guan, M. J. DeFlorio, F. M. Ralph, D. L. Swain, Ridging associated with drought across the western and southwestern United States: characteristics, trends, and predictability sources. *Journal of Climate*. **33**, 2485-2508 (2020).

63. P. Achakulwisut, L. J. Mickley, S. C. Anenberg, Drought-sensitivity of fine dust in the US Southwest: Implications for air quality and public health under future climate change. *Environmental Research Letters*. **13**, 054025 (2018).

64. L. Shen, L. J. Mickley, E. Gilleland, Impact of increasing heat waves on U.S. ozone episodes in the 2050s: Results from a multimodel analysis using extreme value theory. *Geophysical Research Letters*. **43**, 4017-4025 (2016).

65. K. Ardon-Dryer, Y. Dryer, J. N. Williams, N. Moghimi, Measurements of $PM_{2.5}$ with PurpleAir under atmospheric conditions. *Atmospheric Measurement Techniques*. **13**, 5441-5458 (2020).

66. M. C. Brewer, C. F. Mass, Projected changes in western U.S. large-scale summer synoptic circulations and variability in CMIP5 models. *Journal of Climate*. **29**, 5965-5978 (2016).

67. J. C. Liu, L. J. Mickley, M. P. Sulprizio, F. Dominici, X. Yue, K. Ebisu, G. B. Anderson, R.

F. A. Khan, M. A. Bravo, M. L. Bell, Particulate air pollution from wildfires in the western US under climate change. *Climatic Change*. **138**, 655-666 (2016).

68. H. Hersbach, B. Bell, P. Berrisford, S. Hirahara, A. Horányi, J. Muñoz-Sabater, J. Nicolas, C. Peubey, R. Radu, D. Schepers, A. Simmons, C. Soci, S. Abdalla, X. Abellan, G. Balsamo, P. Bechtold, G. Biavati, J. Bidlot, M. Bonavita, G. De Chiara, P. Dahlgren, D. Lee, M. Diamantakis, R. Dragani, J. Flemming, R. Forbes, M. Fuentes, A. Geer, L. Haimberger, S. Healy, R. J. Hogan, E. Hólm, M. Janisková, S. Keeley, P. Laloyaux, P. Lopez, C. Lupu, G. Radnoti, P. de Rosnay, I. Rozum, F. Vamborg, S. Villaume, J-N Thépaut, The ERA5 global reanalysis. *Q J R Meteorol Soc.* **146**, 1999-2049 (2020).

69. Copernicus Climate Change Service (C3S), ERA5: Fifth generation of ECMWF atmospheric reanalyses of the global climate (2017). Copernicus Climate Change Service Climate Data Store (CDS), (available at https://cds.climate.copernicus.eu/cdsapp#!/home).

70. R. Barbero, J. T. Abatzoglou, E. A. Steel, N. K. Larkin, Modeling very large-fire occurrences over the continental United States from weather and climate forcing. *Environmental Research Letters*. **9**, 124009 (2014).

71. L. Giglio, L. Boschetti, D. P. Roy, M. L. Humber, C. O. Justice, The Collection 6 MODIS burned area mapping algorithm and product. *Remote Sens. Environ.* **217**, 72–85 (2018).

72. Center for International Earth Science Information Network - CIESIN - Columbia University, Gridded Population of the World, Version 4 (GPWv4): Population Count (2016). Palisades, NY: NASA Socioeconomic Data and Applications Center (SEDAC). http://dx.doi.org/10.7927/H4X63JVC.

73. P. B. Gibson, P. Uotila, S. E. Perkins-Kirkpatrick, L. V. Alexander, A. J. Pitman, Evaluating synoptic systems in the CMIP5 climate models over the Australian region. *Climate Dynamics*. **47**, 2235-2251 (2016).

Acknowledgments: The authors sincerely thank two anonymous reviewers for their insightful comments that improved this paper. We acknowledge ECMWF's Copernicus Climate Change Service for providing ERA5 data, and we thank multiple United States federal agencies (NASA, NOAA, EPA) for providing public access to the remaining datasets used in this study. We sincerely thank Cass Rogers and Peter Gibson for their input regarding Self-Organizing Maps methodology.

CHAPTER THREE: METEOROLOGICAL AND GEOGRAPHICAL FACTORS ASSOCIATED WITH DRY LIGHTNING IN CENTRAL AND NORTHERN CALIFORNIA

Kalashnikov, D. A., Abatzoglou, J. T., Nauslar, N. J., Swain, D. L., Touma, D., & Singh, D. (2022). Meteorological and geographical factors associated with dry lightning in central and northern California. *Environmental Research: Climate*, *1*(2), 025001. DOI: 10.1088/2752-5295/ac84a0

Originally published in *Environmental Research: Climate* and reproduced here in its original format.

Attributions:

Dmitri A. Kalashnikov designed the research, performed all analyses, and wrote the manuscript. D. Singh provided supervision and research direction, and helped edit the manuscript. J.T. Abatzoglou, N.J. Nauslar, D.L. Swain and D. Touma provided feedback on the research and helped edit the manuscript.

ABSTRACT

Lightning occurring with less than 2.5mm of rainfall – typically referred to as “dry lightning” – is a major source of wildfire ignition in central and northern California. Despite being rare, dry lightning outbreaks have resulted in destructive fires in this region due to the intersection of dense, dry vegetation and a large population living adjacent to fire-prone lands. Since thunderstorms are much less common in this region relative to the interior West, the climatology and drivers of dry lightning have not been widely investigated in central and northern California. Using daily gridded lightning and precipitation observations (1987-2020) in combination with atmospheric reanalyses, we characterize the climatology of dry lightning and the associated meteorological conditions during the warm season (May-October) when wildfire risk is highest. Across the domain, nearly half (~46%) of all cloud-to-ground lightning flashes occurred as dry lightning during the study period. We find that higher elevations (>2000m) receive more dry lightning compared to lower elevations (<1000m) with activity concentrated in July-August. Although local meteorological conditions show substantial spatial variation, we find regionwide enhancements in mid-tropospheric moisture and instability on dry lightning days relative to background climatology. Additionally, surface temperatures, lower-tropospheric dryness, and mid-tropospheric instability are increased across the region on dry versus wet lightning days. We also identify widespread dry lightning outbreaks in the historical record, quantify their seasonality and spatial extent, and analyze associated large-scale atmospheric patterns. Three of these four atmospheric patterns are characterized by different configurations of ridging over the continental interior and offshore troughing. Understanding the meteorology of dry lightning across this region can inform forecasting of possible wildfire ignitions and is relevant for assessing changes in dry lightning and wildfire risk in climate projections.

1. Introduction

Wildfires are a growing threat in California as the climate continues to warm. While human-caused wildfire ignitions predominate in southern California, lightning-caused fires are more prevalent in the northern half of the state, particularly over mountainous terrain (Balch *et al* 2017; Brey *et al* 2018; Chen and Jin 2022; Keeley and Syphard 2018; Komarek 1967; Show and Kotok 1923). Summertime lightning outbreaks accompanied by little or no rainfall (hereafter, "dry lightning") pose a threat for wildfire ignition where they align with flammable fuels. Unlike human-caused fires that originate in a single location, lightning outbreaks can strike multiple locations and start numerous simultaneous wildfires (Bartlein *et al* 2008; Court 1960; Komarek 1967; Miller *et al* 2012; Wallmann *et al* 2010). Widespread thunderstorms with dry lightning produced some of the largest and longest-lasting wildfires in recent decades in California, notably in 1987 (Duclos *et al* 1990), 2008 (Wallmann *et al* 2010), and 2020 (Keeley and Syphard 2021).

Despite its importance for wildfire ignition, few studies have explored dry lightning in central and northern California. Previous studies of summertime lightning in the western United States have omitted lower-elevation areas within this region due to small sample sizes of lightning activity (e.g., Abatzoglou *et al* 2016; Easterling and Robinson 1985; Kalashnikov *et al* 2020). Case studies have investigated the meteorology of notable dry lightning outbreaks to inform operational forecasting on short timescales (e.g., Nauslar *et al* 2013; Wallmann *et al* 2010). Van Wagtendonk and Cayan (2008) developed a climatology of lightning and associated meteorological patterns for California, but without a specific focus on dry lightning. A systematic climatology of dry lightning and associated meteorological conditions has thus not yet been developed for this region.

This study leverages three decades of gridded cloud-to-ground lightning and precipitation data (1987-2020) to compile the first long-term climatology of dry lightning for central and northern California. We utilize atmospheric reanalysis data to quantify the meteorological conditions that produce dry lightning and examine their differences compared to "wet" lightning. Due to their ability to produce widespread and costly wildfire outbreaks, we also analyze historical widespread dry lightning episodes and identify associated large-scale atmospheric patterns. As lightning climatology is strongly linked to topography in California (van Wagtendonk and Cayan 2008), we additionally explore the influence of elevation on dry lightning across this region. Understanding the characteristics and meteorological drivers of dry lightning is critical for anticipating fire ignitions in the present climate and for fully characterizing the changing risk of wildfires, including multiple fire ignitions, with ongoing and projected warming and drying in the region (Abatzoglou and Williams 2016; Goss *et al* 2020; Parks and Abatzoglou 2020).

2. Materials and Methods

2.1. Study domain

In this analysis, we focus on the warm season (May-October) due to the co-occurrence of dry lightning and seasonally dry vegetation that enhances wildfire risk. Our study domain encompasses the North Coast, Central Coast, and Sierra Nevada regions defined in Williams *et al* (2019) from Bailey's ecoregion sections and includes the Central Valley to form a spatially contiguous region (figure 1(A)). We focus on this region because of the relatively large tree cover and vegetation fraction and large wildfire burned areas associated with lightning relative to southern California, where humans are the major source of historical wildfire ignitions and

burned area (figures 1(B), (C), S.1) (Brey *et al* 2018; Keeley and Syphard 2018). Our domain excludes the western Great Basin for two primary reasons. *First*, the lightning-wildfire relationship differs in the Great Basin due to differences in both climate and vegetation composition, where both dry lightning flashes and lightning-ignited wildfires are climatologically more frequent compared to our domain (Abatzoglou *et al* 2016; Brey *et al* 2018), yet sparser fuels typically prevent most fires from growing large (Williams *et al* 2019). Outside of the agricultural lands of the Central Valley, most of our domain contains substantial tree cover (figure 1(C)), which provides additional fuel when compared to shrubs and herbaceous fuels common to other parts of the state (figure S.1) and increases the risk of sustained wildfire ignition resulting from a cloud-to-ground lightning flash (Hantson *et al* 2022). *Second*, the North American Monsoon brings moisture to the eastern fringe of California, favoring convection and substantially more lightning activity in the Great Basin (figure 1(D)), whereas our domain usually remains dry and free of lightning during such events. Despite being relatively rare in the historical record, our domain has experienced multiple dry lightning outbreaks over the past three decades that have led to numerous simultaneous wildfire ignitions and subsequently to large areas burned (e.g., in August 2020) – threatening the region's population, infrastructure, and air quality (Kalashnikov *et al* 2022; Podschwit and Cullen 2020). Due to its potentially outsized societal and ecological impacts, we focus our analysis on dry lightning in this distinct domain.

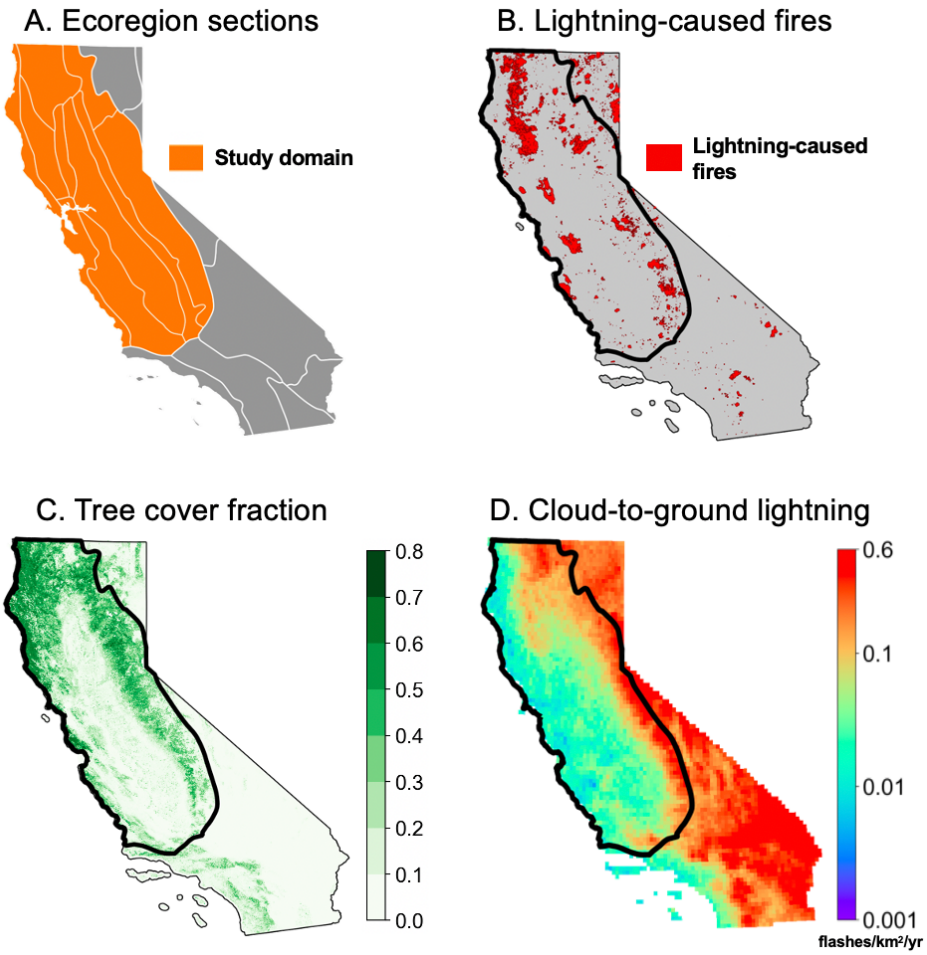

Figure 1. (A) The study domain (orange) comprised of Bailey's ecoregion sections. (B) Lightning-caused wildfire perimeters (red) from the California Department of Forestry and Fire Protection (CAL FIRE) for May-October 1987-2020. (C) Tree cover fraction from the Moderate Resolution Imaging Spectroradiometer at each 250m grid cell. (D) Density of cloud-to-ground lightning flashes averaged over May-October 1987-2020 (flashes/km^2/yr). Study outline is shown in black in (A, C, and D). Note that values in (D) are presented on a base-10 logarithmic scale. Maps were created using the QGIS open-source software.

2.2. Datasets

Daily-gridded cloud-to-ground lightning flash totals (0.1°x0.1°, 1987-2020) from the National Lightning Detection Network (NLDN) were sourced from the National Centers for Environmental Information Severe Weather Data Inventory (https://www.ncei.noaa.gov/pub/data/swdi/database-csv/v2/). Daily precipitation amounts were

obtained from the widely used, high-resolution (4km) gridMET dataset (Abatzoglou 2013) and interpolated to the 0.1° grid of the NLDN dataset using bilinear interpolation from the *GeoCAT-comp* Python package (VAST 2021). Other meteorological variables are from the European Centre for Medium-Range Weather Forecasts ERA5 reanalysis (0.25°x0.25°) (C3S 2017; Hersbach *et al* 2020). For analyzing the influence of elevation on dry lightning, grid cell elevations were calculated using surface geopotential from ERA5 at a 0.1° resolution (https://www.ecmwf.int/en/era5-land).

For delineating the study domain, polygons of Bailey's ecoregion sections were sourced from the United States Geological Survey (USGS) (https://www.sciencebase.gov/catalog/item/54244abde4b037b608f9e23d). Tree cover and vegetation fraction over the domain (as of 2020; 250m resolution) are from the Moderate Resolution Imaging Spectroradiometer's Vegetation Continuous Fields database (MOD44B) sourced from the USGS Land Processes Distributed Active Archive Center (https://lpdaacsvc.cr.usgs.gov/appeears/). The vegetation fraction was computed at each grid cell using the "Percent_NonVegetated" dataset from MOD44B.

Wildfire information for May-October 1987-2020 was obtained from the multi-agency "Fire Perimeters through 2020" dataset, sourced from the California Department of Forestry and Fire Protection (CAL FIRE) Fire and Resource Assessment Program (https://frap.fire.ca.gov/). This dataset excludes timber fires <4ha, brush fires <12ha, and grass fires <121ha when reported by CAL FIRE, and all fires <4ha when reported by the United States Forest Service, and assigns 19 possible fire causes including "Lightning". Any fires with perimeters intersecting the study domain boundary were considered part of the domain, and their final burned areas included herein. A total of 5479 fires were reported in the study domain, representing 6 373 876ha area

burned between 1987-2020. Of these, 1562 were officially categorized as lightning-caused fires (~28.5%) that accounted for nearly half of the total burned area (~49.3%).

2.3. Dry lightning definition

We define a dry lightning day as any cloud-to-ground lightning detection synchronous with <2.5mm (<0.10 inches) accumulated precipitation, using NLDN lightning and gridMET precipitation data. Daily rainfall below 2.5mm is typically considered insufficient to prevent sustained fire ignition resulting from associated lightning strokes. This precipitation threshold is used operationally by the National Oceanic and Atmospheric Administration/National Weather Service Storm Prediction Center (https://www.spc.noaa.gov/exper/dryt/) and has been widely used in previous studies of dry lightning (e.g., Abatzoglou *et al* 2016; Dowdy 2020; Dowdy and Mills 2012a; Rorig and Ferguson 1999).

GridMET daily total precipitation is reported from midnight-midnight local time each calendar day whereas NLDN reported daily lightning totals are binned from 5 PM-5 PM local time. To account for the difference in the temporal aggregation of these datasets, we consider accumulated precipitation over two consecutive calendar days overlapping with the lightning data (e.g., from midnight-midnight local time on both calendar days). While this is a conservative approach less likely to falsely identify dry lightning, inclusion of a second calendar day could increase the 2-day accumulated precipitation beyond 2.5mm, thereby not capturing dry lightning occurrence if either calendar day accumulated <2.5mm of precipitation coincident with a cloud-to-ground flash. We test the sensitivity of our approach by using daily NLDN lightning data binned from midnight-midnight local time for 2017–19 acquired from the Western Regional Climate Center (https://wrcc.dri.edu/). Daily dry lightning extents from these datasets show

substantial agreement ($r = 0.84$, $P < 0.05$, figure S.2), indicating that our approach reasonably captures dry lightning climatology in this region. Longer-term lightning data at higher temporal resolution is not yet publicly available and the costs of obtaining this data are prohibitive.

2.4. Dry lightning characteristics

We compile a climatology of dry lightning across the domain and compute the fraction of cloud-to-ground lightning flashes that were dry at each 0.1° grid cell ("*dry lightning fraction*"), further stratifying this climatology by month and by elevation zone. We define *dry lightning spatial extent* as the percentage of grid cells in our domain that experience dry lightning on a given day. *Widespread dry lightning days* are defined as days that have dry lightning spatial extents exceeding 6.1% (~15 200 km^2, $n = 124$ days), which represents the 95th percentile of these extents across the 34-year record. We also examine consecutive 2-day widespread dry lightning outbreaks as some events can last more than 24 hours (Wallmann *et al* 2010). This approach additionally captures late-afternoon lightning outbreaks when lightning data might be split due to the temporal binning of the NLDN dataset.

Although not all widespread dry lightning outbreaks in our record resulted in large burned areas – owing to differences in the types of landscapes struck by lightning as well as antecedent climatic and biophysical controls on burned area (Abatzoglou *et al* 2016; Barbero *et al* 2014) – a portion of these outbreaks have nonetheless produced the largest and costliest lightning-ignited wildfire episodes in modern California history (Keeley and Syphard 2021; Wallmann *et al* 2010). To illustrate this, we estimate wildfire burned areas associated with the ten most widespread dry lightning days in the 34-year record from the CAL FIRE dataset. This is done by extracting all fires identified as lightning-caused with "alarm dates" between -3 and +3

days from each of the ten most widespread dry lightning days, and aggregating their final burned areas. We do this to account for i) the 5 PM-5 PM binning window of the lightning dataset overlapping two calendar dates of possible fire reports, ii) the prospect of "holdover" fires, when fires are not detected for multiple days until they have grown sufficiently large for detection (MacNamara *et al* 2020; Schultz *et al* 2019), and iii) cases when the most widespread dry lightning day represents a multi-day sequence of dry lightning, when wildfire ignition and detection may have occurred several days prior to the most widespread dry lightning spatial extent of the multi-day episode.

2.5. Meteorological variables

Dry thunderstorms need three key ingredients to occur – mid-tropospheric moisture, a lifting mechanism, and a sufficiently dry lower-troposphere to evaporate the majority of rainfall before it reaches the ground (Nauslar *et al* 2013; Rorig *et al* 2007; Rorig and Ferguson 1999; Wallmann *et al* 2010). Lifting can be provided dynamically by transient cyclonic circulations (e.g., shortwave troughs) or thermodynamically through steep vertical temperature differences ("lapse rates"), or both (Nauslar *et al* 2013; Rorig and Ferguson 1999; Wallmann *et al* 2010). The cyclonic circulation around approaching shortwave troughs can additionally promote mid-tropospheric moisture transport to the region from either the Pacific Ocean or locations to the southeast where monsoonal moisture is more prevalent during the warm season (Nauslar *et al* 2013; Wallmann *et al* 2010).

We analyze several local meteorological variables that capture these conditions on dry lightning days at each 0.25° ERA5 grid cell with variable selection informed by literature. To capture atmospheric instability, the mid- ("MTLR") and upper-tropospheric lapse rates

("UTLR") are defined as vertical temperature differences (°C km^{-1}) between 700-500 hPa and 500-300 hPa, respectively (Nauslar *et al* 2013; Wallmann *et al* 2010). Mid-tropospheric moisture is defined as the pressure-weighted specific humidity between 700-500 hPa ("$Q_{700\text{-}500}$") (Nauslar *et al* 2013; Wallmann *et al* 2010), computed from constituent ERA5 pressure levels at 50-hPa increments using the *MetPy* Python package (May *et al* 2021). To understand the degree to which large-scale weather patterns during dry lightning are transient and provide conditions potentially favorable for dynamic lifting, we examine mid-tropospheric wind speeds. While previous studies have utilized 700 hPa to analyze thunderstorm-relevant atmospheric flow (e.g., Bertram and Mayr 2004; Kalashnikov *et al* 2020; Soriano *et al* 2001), we analyze wind speed at 500 hPa ("UV_{500}") due to the elevated cloud bases known to exist with dry lightning (Nauslar *et al* 2013; Rorig *et al* 2007). Lower-tropospheric dryness is represented by the dewpoint depression (i.e., the difference between the temperature and dewpoint) at 850 hPa ("DD_{850}") following Rorig and Ferguson (1999). The 850 hPa dewpoint was calculated using *MetPy* from temperature and relative humidity fields provided by ERA5. Finally, we examine surface heating, represented by daily maximum temperatures ("T_{max}"), as a proxy for near-surface instability and dryness.

The variables we have selected broadly describe the convective environment in which dry lightning occurs and are relatively straightforward to compute from ERA5 pressure-level data, making them useful for future studies evaluating climate model output. Although there are other variables such as Convective Available Potential Energy (CAPE) and Lifted Index that have been used to describe thunderstorm environments, we have not included them in our analysis for several reasons. *First*, due to the elevated cloud bases, surface- and lower troposphere-based convective parameters do not adequately describe the vertical instability profiles typically

associated with dry lightning (Wallmann *et al* 2010). *Second*, although we considered using CAPE calculated from the most unstable air parcel in the lowest 300 hPa (e.g., "Most Unstable CAPE"), to more accurately resolve elevated instability (Doswell and Rasmussen 1994; Rochette *et al* 1999), recent studies have noted substantial biases in modern atmospheric reanalyses relative to sounding data (e.g., Taszarek *et al* 2018). *Third*, the utility of computing Most Unstable CAPE as a climatological parameter over regional domains is unclear due to the widely varying vertical profiles of moisture and instability associated with individual dry lightning events (Wallmann *et al* 2010), making this variable more amenable to operational forecasting of individual events in combination with other diagnostics.

To understand meteorological characteristics unique to dry lightning days, we compare averages of all variables on dry lightning against "wet lightning" days (cloud-to-ground lightning with ≥2.5mm accumulated precipitation) (Bates *et al* 2017; Rorig and Ferguson 1999) and against local background climatology at each grid cell, computed using a running 7-day mean across the 34-year record.

2.6. Identifying large-scale atmospheric patterns

Previous studies have shown that warm-season lightning outbreaks in different parts of California are associated with a set of distinct meteorological patterns (e.g., van Wagtendonk and Cayan 2008). To characterize the different types of large-scale atmospheric patterns observed on the 124 widespread dry lightning days, we perform *k*-means clustering (MacQueen 1967) on the associated 500-hPa geopotential heights ("Z_{500}") from ERA5. Clustering of atmospheric patterns is conducted over a larger region (25°N-50°N, 140°W-105°W) in order to capture large-scale atmospheric features potentially relevant for dry lightning meteorology over our study domain.

We use a hybrid empirical-objective approach to select the *k* number of clusters (Detzer *et al* 2020; Grotjahn *et al* 2016). We analyzed multiple cluster arrangements over a range of cluster numbers ($k = 2{:}8$) and found that composite patterns constructed from four clusters (i.e., $k = 4$) sufficiently represent the diversity of atmospheric patterns associated with widespread dry lightning while minimizing overlap between patterns. Cluster representativeness was tested using 2-D pattern correlation between each cluster's composite pattern and its constituent days. We note that a number of previous studies focused on this region have also used four large-scale patterns when characterizing the meteorology of flash flooding (Maddox *et al* 1980), lightning (van Wagtendonk and Cayan 2008), and heavy precipitation (Moore *et al* 2021).

At each NLDN grid cell, we calculate the likelihood of dry lightning occurring with each cluster's pattern relative to random chance. This is done by first dividing the number of dry lightning days at that grid cell associated with each cluster by the total number of dry lightning days recorded at that grid cell from all clusters. To account for the uneven binning of widespread dry lightning days between clusters, this fraction of dry lightning occurrences is then divided by the fraction of all widespread dry lightning days belonging to that cluster. This process produces a ratio where values >1 indicate an increased likelihood of dry lightning in that grid cell with that cluster's pattern compared to random chance alone. For each cluster, we compare the distributions of area-averaged meteorological variables (Section 2.5) and assess statistical significance of differences from all other days using the Kolmogorov-Smirnov test.

3. Results and Discussion

3.1. Climatology of dry lightning across elevation zones

The average number of annual dry lightning flashes varies substantially across the domain (figure 2(A)). Enhanced dry lightning activity is strongly tied to elevation across the region (figure 2(B), inset), with a larger mean number of flashes in the high-elevation zone (>2000m) over the Sierra Nevada exceeding 0.5 flashes/km^2/yr (figure 2(A)). The greater density of dry lightning over the Sierra Nevada is consistent with studies that examined both dry lightning (e.g., Abatzoglou *et al* 2016) and total cloud-to-ground lightning (e.g., van Wagtendonk 1994; van Wagtendonk and Cayan 2008) over this region.

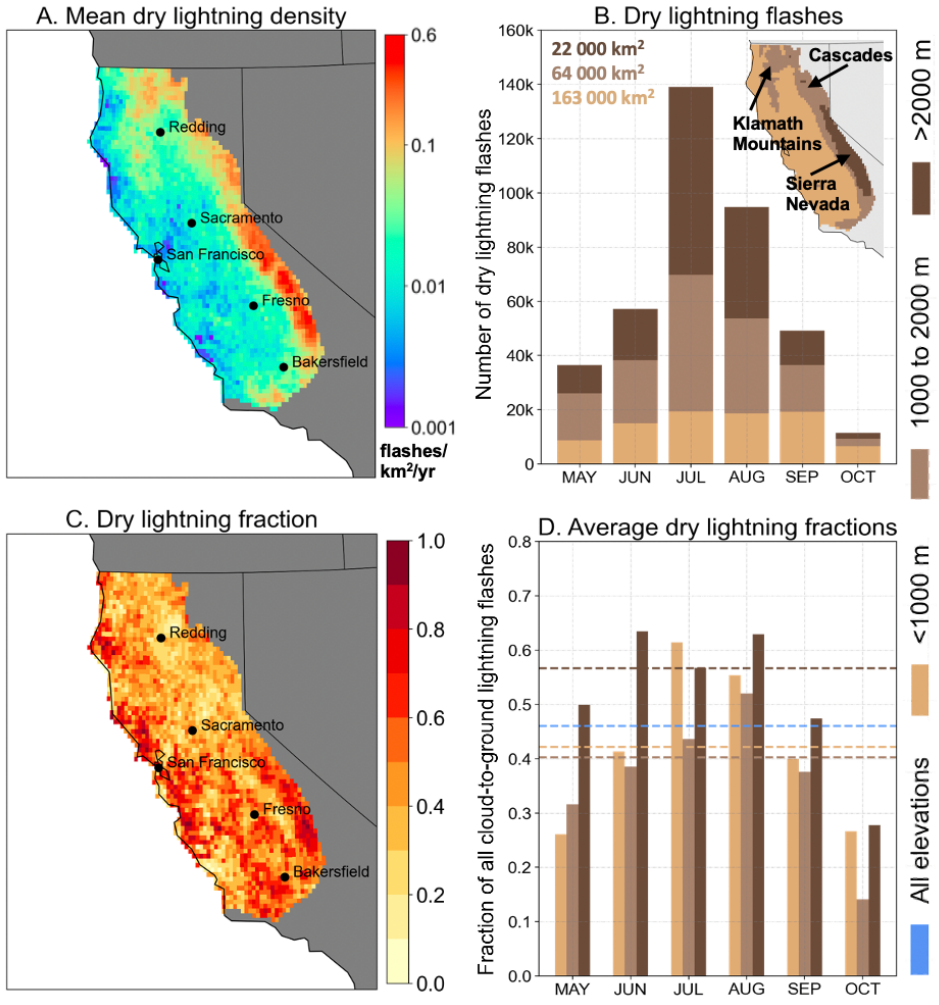

Figure 2. (A) Density of dry lightning flashes (cloud-to-ground lightning with <2.5mm rainfall) averaged over May-October 1987-2020 (flashes/km^2/yr). (B) Total number of dry

lightning flashes across three elevation zones (<1000m, 1000-2000m, >2000m) within the domain for each month between 1987-2020. Text indicates the area of each elevation zone, and inset map shows the geographic distribution of the elevation zones and major mountain ranges. Fraction of all cloud-to-ground lightning flashes occurring as dry lightning in (C) each 0.1° NLDN grid cell across all months and (D) the three elevation zones for each month (bars). Dashed lines in (D) indicate the dry lightning fraction averaged across all months for each zone. Blue dashes in (D) represent the dry lightning fraction computed from all months and elevation zones. Note that values in (A) are presented on a base-10 logarithmic scale.

To assess the elevational dependence of dry lightning, we quantify dry lightning climatology across different elevation zones (figure 2(B)). The medium- (1000-2000m) and high-elevation (>2000m) zones show a pronounced dry lightning peak in July-August with only minimal activity in October (figure 2(B)). Dry lightning flash totals in the low-elevation zone (<1000m) show less variability from June-September (figure 2(B), light brown). Further, while the high-elevation zone accounts for ~50% of all dry lightning flashes across the domain in July, this proportion reduces to ~26% in September (figure 2(B), dark brown). Conversely, the proportion of regionwide dry lightning occurring in the low-elevation zone increases from ~14% in July to ~39% in September (figure 2(B), light brown).

The dry lightning fraction is greater across the southern and western portions of the region, which comprise mainly low-elevation areas, and over the Sierra Nevada (figure 2(C)). In the high-elevation zone of the Sierra Nevada, ~57% of all lightning flashes occurred as dry lightning in the 34-year record (figure 2(D), dark brown dashes) and this fraction exceeded 45% in all months except October (figure 2(D), dark brown bars). In the low-elevation zone, the average dry lightning fraction exceeds 40% in June-September (figure 2(D), light brown bars). Summed across the domain, nearly half (~46%) of all lightning flashes were dry in the 34-year record (figure 2(D), blue dashes).

Our finding of the large dry lightning fraction (>0.5) over the Sierra Nevada may be counterintuitive, as a deeper layer of sub-cloud dry air over low-elevation regions should increase the dry lightning fraction there relative to higher elevations. Over the Sierra Nevada, the relatively large dry lightning fraction could be indicative of a greater density of cloud-to-ground lightning flashes on dry lightning days versus wet lightning days, rather than a greater frequency of individual thunderstorms occurring as dry. Further, strong orographic lifting can produce convection over high terrain in the presence of less atmospheric moisture than would be required to produce convection over lower elevations (Tardy 2001), which may lead to increased incidence of dry thunderstorms over the Sierra Nevada. In addition, gridded precipitation datasets might not capture all convective precipitation which occurs over sparsely-gauged mountain regions (Abatzoglou *et al* 2016), resulting in a potential source of bias in the dry lightning fraction over the Sierra Nevada and other mountain ranges in the study domain. The smaller dry lightning fraction over the lower-elevations of the northern Sacramento Valley and adjacent foothills (figure 2(C)) could be indicative of the surface-based moisture convergence zone found here (Tardy 2002), which would increase the chance of rainfall exceeding 2.5mm accompanying lightning.

3.2. Geographic variations in meteorological conditions on dry lightning days

The local meteorological conditions on dry lightning days also exhibit substantial variations across the domain (figure 3). On dry lightning days, 500 hPa wind speeds (UV_{500}) are strongest in the lower-elevation regions including the lowland San Francisco-Sacramento corridor of central California, exceeding 12 m s^{-1} (figure 3(A)). UV_{500} anomalies on dry lightning days are above background climatology in these areas, whereas they are >3 m s^{-1} below

climatological values over the higher-elevation regions (figure 3(G)). This spatial pattern implies stronger mid-tropospheric steering flow and increased chances of dynamic lifting assisting convective development on dry lightning days at lower elevations compared to higher elevations, where convection can occur due to orographic lifting with lesser dependence on mid- and upper-tropospheric dynamics. Indeed, UV_{500} shows a robust negative correlation with elevation on dry lightning days across the domain (Spearman's rank correlation -0.86, $P < 0.05$; figure S.3(A)).

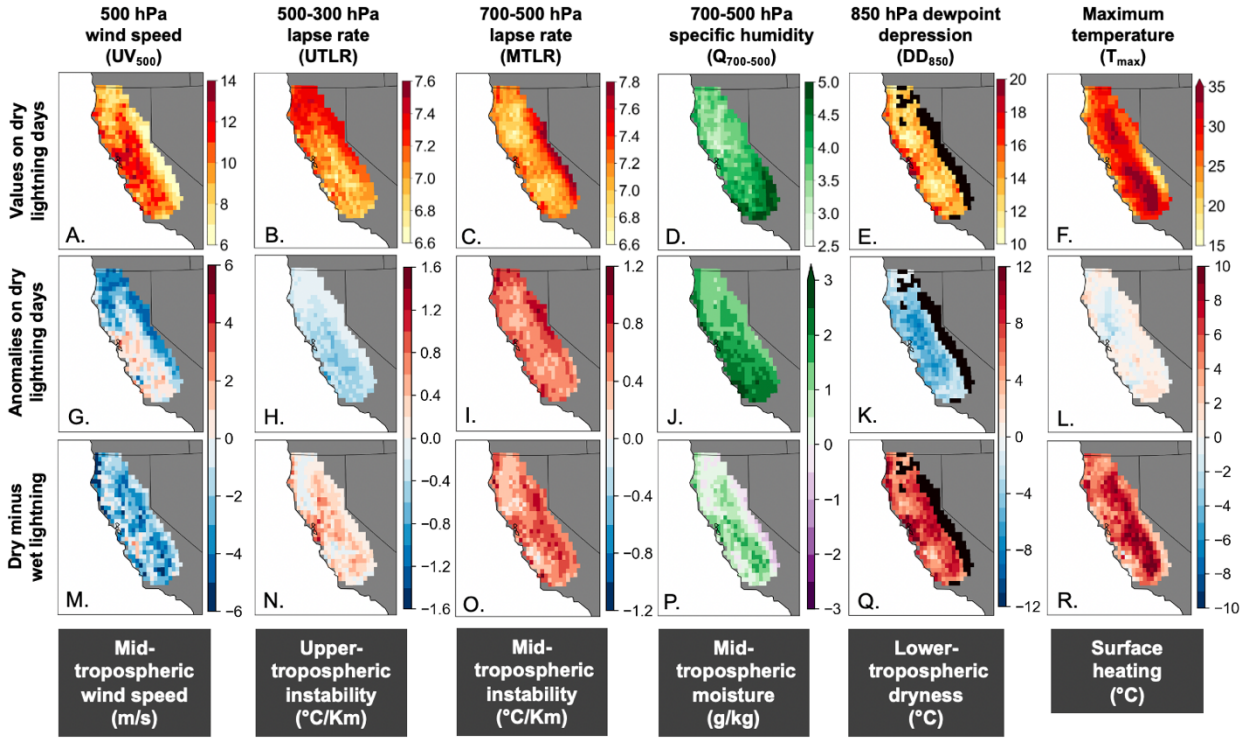

Figure 3. (A-F) Meteorological variables on dry lightning days at each 0.25° ERA5 grid cell during May-October 1987-2020. (G-L) Difference between values on dry lightning days and local background climatology, computed as the departure from the 7-day running mean (1987-2020) centered on each dry lightning day at each grid cell. (M-R) Difference between values on dry lightning (<2.5mm rainfall) and wet lightning days (≥2.5mm rainfall). Black shading in (E, K, Q) indicates surface elevations above 850 hPa.

The upper-tropospheric lapse rate (UTLR) is steepest over northern areas exceeding 7.3°C km^{-1} on dry lightning days and reduces further south (figures 3(B), S.4). Over most of the

domain, UTLR is suppressed relative to background climatology (figure 3(H)). While UTLR exceeding 7.5°C km^{-1} has been previously identified as an important ingredient of dry lightning over northern California (e.g., Wallmann *et al* 2010), our results suggest that lower UTLR values are sufficient to promote dry lightning over this region (figure 3(H)). In contrast, the mid-tropospheric lapse rate (MTLR) is steeper over high elevations of the Sierra Nevada exceeding 7.7°C km^{-1} on dry lightning days (figure 3(C)). MTLR is enhanced compared to climatology regionwide (figure 3(I)), indicating that enhanced mid-tropospheric instability relative to climatology is a key ingredient of dry lightning across the domain.

Mid-tropospheric specific humidity ($Q_{700\text{-}500}$) is highest over southern areas (figure 3(D)) and above background climatology on dry lightning days regionwide, with the largest enhancement of anomalies (>2 g kg^{-1}) in the coastal zone and southern areas (figure 3(J)). These areas largely correspond to the zone of enhanced UV_{500} (figure 3(G)) which could suggest increased mid-tropospheric moisture transport to the region by stronger atmospheric flow at that level. The dewpoint depression at 850 hPa (DD_{850}) is greater over the coastal zone with values exceeding 16°C, indicating drier lower-tropospheric conditions compared to interior locations (figure 3(E)). However, DD_{850} is suppressed relative to climatology across the domain indicating increased atmospheric moisture content compared to climatology in the lower troposphere as well (figure 3(K)). Our results emphasize the importance of atmospheric moisture enhancement in the mid- to lower-troposphere on dry lightning days across the region. These results further suggest that even though the lower-troposphere is “moistened” compared to normal on dry lightning days, conditions are not moist enough for substantial precipitation at the surface. Surface temperatures (T_{max}) on dry lightning days are similar to climatology, with the warmest temperatures over the Central Valley (figure 3(F)).

To understand the differences in meteorology during dry and wet lightning, we contrast the magnitude of these variables on dry versus wet lightning days. On dry lightning days, UV_{500} is generally weaker compared to wet lightning days across the domain with some areas experiencing reductions of >3 m s^{-1} (figure 3(M)), indicating that stronger mid-tropospheric flow is present on wet lightning days in many areas. This may suggest that large-scale atmospheric patterns with weaker mid-tropospheric winds but sufficient moisture, such as northward-displaced high pressure ridges centered over the Northwest or closed lows centered over California (Abatzoglou 2016; van Wagtendonk and Cayan 2008), may cause more dry lightning days compared to wet lightning days during the warm season. Conversely, UTLR is steeper on dry lightning days in many areas compared to wet lightning (figure 3(N)), despite suppressed UTLR compared to background climatology apparent in figure 3(H). $Q_{700\text{-}500}$ is also higher compared to wet lightning over many parts of the Central Valley, indicating a greater enhancement of mid-tropospheric moisture on dry lightning versus wet lightning days over many low-elevation areas (figure 3(P)). These results may be counterintuitive and could reflect a narrower atmospheric moisture layer on dry lightning days confined to the mid-troposphere, compared to a more saturated lower troposphere (below 700 hPa) associated with wet lightning (Nauslar *et al* 2013; Wallmann *et al* 2010). Conversely, $Q_{700\text{-}500}$ is reduced on dry lightning days over several mountainous areas compared to wet lightning, including over the Klamath Mountains and Sierra Nevada (figure 3(P)). While these results may indicate less available moisture, they may also reflect uncertainty in the exact location of moisture in the atmospheric column during dry lightning, which varies vertically from event to event, or instances when cloud bases are substantially above 700 hPa, which would not be resolved by a layer-average from 700-500 hPa (Nauslar *et al* 2013; Wallmann *et al* 2010).

Enhancements of mid-tropospheric instability, lower-tropospheric dryness, and surface heating are evident on dry- versus wet-lightning days across most of our study domain. MTLR is steeper on dry lightning versus wet lightning days regionwide with enhancements of >0.5°C km^{-1} in central and southern areas (figure 3(O)), comparable to results of previous analyses over the interior West (e.g., Rorig and Ferguson 1999; Rorig and Ferguson 2002). DD_{850} and T_{max} are strongly enhanced, with large areas showing increases of >6°C for both variables on dry versus wet lightning days (figures 3(Q), (R)). Our findings demonstrate that considerably hotter and drier conditions exist in the lower troposphere when lightning occurs as dry across this region. These results agree with previous studies that reported significantly increased DD_{850} on dry versus wet lightning days over the northwest United States (Rorig and Ferguson 1999), northern Rockies (Rorig and Ferguson 2002), and southeastern Australia (Dowdy and Mills 2012b) sufficient to evaporate rainfall before it reaches the ground (i.e., "virga"). Stronger surface heating, reflected by higher T_{max} across the domain compared to wet lightning days (figure 3(R)), contributes to enhanced lower-tropospheric dryness and greater mid-tropospheric instability congruent with previous studies (e.g., Rorig and Ferguson 1999; Rorig and Ferguson 2002).

We note that a limitation of our composite analysis is that we examine these variables in isolation and do not elucidate the concurrence of multiple variables initiating dry lightning. Wallmann *et al* (2010), for example, found that UTLR of >7.5°C km^{-1} is an important indicator of dry lightning but only when combined with sufficient low- or mid-tropospheric moisture, and Rorig and Ferguson (1999) developed a dry lightning classification scheme that considered the 850-500 hPa lapse rate and DD_{850} simultaneously. More broadly, Nauslar *et al* (2013) showed that the most likely zones for dry lightning exist at the periphery of high-moisture and high-instability environments, where convection can produce dry lightning but without sufficient

moisture to produce “wetting” rain. A multivariate approach could improve our understanding of these relationships and help operational forecasters and fire management entities better anticipate dry lightning at longer lead-times than are currently available (Nauslar *et al* 2013).

3.3. Climatology of widespread dry lightning outbreaks

Widespread dry lightning days (dry lightning in >6.1% of the domain) have occurred throughout the warm season (figure 4(A)). Although the majority of these days occurred during July-August, the largest spatial extents occurred in June and September (figures 4(A), (C)). Widespread dry lightning outbreaks, on average, occurred over higher elevations during May-August and lower elevations in September-October (figure 4(A), brown line). Figure 4(B) shows the largest 1-day (orange) and 2-day (red) dry lightning outbreaks, and the total number of widespread dry lightning days in each year (blue bars). There is substantial interannual variability in outbreak frequency and spatial extents. Two-day outbreak spatial extents affecting >20% of the domain have occurred in 8 of these years (1987, 1988, 1990, 1991, 2003, 2008, 2017 and 2020; figure 4(B)). Some observational uncertainty exists in the early part of the record due to lower detection efficiency of the NLDN network, particularly before a major network upgrade in 1995 (Cummins and Murphy 2009). Nonetheless, we find frequent widespread dry lightning days and large spatial extents of dry lightning between 1987 and 1995. In contrast, relatively few widespread dry lightning days have occurred since 2015 (figure 4(B), blue bars).

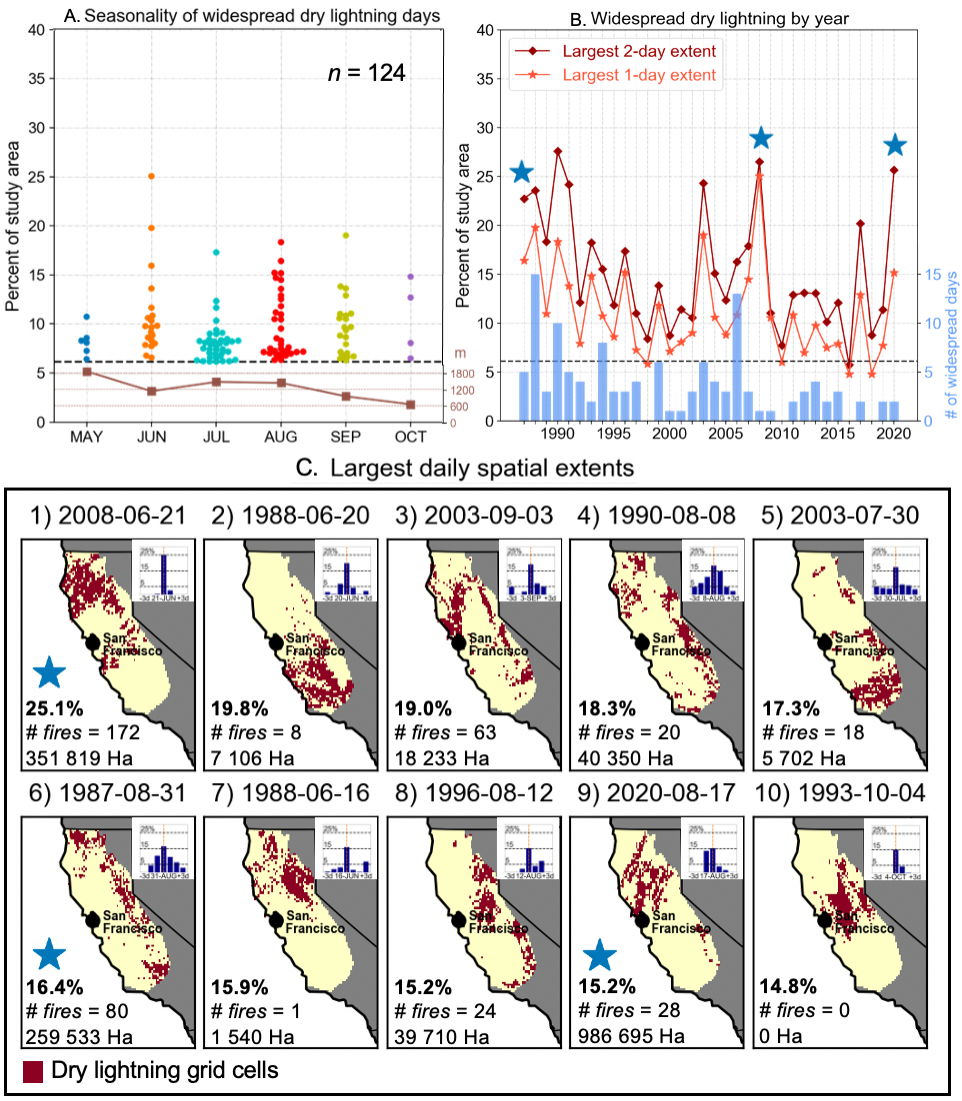

Figure 4. (A) Monthly distribution of the 124 widespread dry lightning days (dry lightning in >6.1% of all 0.1° NLDN grid cells) between May-October 1987-2020 and median elevation of affected grid cells on these days (brown line). (B) Maximum annual dry lightning extent (percentage of all grid cells in domain) defined over 1-day (orange) and 2-day (red) periods. For 2-day periods, only unique grid cells are counted. Data points in (A) are jittered for visualization within each month. In (A) and (B), dashed black line represents the fraction of grid cells (6.1%) corresponding to the 95th percentile of all daily spatial extents of dry lightning over the 34-year period. Blue bars in (B) show the number of widespread dry lightning days defined at this threshold in each year. (C) Top-10 largest daily spatial extents of dry lightning over the study period. In (C), bold inset text indicates the percentage of grid cells experiencing dry lightning on that day, and inset bar charts show the daily spatial extents of dry lightning in the 7-day window centered on that day. Other inset text shows the number of associated lightning-caused wildfires ignited during the 7-day period and the final burned area from such fires (see *Materials and Methods*)

from CAL FIRE. Blue markers in (B) and (C) denote widespread dry lightning outbreaks discussed in the text.

The largest lightning-caused wildfire outbreaks, measured by burned area, started on or around 31 August 1987 (~260 000ha), 21 June 2008 (~352 000ha), and 17 August 2020 (987 000ha), which were also three of the ten most widespread dry lightning days (figure 4(C)). The "Siege of 1987" wildfire outbreak (Duclos *et al* 1990) resulted from four consecutive days of widespread dry lightning (30 August – 2 September) peaking at 16.4% of the domain on 31 August over mainly forested regions of the Sierra Nevada, Cascades, and Klamath Mountains (figure 4(C)). The "exceptional" dry lightning outbreak of 21 June 2008 represents the largest single-day spatial extent of 25.1% and affected a large swath of northern California (figure 4(C)) (Wallmann *et al* 2010), resulting in the 8th largest lightning-caused fire over this domain in the 34-year record (Basin Complex, ~66 000ha). The dry lightning outbreak of 16-17 August 2020 ignited the August Complex, SCU Lightning Complex, LNU Lightning Complex, and North Complex fires – the 1st, 4th, 6th, and 7th largest fires on record in California – contributing to the state's largest annual burned area in modern records (Keeley and Syphard 2021). The 2-day outbreak together affected ~25.7% of the domain even though the individual daily spatial extents were less remarkable peaking at 15.2% on 17 August (figures 4(B), (C)). Notably, the 2008 and 2020 outbreaks represented the only widespread dry lightning days in their respective years (figure 4(B), blue bars), emphasizing the importance of rare but extreme dry lightning outbreaks as drivers of extreme wildfire episodes in this region.

We test the sensitivity of our dry lightning climatology to our choice of precipitation dataset by comparing key climatological characteristics identified above using gridMET with the climatology created using the Multi-Source Weighted Ensemble Precipitation (MSWEP) V2.8

dataset (Beck *et al* 2019) at a 0.1° resolution (http://www.gloh2o.org/mswep/; 1979-present). MSWEP combines precipitation data from surface gauges, satellites, and reanalysis. Compared to other high spatial and temporal resolution multi-source precipitation datasets, MSWEP is available for the entire analysis period. Daily precipitation totals provided by MSWEP are binned 5 PM-5 PM local time and thus match the temporal aggregation of the NLDN data. Although gridMET and MSWEP are created from different data sources and over different daily timesteps, the spatial patterns of mean lightning density and dry lightning fraction and monthly differences in dry lightning characteristics at different elevations are generally similar over 1987-2020 (figures S.(5)-(7)). A notable difference is the larger dry lightning fraction over northeastern areas when using MSWEP (figure S.5(D)), which could result from different temporal aggregation in these datasets or differences in input data sources. Additionally, the coarser spatial resolution of MSWEP compared to gridMET might lead to averaging of sub-grid rainfall over each grid point, possibly causing more grid points to fall below the dry lightning threshold (<2.5mm). Although MSWEP may be expected to capture more precipitation than the gauge-based gridMET over sparsely-gauged regions (e.g., Sierra Nevada), the accuracy of satellite and reanalysis precipitation inputs in the presence of dry sub-cloud environments that lead to virga is unknown. In addition, the widespread dry lightning days are largely consistent between the two datasets, with slight differences in the identified extents.

3.4. Clustering of large-scale atmospheric patterns on widespread dry lightning days

We identify four main types of weather patterns associated with dry lightning outbreaks in different parts of the domain. Figure 5 shows the four clusters representing the large-scale atmospheric patterns on widespread dry lightning days, their associated meteorological

conditions, and the spatial patterns of dry lightning likelihood across the region. All clusters exhibit mid-tropospheric high-pressure ridging centered over different portions of the western North American continental interior (as indicated by higher values of 500 hPa geopotential heights (Z_{500}), figures 5(A)-(D)).

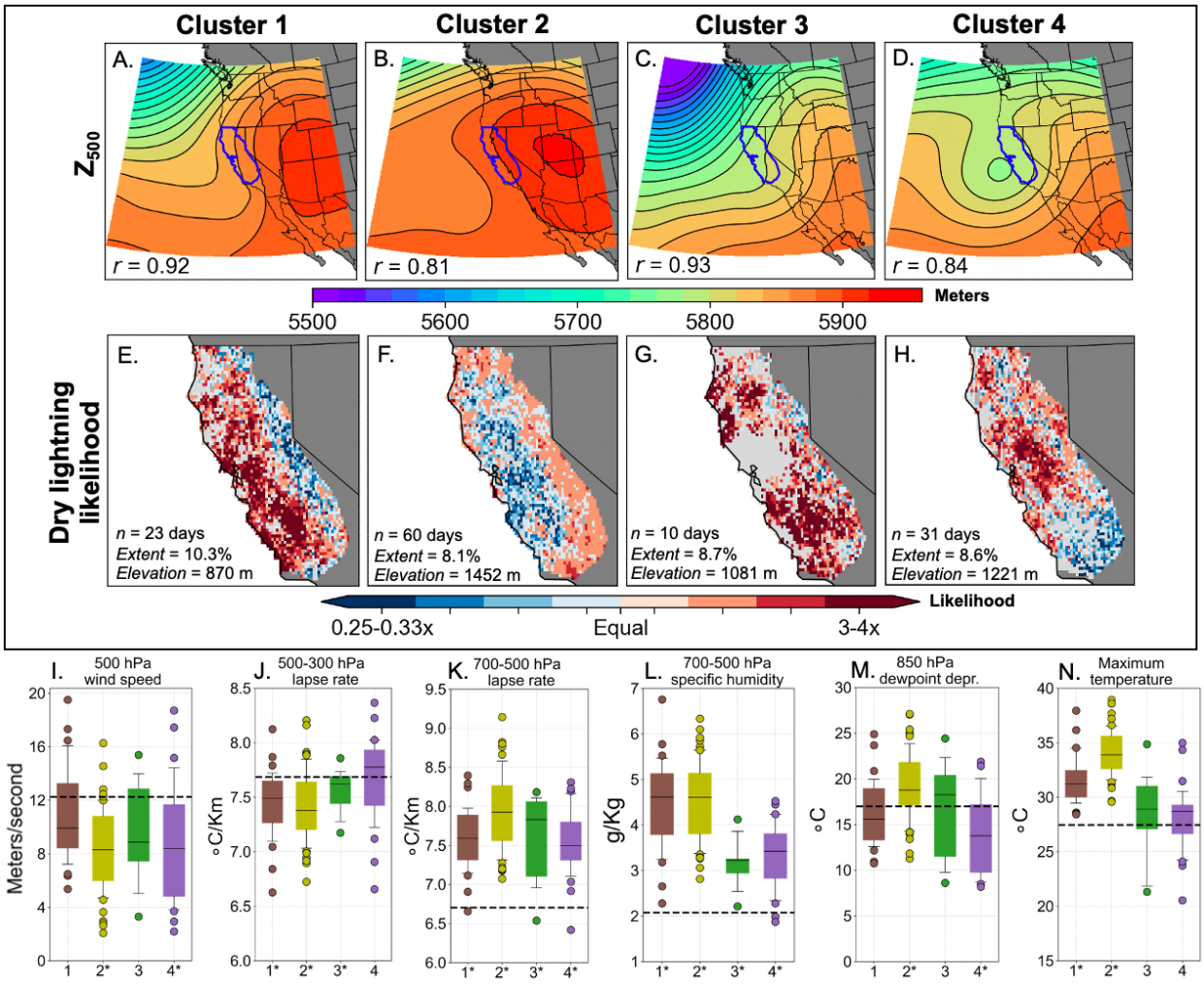

Figure 5. (A-D) *k*-means clusters of 500 hPa geopotential heights (Z_{500}) on widespread dry lightning days during May-October 1987-2020 (*n* = 124). The domain outline is shown in blue. Inset text indicates median 2-D pattern correlation (*r*) between the cluster's composite and constituent daily patterns. (E-H) Dry lightning likelihood in each grid cell associated with that cluster's Z_{500} pattern, relative to random chance. For example, dark red shading indicates that on widespread dry lightning days, these grid cells are >3 times more likely to experience dry lightning with that cluster's Z_{500} pattern compared to random chance. Light gray shading denotes grid cells which have not been constituent to a widespread dry

lightning day with that cluster. (I-N) Boxplots of domain-averaged meteorological variables on widespread dry lightning days for each cluster. Asterisks next to cluster names denote significant difference ($P < 0.05$) of that cluster's distribution compared to all non-widespread days (dry lightning in <6.1% of domain including no dry lightning) in the 34-year record according to a Kolmogorov-Smirnov test. Inset text in (E-H) shows the number of days assigned to each cluster and the median extent and elevation of all grid cells affected on widespread dry lightning days in that cluster. Dashed lines in (I-N) indicate the domain-averaged value of each variable on non-widespread days.

Cluster 1 features a strong ridge over the continental interior, with offshore troughing likely providing dynamic lifting and enhancing mid-tropospheric moisture transport to the region, particularly if tropical moisture is readily available over the eastern Pacific Ocean (figure 5(A)). For example, the August 2020 dry lightning outbreak – a cluster 1 pattern – developed after the circulation of an approaching shortwave trough interacted with Tropical Storm Fausto in the eastern tropical Pacific (Blake 2021), sending large amounts of mid-tropospheric moisture northward over California that was sufficient to initiate widespread elevated convection. Cluster 1 is associated with increased dry lightning likelihood throughout the domain outside of the Sierra Nevada, the largest median dry lightning spatial extent (~10.3%), and the lowest median elevation of dry lightning (870m, figure 5(E)). Cluster 2 shows a broad, amplified ridge extending over the Pacific coastal states northward to Canada (figure 5(B)). This pattern is associated with enhanced dry lightning likelihood over the Sierra Nevada and the highest median elevation of dry lightning (1452m, figure 5(F)). Cluster 3 shows weaker ridging over the continental interior and strong, amplified troughing offshore centered over the northeast Pacific Ocean (figure 5(C)) with enhanced dry lightning likelihood everywhere except the central parts of the domain (figure 5(G)). Cluster 4 is a "closed low" pattern (figure 5(D)) and corresponds to enhanced dry lightning likelihood in northern and central areas of the domain with decreased likelihood in southern areas (figure 5(H)).

The large-scale atmospheric flow represented by clusters 1 and 3 – with ridging in the continental interior and troughing offshore – resembles the "transitional" weather pattern following high pressure ridge breakdown identified by previous studies as favorable for warm-season lightning outbreaks over broad areas of the western United States (figures 5(A), (C)) (e.g., Abatzoglou and Brown 2009; Dettinger *et al* 1999; Kalashnikov *et al* 2020; Rorig and Ferguson 1999; Werth and Ochoa 1993). These patterns are conducive to shortwave troughs transiting the region from west to east, which have produced some of the most widespread dry lightning outbreaks over northern California including both the 2008 (cluster 3) and 2020 (cluster 1) outbreaks (Nauslar *et al* 2013; Wallmann *et al* 2010). In contrast, cluster 2 does not produce widespread dry lightning outbreaks over many lowland areas (figure 5(F)). Rather, this is a common summertime lightning pattern over mainly high terrain during the North American Monsoon season, as northward extension of ridging over the coastal states promotes monsoonal moisture transport, which combines with orographic lifting to initiate convection over mountains (figure 5(B)) (Abatzoglou and Brown 2009; Kalashnikov *et al* 2020). Indeed, cluster 2 accounts for 60 of the 124 observed widespread dry lightning days (figure 2(F)), and 50 of these days occurred during July-August representing peak monsoon season (figure S.8(B)). The dry lightning outbreak of 31 August 1987 is an example of a cluster 2 pattern, affecting mainly areas over high terrain (figure 4(C)).

Domain-averaged meteorological variables further illustrate the dynamic (figure 5(I)) and thermodynamic (figures 5(J)-(N)) conditions associated with each cluster. Cluster 1, associated with the most widespread median dry lightning spatial extent and occurring at the lowest elevations (figure 5(E)), features the strongest average UV_{500} among all clusters of ~9.9 m s^{-1} (figure 5(I)), supporting the earlier finding of stronger mid-tropospheric winds on dry lightning

days in these areas compared to higher elevations. The median UTLR values associated with Clusters 1-3 range from 7.4-7.6°C km^{-1} and are below the climatological average of 7.7°C km^{-1} computed from all other days (figure 5(J)), while Cluster 4 has the highest median ULTR of 7.8°C km^{-1}. All clusters show significant enhancement of MTLR and $Q_{700\text{-}500}$ compared to background climatology (figures 5(K), (L)), reinforcing the importance of increased mid-tropospheric instability and moisture in promoting widespread dry lightning outbreaks across this region irrespective of the synoptic configuration. Cluster 2, associated with a strong ridge of high pressure over the coastal states and the highest median elevation of dry lightning risk, exhibits the largest values of MTLR, $Q_{700\text{-}500}$, DD_{850} and T_{max} (figures 5(K)-(N)) yet shows decreased dry lightning likelihood in most of the low-elevation areas (figure 5(F)). This suggests the importance of atmospheric features associated with the other three clusters in causing dry lightning over lower elevations, including troughing (clusters 1 and 3) and closed lows (cluster 4; figures 5(A), (C)-(D)). These patterns can provide favorable mid-and upper-level dynamics, in addition to enhanced instability and moisture transport, to support warm-season convection over low-elevation areas, which lack orographic lifting and low-level forcing typically associated with thunderstorm development (Nauslar *et al* 2013; Wallmann *et al* 2010).

4. Summary and Conclusions

In this study we have developed the first long-term and spatially contiguous climatology of dry lightning and examined its elevational dependence in central and northern California – a highly populated region that has experienced numerous destructive lightning-caused wildfires in recent decades. We identify local and large-scale meteorological conditions associated with such dry lightning outbreaks. Our work builds on previous studies of individual dry lightning

outbreaks (e.g., Nauslar *et al* 2013; Wallmann *et al* 2010) and distinguishes the meteorological conditions associated with dry versus wet lightning. We demonstrate that dry lightning preferentially occurs at higher elevations and peaks during July-August, while lower elevations account for a larger proportion of dry lightning during September-October – representing a reversal of the relationship between dry lightning and elevation during the transition from summer to fall. We show that many low-elevation locations experience a large fraction of their lightning occurring as dry (versus wet) and experience a longer dry lightning season extending into fall (figures 2(B), (C)). This is particularly important since both live and dead fuels tend to be extremely dry before the arrival of cool-season rains, further elevating the risk of wildfires late in the burning season (Balch *et al* 2018; Court 1960; Goss *et al* 2020).

We conduct a composite analysis of meteorological conditions on dry lightning days at each grid cell across the varied geography of this region. We show that two thermodynamically related variables – MTLR and $Q_{700\text{-}500}$ – are consistently above background climatology across the region on dry lightning days (figures 3(I), (J)), indicating that enhanced mid-tropospheric instability and moisture are key meteorological ingredients for dry lightning. Compared to wet lightning, we find that dry lightning occurs with considerably greater values of T_{max}, DD_{850}, and MTLR across the domain suggesting a much hotter, drier lower troposphere with greater mid-tropospheric instability when lightning occurs during dry versus wet thunderstorms (figures 3(P)-(R)). We find greater UV_{500} and $Q_{700\text{-}500}$ on dry lightning days over lower elevations, suggesting stronger mid-tropospheric steering flow and moisture enhancement in these parts of the domain compared to when dry lightning occurs over higher terrain. We also find steeper UTLR over northern areas, indicating greater upper-tropospheric instability on dry lightning days there compared to southern areas.

Widespread dry lightning outbreaks create the potential for multiple simultaneous wildfire ignitions that can severely impact fire suppression efforts due to the geographic dispersion of ignitions and the potential for substantial resource commitments. In this study, we present the first assessment of the climatology and spatial extents of these dry lightning outbreaks across this region. While the majority of widespread dry lightning days occurred in July-August consistent with overall dry lightning climatology, they also occurred throughout the warm season with the largest spatial extents observed in June and September, respectively (figure 4(A)). Although vegetation, antecedent climate, and post-ignition weather conditions modulate wildfire extent, the largest lightning-caused wildfire burned areas in the 34-year record nonetheless resulted from widespread dry lightning outbreaks centered on 31 August 1987, 21 June 2008, and 17 August 2020 (figure 4(C)). Our findings indicate that large dry lightning outbreaks can occur in otherwise "quiet" years for dry-lightning activity as was demonstrated in 2008 and 2020, when some of the most widespread dry lightning days on record ignited numerous wildfires leading to costly and destructive wildfire seasons, despite a lack of any other widespread dry lightning days in those years (figures 4(B), (C)). We identify four types of large-scale atmospheric patterns associated with widespread dry lightning outbreaks over this region. All four patterns are associated with different configurations of high pressure ridging over the continental interior, three of which additionally feature offshore troughing that provides a lifting mechanism and promotes moisture transport into the region (figures 5(A), (C)-(D)).

As our study domain is a highly populated region prone to lightning-caused wildfires, understanding the climatology and meteorology of dry lightning is critical for informing operational forecasts and climate model projections of dry lightning risk across the varied geography found here. Increased forecast accuracy of dry lightning outbreaks can aid fire

suppression efforts, as firefighting resources can be strategically pre-positioned in at-risk areas. Finally, our findings regarding dry lightning are also relevant to efforts aimed at better constraining future risk of wildfire ignition in California from climate model projections – independent of changes to fire weather, biophysical factors, or human ignitions across this region.

REFERENCES

Abatzoglou J T 2016 Contribution of Cutoff Lows to Precipitation across the United States *J Appl Meteorol Climatol* **55** 893–899

Abatzoglou J T 2013 Development of gridded surface meteorological data for ecological applications and modelling *Int J Climatol* **33** 121–131

Abatzoglou J T and Brown T J 2009 Influence of the Madden–Julian Oscillation on Summertime Cloud-to-Ground Lightning Activity over the Continental United States *Mon Weather Rev* **137** 3596–3601

Abatzoglou J T, Kolden C A, Balch J K and Bradley B A 2016 Controls on interannual variability in lightning-caused fire activity in the western US *Environ Res Lett* **11** 045005

Abatzoglou J T and Williams A P 2016 Impact of anthropogenic climate change on wildfire across western US forests *Proc Natl Acad Sci* **113** 11770–11775

Balch J K, Bradley B A, Abatzoglou J T, Nagy R C, Fusco E J and Mahood A L 2017 Human-started wildfires expand the fire niche across the United States *Proc Natl Acad Sci* **114** 2946–2951

Balch J K, Schoennagel T, Williams A P, Abatzoglou J T, Cattau M E, Mietkiewicz N P and St. Denis L A 2018 Switching on the Big Burn of 2017 *Fire* **1** 9 pp

Barbero R, Abatzoglou J T, Steel E A and Larkin N K 2014 Modeling very large-fire occurrences over the continental United States from weather and climate forcing *Environ Res Lett* **9** 124009

Bartlein P J, Hostetler S W, Shafer S L, Holman J O and Solomon A M 2008 Temporal and spatial structure in a daily wildfire-start data set from the western United States (1986–96) *Int J Wildland Fire* **17** 8–17

Bates B C, Dowdy A J and Chandler R E 2017 Classification of Australian Thunderstorms Using Multivariate Analyses of Large-Scale Atmospheric Variables *J Appl Meteorol Climatol* **56** 1921–1937

Beck H E, Wood E F, Pan M, Fisher C K, Miralles D G, van Dijk A I J M *et al* 2019 MSWEP V2 global 3-hourly 0.1° precipitation: Methodology and quantitative assessment *Bull Am Meteorol Soc* **100** 473-500

Bertram I and Mayr G J 2004 Lightning in the eastern Alps 1993-1999, part I: Thunderstorm tracks *Nat Hazards Earth Syst Sci* **4** 501–511

Blake E 2021 Tropical Storm Fausto National Hurricane Center Tropical Cyclone Report *National Hurricane Center* 8 pp https://www.nhc.noaa.gov/data/tcr/EP112020_Fausto.pdf

Brey S J, Barnes E A, Pierce J R, Wiedinmyer C and Fischer E V 2018 Environmental Conditions, Ignition Type, and Air Quality Impacts of Wildfires in the Southeastern and Western United States *Earths Future* **6** 1442–1456

Chen B and Jin Y 2022 Spatial patterns and drivers for wildfire ignitions in California *Environ Res Lett* **17** 055004

Copernicus Climate Change Service (C3S) 2017 ERA5: Fifth generation of ECMWF atmospheric reanalyses of the global climate *Copernicus Climate Change Service Climate Data Store (CDS)*

Court A 1960 Thunderstorm Frequency in Northern California *Bull Am Meteorol Soc* **41** 406-409

Cummins K L and Murphy M J 2009 An Overview of Lightning Locating Systems: History, Techniques, and Data Uses, With an In-Depth Look at the U.S. NLDN *IEEE Trans Electromagn Compat* **51** 499–518

Dettinger M D, Cayan D R and Brown T J 1999 Summertime intraseasonal and interannual lightning variations in the western United States *Proc 24th Annual NOAA Clim Diagn and Pred Workshop, Tucson, Arizona, Nov 1-5, 1999*

Detzer J, Loikith P C, Pampuch L A, Mechoso C R, Barkhordarian A and Lee H 2020 Characterizing monthly temperature variability states and associated meteorology across southern South America *Int J Climatol* **40** 492–508

Doswell C A III and Rasmussen E N 1994 The effect of neglecting the virtual temperature correction on CAPE calculations *Weather Forecast* **9** 625-629

Dowdy A J 2020 Climatology of thunderstorms, convective rainfall and dry lightning environments in Australia *Clim Dyn* **54** 3041–3052

Dowdy A J and Mills GA 2012a Atmospheric and Fuel Moisture Characteristics Associated with Lightning-Attributed Fires *J Appl Meteorol Climatol* **51** 2025–2037

Dowdy A J and Mills G A 2012b Characteristics of lightning-attributed wildland fires in south-east Australia *Int J Wildland Fire* **21** 521–524

Duclos P, Sanderson L M and Lipsett M 1990 The 1987 Forest Fire Disaster in California: Assessment of Emergency Room Visits *Arch Environ Health Int J* **45** 53–58

Easterling D R and Robinson P J 1985 The Diurnal Variation of Thunderstorm Activity in the United States *J Appl Meteorol Climatol* **24** 1048–1058

Goss M, Swain D L, Abatzoglou J T, Sarhadi A, Kolden C A, Williams A P *et al* 2020 Climate change is increasing the likelihood of extreme autumn wildfire conditions across California *Environ Res Lett* **15** 094016

Grotjahn R, Black R, Leung R, Wehner M F, Barlow M, Bosilovich M *et al* 2016 North American extreme temperature events and related large scale meteorological patterns: a review of statistical methods, dynamics, modeling, and trends *Clim Dyn* **46** 1151–1184

Hantson S, Andela N, Goulden M L and Randerson J T 2022 Human-ignited fires result in more extreme fire behavior and ecosystem impacts *Nature Comm* **13** 2717

Hersbach H, Bell B, Berrisford P, Hirahara S, Horányi A, Muñoz-Sabater J *et al* 2020 The ERA5 global reanalysis *Q J R Meteorol Soc* **146** 1999–2049

Kalashnikov D A, Loikith P C, Catalano A J, Waliser D E, Lee H and Abatzoglou J T 2020 A 30-Yr Climatology of Meteorological Conditions Associated with Lightning Days in the Interior Western United States *J Clim* **33** 3771–3785

Kalashnikov D A, Schnell J L, Abatzoglou J T, Swain D L and Singh D 2022 Increasing co-occurrence of fine particulate matter and ground-level ozone extremes in the western United States *Sci Adv* **8** eabi9386

Keeley J E and Syphard A D 2021 Large California wildfires: 2020 fires in historical context *Fire Ecol* **17** 11 pp

Keeley J E and Syphard A D 2018 Historical patterns of wildfire ignition sources in California ecosystems *Int J Wildland Fire* **27** 781–799

Komarek E V Sr 1967 The Nature of Lightning Fires *Proc 7th Tall Timbers Fire Ecol Conf* 5-41

MacNamara B R, Schultz C J and Fuelberg H E 2020 Flash Characteristics and Precipitation Metrics of Western U.S. Lightning-Initiated Wildfires from 2017 *Fire* **3** 19 pp

MacQueen J 1967 Some methods for classification and analysis of multivariate observations *Proc Fifth Berkeley Symp Math Stat Probab* **1** 281-297

Maddox R A, Canova F and Hoxit L R 1980 Meteorological Characteristics of Flash Flood Events over the Western United States *Mon Weather Rev* **108** 1866–1877

May R M, Arms S C, Marsh P, Bruning E, Leeman J R, Goebbert K *et al* 2021 MetPy: A Python Package for Meteorological Data *Unidata* https://github.com/Unidata/MetPy

Miller J D, Skinner C N, Safford H D, Knapp E E and Ramirez C M 2012 Trends and causes of severity, size, and number of fires in northwestern California, USA *Ecol Appl* **22** 184–203

Moore B J, White A B and Gottas D J 2021 Characteristics of Long-Duration Heavy Precipitation Events along the West Coast of the United States *Mon Weather Rev* **149** 2255–2277

Nauslar N, Kaplan M, Wallmann J and Brown T 2013 A forecast procedure for dry thunderstorms *J Oper Meteorol* **1** 200–214

Parks S A and Abatzoglou J T 2020 Warmer and Drier Fire Seasons Contribute to Increases in Area Burned at High Severity in Western US Forests From 1985 to 2017 *Geophys Res Lett* **47** e2020GL089858

Podschwit H and Cullen A 2020 Patterns and trends in simultaneous wildfire activity in the United States from 1984 to 2015 *Int J Wildland Fire* **29** 1057-1071

Rochette S M, Moore J T and Market P S 1999 The importance of parcel choice in elevated CAPE computations *Natl Wea Dig* **23** 20-32

Rorig M L and Ferguson S A 1999 Characteristics of Lightning and Wildland Fire Ignition in the Pacific Northwest *J Appl Meteorol Climatol* **38** 1565–1575

Rorig M L and Ferguson S A 2002 The 2000 Fire Season: Lightning-Caused Fires *J Appl Meteorol Climatol* **41** 786–791

Rorig M L, McKay S J, Ferguson S A and Werth P 2007 Model-Generated Predictions of Dry Thunderstorm Potential *J Appl Meteorol Climatol* **46** 605–614

Schultz C J, Nauslar N J, Wachter J B, Hain C R and Bell J R 2019 Spatial, Temporal and Electrical Characteristics of Lightning in Reported Lightning-Initiated Wildfire Events *Fire* **2** 15 pp

Show S B and Kotok E I 1923 Forest Fires in California from 1911-1920: An Analytical Study *U S Dep Agric Dep Circ 243*

Soriano L J R, Pablo F D and Diez E L G 2001 Meteorological and geo-orographical relationships with lightning activity in Castilla-Leon (Spain) *Meteorol Appl* **8** 169–175

Tardy A 2001 Combining numerical model and observed soundings with VIL Density to forecast severe thunderstorms in the Sierra Nevada *Western Reg Tech Attach No 01-05* https://www.weather.gov/media/wrh/online_publications/TAs/ta0105.pdf

Tardy A 2002 The northern Sacramento Valley surface moisture convergence zone *Western Reg Tech Attach No 02-07* https://www.weather.gov/media/wrh/online_publications/TAs/ta0207.pdf

Taszarek M, Brooks H E, Czerneki B, Szuster P and Fortuniak K 2018 Climatological aspects of convective parameters over Europe: A comparison of ERA-Interim and sounding data *J Clim* **31** 4281-4308

van Wagtendonk J W 1994 Spatial patterns of lightning strikes and fires in Yosemite National Park *Proc of the 12th Conf on Fire and Forest Meteorol* 223-231

van Wagtendonk J W and Cayan D R 2008 Temporal and Spatial Distribution of Lightning Strikes in California in Relation to Large-Scale Weather Patterns *Fire Ecol* **4** 34–56

Visualization & Analysis Systems Technologies (VAST) 2021 Geoscience Community Analysis

Toolkit (GeoCAT-comp version 2021.5.1) [Software] *Boulder, CO: UCAR/NCAR - Computational and Informational System Lab*

Wallmann J, Milne R, Smallcomb C and Mehle M 2010 Using the 21 June 2008 California Lightning Outbreak to Improve Dry Lightning Forecast Procedures *Weather Forecast* **25** 1447–1462

Werth P and Ochoa R 1993 The Evaluation of Idaho Wildfire Growth Using the Haines Index *Weather Forecast* **8** 223–234

Williams A P, Abatzoglou J T, Gershunov A, Guzman-Morales J, Bishop D A, Balch J K *et al* 2019 Observed Impacts of Anthropogenic Climate Change on Wildfire in California *Earths Future* **7** 892–910

ACKNOWLEDGMENTS

We thank two anonymous reviewers for their insightful comments that helped improve this paper. We acknowledge ECMWF's Copernicus Climate Change Service for providing ERA5 data, and Vaisala for collecting the NLDN lightning data used in this study. We sincerely thank Jim Wallmann for input regarding meteorological variables. This research used resources from the Center for Institutional Research Computing at Washington State University. DAK and DS were supported by NASA FINESST award 80NSSC21K1603. DLS was supported by a collaboration between the Institute of the Environment and Sustainability at the University of California, Los Angeles; the Center for Climate and Weather Extremes at the National Center for Atmospheric Research; and the Nature Conservancy of California. JTA was supported by NSF award OAI-2019762. DT was supported by the National Center for Atmospheric Research,

which is a major facility sponsored by the National Science Foundation under Cooperative Agreement No. 1755088.

CHAPTER FOUR: LIGHTNING-IGNITED WILDFIRES IN THE WESTERN UNITED STATES: IGNITION PRECIPITATION AND ASSOCIATED ENVIRONMENTAL CONDITIONS

Kalashnikov, D. A., Abatzoglou, J. T., Loikith, P. C., Nauslar, N. J., Bekris, Y., & Singh, D. (2023). Lightning-ignited wildfires in the western United States: Ignition precipitation and associated environmental conditions. *Geophysical Research Letters*, *50*(16), e2023GL103785. DOI: 10.1029/2023GL103785

Originally published in *Geophysical Research Letters* and reproduced here in its original format.

Attributions:

Dmitri A. Kalashnikov designed the research, performed all analyses, and wrote the manuscript. D. Singh provided supervision and research direction, and helped edit the manuscript. J.T. Abatzoglou, P.C. Loikith, N.J. Nauslar, and Y. Bekris provided feedback on the research and helped edit the manuscript.

Abstract

Cloud-to-ground lightning with minimal rainfall ("dry" lightning) is a major wildfire ignition source in the western United States (WUS). Although dry lightning is commonly defined as occurring with <2.5mm of daily-accumulated precipitation, a rigorous quantification of precipitation amounts concurrent with lightning-ignited wildfires is lacking. We combine wildfire, lightning and precipitation datasets to quantify these ignition precipitation amounts across ecoprovinces of the WUS. The median precipitation for all lightning-ignited wildfires is 2.8mm but varies with vegetation and fire characteristics. "Holdover" fires not detected until 2-5 days following ignition occur with significantly higher precipitation (5.1mm) compared to fires detected promptly after ignition (2.5mm), and with cooler and wetter environmental conditions. Further, there is substantial variation in precipitation associated with promptly-detected (1.7-4.6mm) and holdover (3.0-7.7mm) fires across ecoprovinces. Consequently, the widely-used 2.5mm threshold does not fully capture lightning ignition risk and incorporating ecoprovince-specific precipitation amounts would better inform WUS wildfire prediction and management.

Plain Language Summary

Cloud-to-ground lightning with minimal rainfall, also known as "dry lightning," is a major wildfire ignition source in the western United States (WUS). Typically, daily-accumulated precipitation of less than 2.5mm is used to identify dry lightning occurrence. However, there is limited knowledge of i) the true precipitation amounts that occur with lightning-ignited wildfires, and ii) how these amounts vary across different landscapes and vegetation types. We combine wildfire, lightning and precipitation datasets to quantify these ignition precipitation amounts across different regions of the WUS. Although we find a 2.8mm median ignition precipitation for

all lightning-ignited wildfires, we show that "holdover" fires not detected until 2-5 days following ignition occur with significantly higher precipitation (5.1mm) compared to fires detected promptly after ignition (2.5mm). Holdover fires also occur with cooler and wetter environmental conditions. Further, ignition precipitation amounts associated with promptly-detected and holdover fires vary substantially across ecoprovinces. Consequently, the widely-used 2.5mm threshold does not fully capture lightning ignition risk. WUS wildfire prediction and management could be improved through incorporating ecoprovince-specific precipitation amounts and accounting for differing characteristics of holdover fires.

1 Introduction

Cloud-to-ground lightning without substantial accompanying rainfall ("dry lightning") is a major source of western United States (WUS) wildfire ignitions during summer, when fuels are typically dry (Abatzoglou et al., 2016; Balch et al., 2017; Brey et al., 2018). In August 2020, a large dry lightning outbreak ignited numerous simultaneous wildfires in California (Kalashnikov et al., 2022a), contributing to the largest annual wildfire burned area in the state's modern history (Keeley & Syphard, 2021) and prolonged hazardous air quality conditions across the WUS (Kalashnikov et al., 2022b; Zhou et al., 2021). Approximately 69% of WUS wildfire burned area is attributed to lightning-ignited wildfires (LIWs; Abatzoglou et al., 2016). LIW burned area is increasing (Cattau et al., 2020) and these trends are projected to continue under warming (Barros et al., 2021; Li et al., 2020). A better understanding of dry lightning and the environmental conditions shaping LIW risk can inform operational forecasting and future projections of LIWs.

Dry lightning is produced by thunderstorms that typically initiate at high altitudes (>3 km) due to moisture advection in the mid-troposphere, with substantially elevated cloud bases compared to heavy rain-producing thunderstorms (Fuquay, 1962; Krumm, 1954; Nauslar et al.,

2013; Rorig & Ferguson, 1999). These conditions coincide with increased mid-level instability and a dry lower troposphere, evaporating rainfall before reaching the ground and increasing LIW ignition risk (Kalashnikov et al., 2022a; Nauslar et al., 2013; Rorig & Ferguson, 1999; Wallmann et al., 2010). A daily precipitation amount of <2.5mm is widely used to define dry lightning over the interior WUS and similar dryland environments globally in both research (Abatzoglou et al., 2016; Dowdy, 2020; Dowdy & Mills, 2012; Kalashnikov et al., 2022a; Rorig & Ferguson, 1999) and operational forecasting (SPC 2022). Precipitation below this threshold is considered insufficient to prevent sustained wildfire ignition from cloud-to-ground lightning. However, other studies have shown varied precipitation amounts during LIWs. Using interpolated rain-gauge data, Hall (2007) found that most LIWs occur with <2mm/day precipitation in the southwest US. Using atmospheric reanalyses for the same region, Pérez-Invernón et al. (2022) reported a median precipitation of 0.2mm/hour accumulated during the hour of ignition. MacNamara et al. (2020) found median ignition precipitation amounts of 1.7mm/hour and 2.9mm/day using radar estimates over the WUS for LIWs in 2017. However, a comprehensive multi-year analysis of WUS LIW precipitation amounts does not yet exist.

Therefore, we quantify precipitation associated with LIWs across WUS ecoprovinces between 2015-2020 and examine associated environmental conditions. Some LIWs are not discovered for multiple days or weeks following ignition and are known as “holdover” fires (Schultz et al., 2019). For example, the 2021 Bootleg Fire in Oregon smoldered for more than one week before detection and ultimately grew into the state’s third-largest wildfire on record (Gorman, 2021). Such holdover fires might be associated with different environmental conditions and precipitation amounts (MacNamara et al., 2020). We therefore investigate ignition precipitation amounts and environmental conditions associated with holdover LIWs separately

from promptly-detected LIWs. Our findings advance the understanding of factors affecting LIW risk and are relevant to wildland fire prediction, suppression, and management across WUS sub-regions.

2 Materials and Methods

We conduct our analyses during May-September between 2015-2020, which corresponds to the summertime thunderstorm season over the interior WUS (Burrows et al., 2005; Kalashnikov et al., 2020; Rorig & Ferguson, 1999). Our analysis utilizes Bailey's ecoprovinces (USFS, 1995) to examine variations in precipitation amounts and environmental conditions associated with LIWs across different landscapes. Although each ecoprovince contains multiple vegetation types and land cover classifications, they represent regions of broadly similar climate, vegetation composition, and climate-fire relationships (Abatzoglou et al., 2016; Littell et al., 2009). We analyze the 16 ecoprovinces contained within the WUS.

2.1 Data

Wildfire data are from the National Interagency Fire Center (NIFC) – "Wildland Fire Locations Full History" dataset (WFIGS, 2022). This database provides fire discovery locations, dates, final burned areas, and fire cause type (e.g., human or natural). We consider all fires labeled as "natural" and constrain our analysis to >1 ha fires (Fusco et al., 2019a). Wildfire records geolocated within 0.01° latitude and longitude (~1 km) of another fire on the same day are flagged as duplicates and removed. A total of 4651 fires are identified using these criteria, representing a combined burned area of 5.79 million ha (Figure S1).

Cloud-to-ground lightning flashes are from the National Lightning Detection Network (NLDN; Vaisala, Inc.). We use daily accumulated precipitation from three gridded datasets:

NOAA *Multi-Radar/Multi-Sensor System (MRMS;* 1-km*)*; NASA's *Integrated Multi-satellitE Retrievals for GPM (IMERG;* 0.1°*)*; and *gridMET* (Abatzoglou, 2013; 4-km). These datasets were chosen to represent the three primary input data types for quantitative precipitation estimation - radar, satellite, and interpolated surface gauges, allowing for assessing uncertainties. Since we use gauge-corrected MRMS data ("GaugeCorr_QPE_01H") available starting 7 May 2015, we exclude ignitions between 1-6 May 2015. We assess differences in ignition precipitation amounts when aggregated by percent tree cover (as of 2020) using the Moderate Resolution Imaging Spectroradiometer (MODIS) "Vegetation Continuous Fields" dataset, and by fire size using the National Wildfire Coordinating Group (NWCG) fire size classes (https://www.nwcg.gov/term/glossary/size-class-of-fire).

To understand environmental conditions shaping LIW risk, we analyze daily surface variables representing atmospheric and fuel moisture conditions (vapor pressure deficit, maximum temperatures, 100- and 1000-hr dead fuel moisture on a 4-km grid) from gridMET since they can affect LIW ignition efficiency and overall burned area (Abatzoglou et al., 2016; Brey et al., 2020). Contemporaneous atmospheric conditions should affect moisture content and flammability of fine fuels. Meanwhile, the fuel moisture variables indicate the moisture content of medium (~3-8 cm diameter; 100-hr) to large (8-20 cm diameter; 1000-hr) dead woody debris.

2.2 Methods

Although the NIFC database provides latitude-longitude coordinates for each fire's discovery location, these may not represent the precise ignition location (Fusco et al., 2019a; Pérez-Invernón et al., 2022). Similarly, fire discovery dates are provided but they differ from ignition dates for holdover fires. Due to these spatiotemporal uncertainties, locations and dates of wildfire reports are refined using cloud-to-ground lightning data (Larjavaara et al., 2005; Schultz

et al., 2019). To match wildfires with lightning, we use a 2 km radius around every wildfire location to search for lightning (MacNamara et al., 2020; Nauslar, 2014), and consider the closest lightning location as the most likely ignition source. Although some studies have used larger search radii (Larjavaara et al., 2005; Moris et al., 2020; Pérez-Invernón et al., 2022; Pineda et al., 2022; Pineda & Rigo, 2017; Schultz et al., 2019), the smaller radius should reduce uncertainty in matching wildfire locations to potential igniting lightning flashes. This search radius also captures the ~1.6 km locational uncertainty ascribed to US federal wildfire reports (Short, 2014). NLDN lightning data also contain locational uncertainties of ~0.25 km (Nag, 2014), which can be larger in the mountainous terrain of the WUS (Schultz et al., 2019).

We search for lightning on the day of wildfire discovery (Lag 0), followed by the day prior (Lag 1). LIWs detected on Lag 0 or 1 are termed promptly-detected. If no cloud-to-ground lightning is found within 2 km on Lag 0 or 1, we sequentially search up to five days prior to fire discovery (Lag 2-5) until lightning is found or the search is exhausted. This imposes at least a 24-hour delay between ignition and discovery for such LIWs, termed as holdovers, as late afternoon and evening ignitions may not be reported until the following morning (Pineda & Rigo, 2017). The lightning flash closest to wildfire discovery time is considered the ignition source. We select a 5-day lag as a majority of LIWs are reported within a few days of ignition (MacNamara et al., 2020; Schultz et al., 2019). This window excludes rare longer-duration holdovers with increased uncertainty in the location of their ignition source (Schultz et al., 2019). Fires not paired with lightning within this window are excluded from further analysis.

For each fire, we use the lightning location and day to extract the precipitation amount and environmental variables from the overlying grid cell. We primarily use MRMS because of its high spatial resolution (1-km) and its use in prior studies (MacNamara et al., 2020). Due to the

areal coverage and proximity of ground-based radar beams, MRMS is expected to perform better when capturing convective precipitation over mountainous terrain of the WUS compared to gridMET and IMERG, particularly in areas with a sparse gauge network. Known limitations to using radar data over this region include a lack of adequate coverage in some areas (Vant-Hull et al., 2018) and possible overestimation of surface precipitation if rainfall evaporates before reaching the ground (Zhang et al., 2016). Therefore, we evaluate the sensitivity of our analysis to other precipitation datasets.

We compare the distributions of ignition precipitation amounts and environmental variables for promptly-detected LIWs with holdovers for each ecoprovince, and assess statistical significance of differences ($P < 0.10$) using the Mann-Whitney U test. For each ecoprovince and fire type, we use bootstrap resampling (n=1000 iterations) to test whether the median ignition precipitation is significantly different from 2.5mm. Differences are considered significant if the 90% confidence interval of resampled medians does not overlap 2.5mm.

3 Results and Discussion

3.1 Spatial patterns of lightning-ignited wildfires

Using our spatiotemporal search criteria, we matched 3726 of the 4651 (~80.1%) naturally-caused fires (>1 ha) across the WUS from the NIFC database with a cloud-to-ground lightning flash (Figure 1a). The percentage of matched fires is similar to MacNamara et al. (2020), who matched ~79.5% for 2017, but substantially higher than the ~59.6% over 2012-2015 reported by Schultz et al. (2019) using the same search radius but for larger fires (>400 ha). These differences likely reflect variation in geographic locations, fire size, and reporting conditions in the years analyzed in each study.

There are substantial variations in LIW occurrences across ecoprovinces, with the highest number of 717 LIWs in the Intermountain Semi-Desert that covers a large portion of the northern Great Basin (Figure 1a). Other ecoprovinces had 108-465 LIWs, except for five ecoprovinces in western Washington, Oregon, and California that had substantially fewer LIWs (0-6) and were excluded from subsequent analyses. The spatial pattern of identified LIWs is similar to the pattern of reported naturally-caused fires in the NIFC database (Figure 1a, S1). These patterns result from the greater lightning density in the interior WUS during summer compared to areas closer to the Pacific coast (Kalashnikov et al., 2020).

Of the 3726 identified WUS LIWs, 3157 (~84.7%) were promptly-detected while 569 (~15.3%) were holdovers (Figure 1b). The high percentage of promptly-detected LIWs is not surprising given that most fires are discovered soon after ignition, and a recent study over the southwest US found a median LIW holdover time of ~0.5 days (Pérez-Invernón et al., 2022). Similarly, Schultz et al. (2019) reported that ~78-80% of LIWs in the WUS were matched with a cloud-to-ground lightning flash on the same or prior day (see Figure 3 therein).

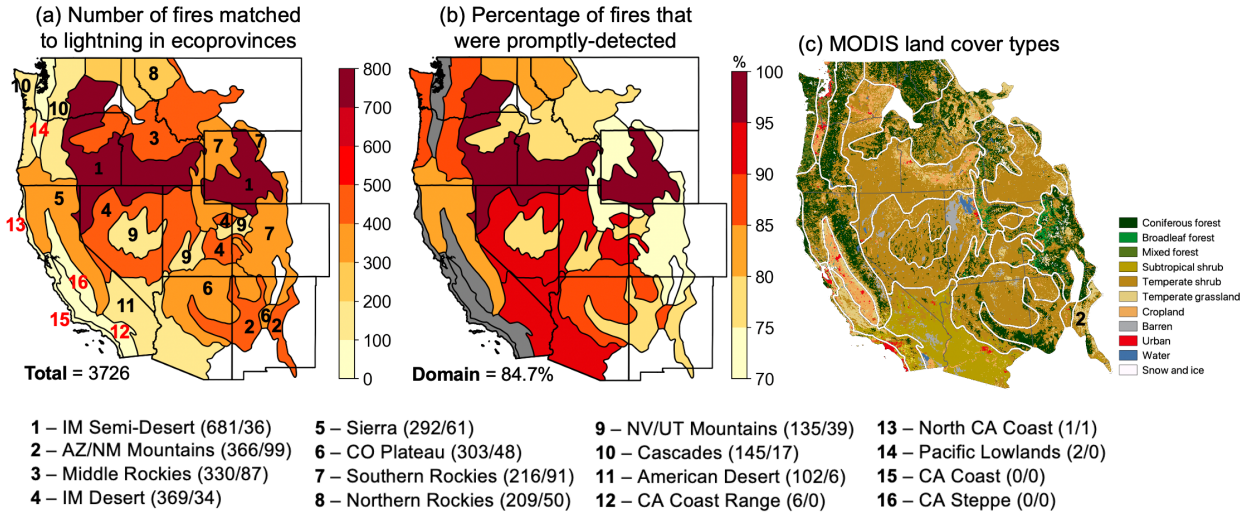

Figure 1. (a) Number of lightning-ignited wildfires (LIWs) in Bailey's ecoprovinces (May-September, 2015-2020). Numbers in (a) are ranks reflecting number of LIWs. Ecoprovinces labeled with red (#12-16) are excluded from further analysis due to low LIW numbers. (b) Percentage of total LIWs that were promptly-detected. Abbreviated ecoprovince names are shown below (see Table S1 for details), with the number of promptly-detected/holdover fires in parentheses. (c) MODIS land cover types (250m).

Across ecoprovinces, promptly-detected fires comprise 70-95% of total LIWs (Figure 1b). The desert and semi-desert environments of the Great Basin and interior Southwest (ecoprovinces #1, #4, and #11; Figure 1b-c) have the largest proportion of promptly-detected LIWs (>90%). Conversely, the highest proportion of holdovers (~20-30%) is found in the largely mountainous, forested terrain of the Arizona/New Mexico Mountains (#2), Middle and Southern Rockies (#3, #7) and Nevada/Utah Mountains (#9). In the Southern Rockies (#7), nearly a third of all LIWs are holdovers. In forested environments, deeper layers of fine organic fuels can ignite and smolder under the canopy even in conditions that are not favorable for flaming combustion, decreasing the likelihood of quick detection (Flannigan & Wotton, 1991; Pineda & Rigo, 2017). In contrast, in semi-desert and desert environments, sparser and patchier dispersion of fuels reduce smoldering while lack of canopy cover enables quick detection, potentially explaining the relative rarity of holdovers.

3.2 Precipitation amounts associated with lightning-ignited wildfires

Next, we evaluate systematic differences in precipitation amounts for promptly-detected and holdover LIWs (Figure 2). WUS-aggregated median holdover precipitation is more than double compared to promptly-detected LIWs (5.1 versus 2.5mm; $P < 0.10$), consistent with MacNamara et al. (2020). Further, eight of the 11 ecoprovinces have significantly higher median precipitation associated with holdover relative to promptly-detected LIWs (Figure 2a-b). Promptly-detected LIWs in most ecoprovinces have median precipitation amounts of <2.5mm

and as low as 1.7mm in the Intermountain Semi-Desert (Figure 2c), which is characterized by sagebrush steppe ecosystems and has the highest proportion of promptly-detected LIWs (~95%; Figure 1b). In contrast, all ecoprovinces have median precipitation for holdovers ≥3.0mm. Median ignition precipitation during holdovers in Northern and Southern Rockies, Arizona/New Mexico Mountains, and Intermountain Semi-Desert are at least 3mm higher than for promptly-detected LIWs (Figure 2c). Ecoprovinces with the highest holdover precipitation – Arizona/New Mexico Mountains, Northern and Southern Rockies, and Sierra (5.7-7.7mm) – are largely comprised of coniferous forests where canopy interception of precipitation and denser organic layers on the forest floor can sustain ignition in wetter conditions (Fischer et al., 2023; Flannigan & Wotton, 1991).

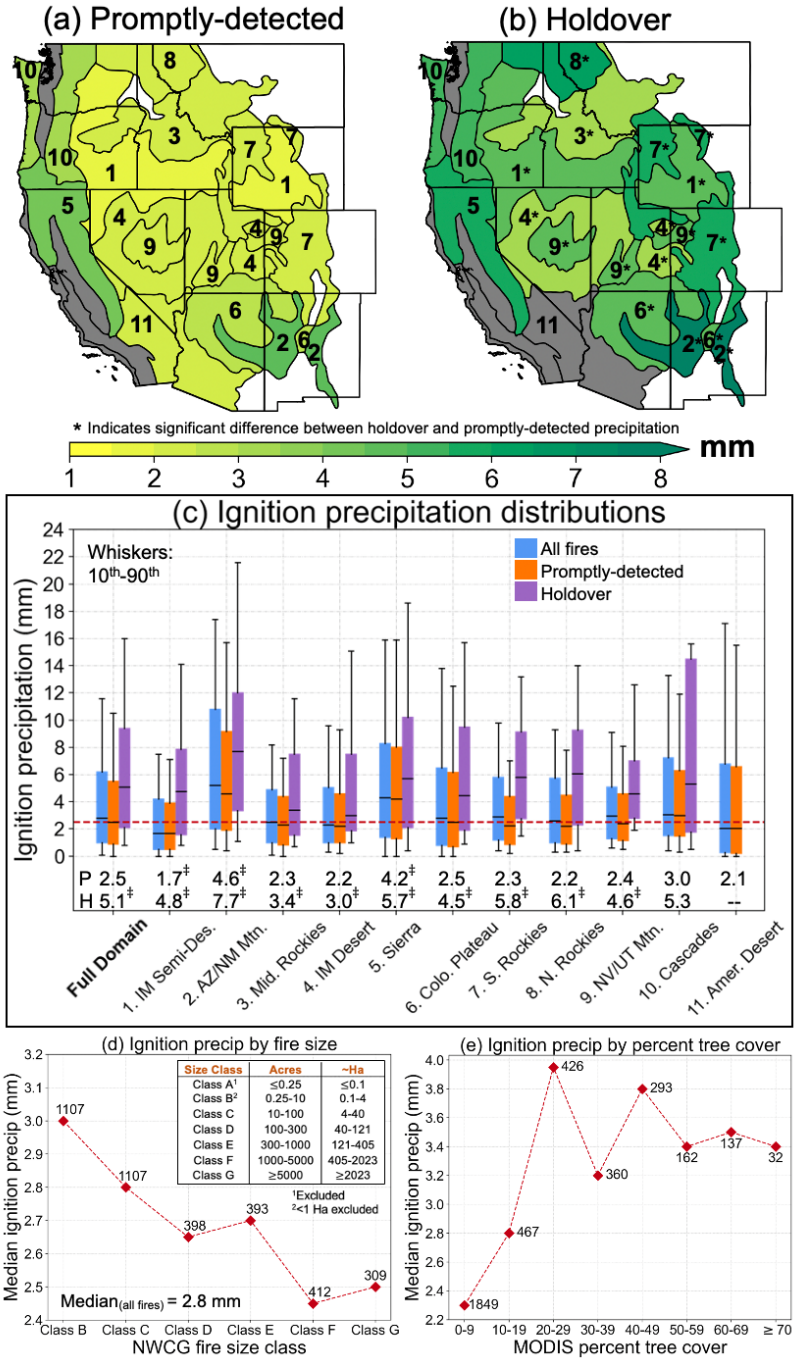

Figure 2. Median ignition precipitation amounts in each ecoprovince for (a) promptly-detected and (b) holdover LIWs. Asterisks beside ecoprovince ranks indicate statistically significant differences ($P < 0.10$) between the promptly-detected and holdover precipitation distributions based on the Mann-Whitney *U* test. (c) Distributions of ignition precipitation amounts for all (blue), promptly-detected (orange) and holdover (purple) LIWs. Red dashed line in (c) indicates 2.5mm daily precipitation threshold commonly used for "dry"

lightning. Numbers below distributions are median ignition precipitation amounts (mm) for promptly-detected ("P") and holdover ("H") LIWs. Markers (‡) indicate that precipitation amounts are significantly different ($P < 0.10$) from 2.5mm based on bootstrap resampling ($n = 1000$ iterations). Median ignition precipitation for all WUS LIWs binned by (d) NWCG fire size class and (e) MODIS percent tree cover. Text accompanying datapoints shows number of LIWs in each bin. Note that the American Desert ecoprovince (#11) is excluded for holdovers in (b-c) and from statistical testing due to low sample size.

Across all WUS LIWs, the median ignition precipitation is 2.8mm. However, this number varies for NWCG fire size classes (Figure 2d, S2). Smaller fires (<40ha; Class B and C) comprise the majority of LIWs and are associated with higher ignition precipitation (2.8-3.0mm) whereas the largest LIWs (≥405ha; Class F and G) occur with lower ignition precipitation (~2.5mm), likely reflecting increased flammability due to less precipitation. Ignition precipitation amounts are also sensitive to percent tree cover (Figure 2e). LIWs ignite with higher accompanying precipitation (>3.2mm) in areas with >20% tree cover compared to areas with <10% tree cover (~2.3mm). These results indicate an increased risk of LIWs in forested areas at precipitation amounts that may be too "wet" for ignition in non-forest environments, where canopy interception of rainfall is absent (Wotton et al., 2005).

Our results suggest that the <2.5mm precipitation amount commonly used to identify dry lightning is not adequate for capturing LIW ignition risk across most of the WUS, particularly for holdovers and LIWs in forested areas that can sustain ignition despite more accompanying rainfall. Approximately 72% of all WUS holdovers occurred with ≥2.5mm precipitation (Figure S3). Further, median holdover ignition precipitation amounts are significantly higher than 2.5mm everywhere except the Cascades, while promptly-detected precipitation amounts are close to 2.5mm in most ecoprovinces (Figure 2c). For predicting and modeling LIW ignitions, these results imply that different precipitation amounts need to be considered to account for predominant vegetation type and holdovers, which comprise ~15% of WUS LIWs (Figure 1b).

Our findings of higher holdover precipitation amounts are robust across IMERG and gridMET (Figures S4-S5). However, the radar-based MRMS shows systematically higher median precipitation for all ecoprovinces compared to the satellite-based IMERG or the gauge-interpolated gridMET (Figure 3). Aggregated across all WUS LIWs, the median ignition precipitation is 1.4mm using IMERG and 1.2mm using gridMET, compared to 2.8mm using MRMS. Such uncertainties in ignition precipitation could arise from multiple factors

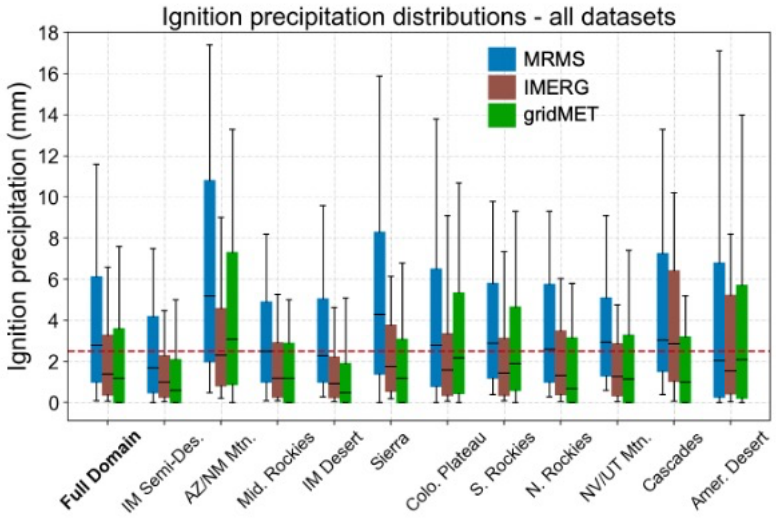

Figure 3. Distributions of ignition precipitation amounts for all LIWs in the domain and across ecoprovinces using MRMS (blue), IMERG (brown), and gridMET (green). Red dashed line indicates commonly used 2.5mm daily precipitation threshold for "dry" lightning. Whiskers indicate 10th-90th percentiles.

including varying gauge density and radar coverage, instrumentation, measurement methods, and the influence of terrain and local meteorology. We note that MRMS might overestimate ignition precipitation amounts as radar beams cannot resolve virga (Zhang et al., 2016). Nonetheless, the finer spatial resolution and ground-based radar coverage of MRMS offers an advantage when capturing isolated convective episodes that can produce LIWs (Flannigan & Wotton, 1991;

Pineda & Rigo, 2017), which may not be captured by the station network that gridMET is weighted toward or biased low due to averaging over the coarser grid of IMERG.

3.3 Environmental conditions associated with lightning-ignited wildfires

To understand the influence of environmental conditions on promptly-detected and holdover LIWs, we compare atmospheric and fuel moisture conditions on identified lightning days for each LIW (Figure 4, S6). Vapor pressure deficit (VPD; -9.3 to -3.8hPa) and maximum temperatures (T_{max}; -5.6 to -2.0°C) are significantly lower for holdover compared to promptly-detected LIWs across all ecoprovinces (Figure 4a-d), and 100-hour fuel moisture (FM_{100}; +0.4 to +2.6%) is significantly higher (Figure 4e-f). Meanwhile, 1000-hour fuel moisture (FM_{1000}; +0.2 to +2.5%) is higher across all ecoprovinces and these differences are significant in all but the Intermountain Semi-Desert (#1) and Intermountain Desert (#4) (Figure 4g-h). The relatively cooler and more humid conditions associated with holdovers, along with higher fuel moisture, are consistent with previous work (Pineda et al., 2022).

The significantly higher FM_{100} in all ecoprovinces during holdovers (Figure 4e-f) indicates the importance of fuel moisture in medium-size (~3-8cm) dead fuels on whether a LIW smolders or quickly spreads. These ecoprovinces are predominantly either coniferous forest or shrub steppe and have abundant fuels of this size (Figure 1c). Similarly, most ecoprovinces contain abundant large fuels (~8-20cm) and have significant differences in FM_{1000} between holdover and promptly-detected LIWs (Figure 4g-h). These differences are larger in the typically drier ecoprovinces in the southeastern parts of the domain including the Arizona/New Mexico Mountains (#2; +2.0%) and the Colorado Plateau (#6; +2.5%; Figure 4g). This indicates that substantially wetter large fuels are needed in these regions for holdovers. Notably for the

Colorado Plateau, substantially more precipitation is observed in the seven days preceding holdovers compared to promptly-detected LIWs (+5.5mm; Figure S7).

In contrast, in the Intermountain Semi-Desert (#1) and Intermountain Desert (#4), FM_{1000} is not significantly higher for holdovers (Figure 4g). This is because large woody debris is scarce in these environments compared to forests, which likely diminishes their importance for LIW ignition and survival. Additionally, longer-term antecedent conditions (i.e., FM_{1000}) may be less important compared to short-term atmospheric conditions for differentiating between promptly-detected and holdover LIWs here. VPD and T_{max} are significantly lower for holdovers in these ecoprovinces (Figure 4a,c) and these differences can strongly influence moisture content of fine fuels common in these semi-arid to arid ecosystems, including invasive annual grasses such as cheatgrass (Davies and Nafus, 2012; Fusco et al., 2019b).

Our results indicate that the combination of fuel moisture and atmospheric conditions around ignition influence holdover LIW risk across ecoprovinces. Specifically, higher precipitation amounts (Figure 2) and cooler, more humid accompanying conditions with higher fuel moisture (Figure 4) during ignition are more conducive to holdovers. Hotter and drier conditions (e.g., higher VPD and T_{max}) such as those observed with promptly-detected LIWs are more favorable for flaming combustion that leads to faster-spreading fires and quicker detection. Although some fuel dryness is required to sustain ignition, cooler and wetter conditions can reduce the combustion to smoldering until conditions become more favorable thereby increasing the chance of a multi-day holdover.

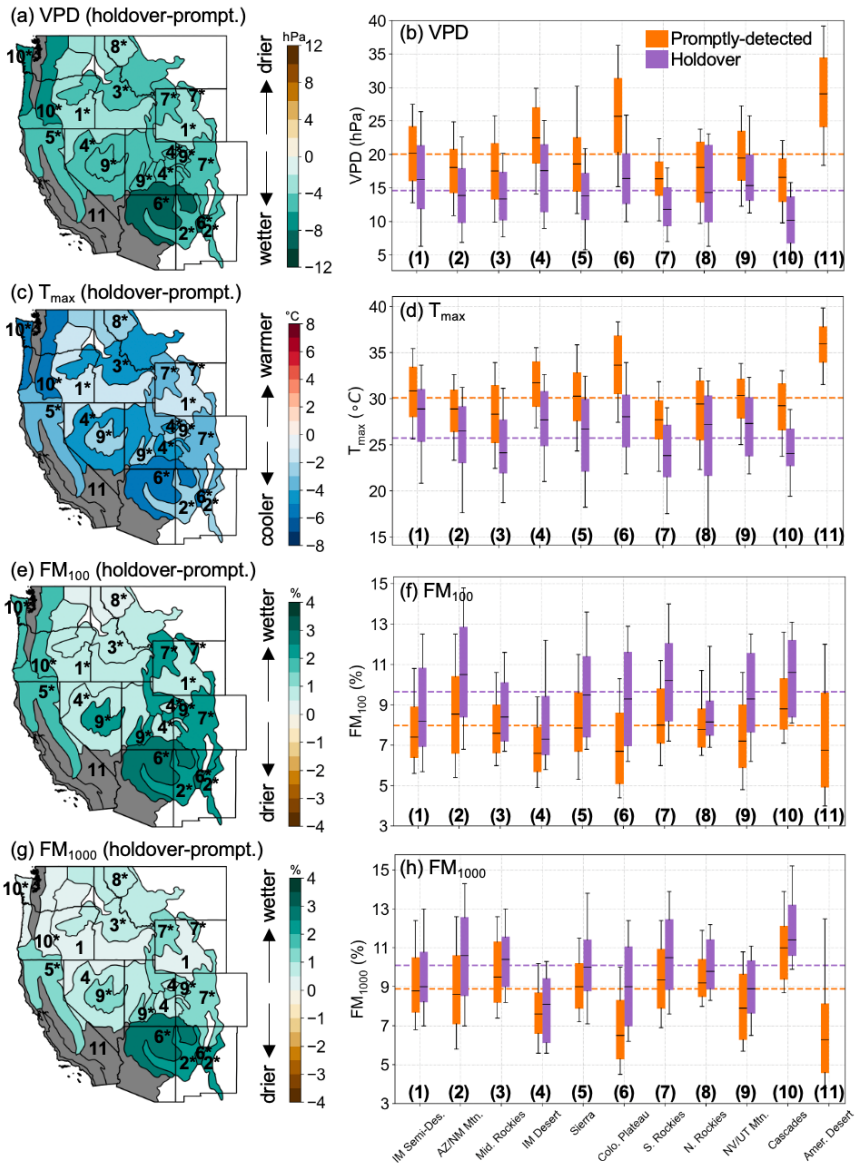

Figure 4. Differences in environmental conditions during holdover and promptly-detected LIWs for (a) VPD, (c) T_{max}, (e) FM_{100}, and (g) FM_{1000}. Asterisks indicate statistically significant difference ($P < 0.10$) between the promptly-detected and holdover distributions based on the Mann-Whitney *U* test. Boxplots of (b) VPD, (d) T_{max}, (f) FM_{100}, and (h) FM_{1000} for promptly-detected (orange) and holdover LIWs (purple). Whiskers indicate 10^{th}-90^{th} percentiles and dashed lines represent WUS-averaged values for promptly-detected (orange) and holdover LIWs (purple). Note that the American Desert ecoprovince (#11) is excluded for holdovers and from statistical testing due to low sample size.

4 Summary and Conclusions

We combined wildfire, lightning, and precipitation data along with atmospheric and fuel moisture indices to provide the first comprehensive multi-year assessment of ignition precipitation amounts and environmental conditions associated with promptly-detected and holdover LIWs across the WUS. Of the 3726 LIWs examined, ~85% were promptly-detected. Holdovers are relatively rare (<10% of all LIWs) in desert and semi-desert ecoprovinces of the Great Basin and southwest US but are more common (>20%) in forested landscapes (Figure 1b). Holdovers occur with significantly higher median precipitation (5.1mm) compared to promptly-detected LIWs (2.5mm). Further, there is substantial spatial heterogeneity in promptly-detected (1.7-4.6mm) and holdover (3.0-7.7mm) ignition precipitation across ecoprovinces (Figure 2).

Holdovers are accompanied by lower T_{max}, lower VPD, and higher FM_{100} and FM_{1000} compared to promptly-detected LIWs in a majority of ecoprovinces (Figure 4). We note, however, that daily-averaged values do not capture exact conditions during the hour of ignition, and hourly meteorological data at the spatial resolution used here are not available. Previous work shows that LIWs rarely become a holdover if ignition occurs during the morning-afternoon burning window, when fine fuels are primed for combustion (Pineda & Rigo, 2017). In addition to more precipitation, cooler and more humid environmental conditions along with late afternoon-evening ignition likely increase holdover probability. As holdovers represent ~15% of all LIWs, accounting for their differing ignition precipitation and environmental conditions could advance prediction and identification of LIWs, and provide fire managers with information to retain resources after lightning events if conditions for holdovers are present.

Overall, our findings indicate that the widely-used 2.5mm precipitation amount is only useful when characterizing LIWs in limited regions and a subset of scenarios. Ignition

precipitation amounts are affected by climate and vegetation characteristics including tree cover, and differ by fire size. We suggest that spatially varying, vegetation-specific precipitation thresholds would more accurately characterize the risk of LIW ignition and holdover potential in different ecoprovinces of the WUS. Our results can inform prediction, modeling, and future projections of LIWs across this region to aid the suppression, management, and adaptation to these fires in a changing climate with increasing wildfire risk.

Acknowledgments

We thank the National Interagency Fire Center for compiling the wildfire database and Vaisala, Inc. for collecting the NLDN lightning data used in this study. This research used resources from the Center for Institutional Research Computing at Washington State University. This work was supported by NASA awards 80NSSC21K1603 (DAK and DS) and 80NSSC21K1501 (PCL), and by NSF award OAI-2019762 (JTA).

Data Availability Statement

MRMS data are from NOAA's National Severe Storms Laboratory, sourced from Iowa State University's Environmental Mesonet archive (https://mtarchive.geol.iastate.edu/). IMERG data were acquired from NASA's Goddard Earth Sciences Data Information Services Center (GES DISC; https://disc.gsfc.nasa.gov/datasets/GPM_3IMERGDF_06/summary?keywords=imerg). MODIS land cover data (250m) is from the 2010 North American Environmental Atlas, made available by the Commission for Environmental Cooperation (http://www.cec.org/north-american-environmental-atlas/land-cover-2010-modis-250m/). Percent tree cover (as of 2020; 250m) is from the MODIS Vegetation Continuous Fields dataset (MOD44B) sourced from the USGS Land Processes Distributed Active Archive Center

(https://lpdaacsvc.cr.usgs.gov/appeears/). Ecoprovince polygons are sourced from the US Geological Survey (https://www.sciencebase.gov/catalog/item/54244abde4b037b608f9e23d). The NLDN lightning data are not publicly available at the resolution used herein, but can be purchased directly from Vaisala, Inc. (https://www.vaisala.com/en/products/national-lightning-detection-network-nldn) or Earth Networks (https://www.earthnetworks.com/product/lightning-data/). Datasets used to perform the analyses are available at the following Zenodo repository: https://doi.org/10.5281/zenodo.7761326 (Kalashnikov, 2023a). Source code to create publication figures can be accessed at the following GitHub repository: https://github.com/dmitri1357/Lightning-fire-precipitation (Kalashnikov, 2023b). Geospatial analyses were performed using the Python packages *GeoPy*, *GeoPandas*, and *rasterio*.

References

Abatzoglou, J. T. (2013). Development of gridded surface meteorological data for ecological applications and modelling. *International Journal of Climatology*, *33*(1), 121-131. https://doi.org/10.1002/joc.3413

Abatzoglou, J. T., Kolden, C. A., Balch, J. K., & Bradley, B. A. (2016). Controls on interannual variability in lightning-caused fire activity in the western US. *Environmental Research Letters*, *11*(4), 045005. https://doi.org/10.1088/1748-9326/11/4/045005

Balch, J. K., Bradley, B. A., Abatzoglou, J. T., Nagy, R. C., Fusco, E. J., & Mahood, A. L. (2017). Human-started wildfires expand the fire niche across the United States. *Proceedings of the National Academy of Sciences of the United States of America*, *114*(11), 2946–2951. https://doi.org/10.1073/pnas.1617394114

Barros, A. M. G., Day, M. A., Preisler, H. K., Abatzoglou, J. T., Krawchuk, M. A., Houtman, R.,

& Ager, A. A. (2021). Contrasting the role of human- and lightning-caused wildfires on future fire regimes on a Central Oregon landscape. *Environmental Research Letters*, *16*(6), 064081. https://doi.org/10.1088/1748-9326/ac03da

Brey, S. J., Barnes, E. A., Pierce, J. R., Wiedinmyer, C., & Fischer, E. V. (2018). Environmental Conditions, Ignition Type, and Air Quality Impacts of Wildfires in the Southeastern and Western United States. *Earth's Future*, *6*(10), 1442–1456. http://doi.org/10.1029/2018EF000972

Brey, S. J., Barnes, E. A., Pierce, J. R., Swann, A. L. S., & Fischer, E. V. (2020). Past Variance and Future Projections of the Environmental Conditions Driving Western U.S. Summertime Wildfire Burn Area. *Earth's Future*, *9*(2), e2020EF001645. http://doi.org/10.1029/2020EF001645

Burrows, W. R., Price, C., & Wilson, L. J. (2005). Warm Season Lightning Probability Prediction for Canada and the Northern United States. *Weather and Forecasting*, *20*(6), 971-988. https://doi.org/10.1175/waf895.1

Cattau, M. E., Wessman, C., Mahood, A., & Balch, J. K. (2020). Anthropogenic and lightning-started fires are becoming larger and more frequent over a longer season length in the U.S.A. *Global Ecology and Biogeography*, *29*(4), 668-681. https://doi.org/10.1111/geb.13058

Davies, K. W., & Nafus, A. M. (2012). Exotic annual grass invasion alters fuel amounts, continuity and moisture content. *International Journal of Wildland Fire*, *22*(3), 353–358. https://doi.org/10.1071/WF11161

Dowdy, A. J. (2020). Climatology of thunderstorms, convective rainfall and dry lightning environments in Australia. *Climate Dynamics*, *54*, 3041-3052.

https://doi.org/10.1007/s00382-020-05167-9

Dowdy, A. J., & Mills, G. A. (2012). Atmospheric and Fuel Moisture Characteristics Associated with Lightning-Attributed Fires. *Journal of Applied Meteorology and Climatology*, *51*(11), 2025-2037. https://doi.org/10.1175/jamc-d-11-0219.1

Fischer, D. G., Vieira, S. T., & Jayakaran, A. D. (2023). Distinct Rainfall Interception Profiles among Four Common Pacific Northwest Tree Species. *Forests*, *14*(1), 144. https://doi.org/10.3390/f14010144

Flannigan, M. D., & Wotton, B. M. (1991). Lightning-ignited forest fires in northwestern Ontario. *Canadian Journal of Forest Research*, *21*(3), 277-287. https://doi.org/10.1139/x91-035

Fuquay, D. M. (1962). Mountain Thunderstorms and Forest Fires. *Weatherwise*, *15*(4), 149-152. https://doi.org/10.1080/00431672.1962.9926981

Fusco, E. J., Finn, J. T., Abatzoglou, J. T., Balch, J. K., Dadashi, S., & Bradley, B. A. (2019a). Detection rates and biases of fire observations from MODIS and agency reports in the conterminous United States. *Remote Sensing of Environment*, *220*, 30-40. https://doi.org/10.1016/j.rse.2018.10.028

Fusco, E. J., Finn, J. T., Balch, J. K., Nagy, R. C., & Bradley, B. A. (2019b). Invasive grasses increase fire occurrence and frequency across US ecoregions. *Proceedings of the National Academy of Sciences of the United States of America*, *116*(47), 23594–23599. https://doi.org/10.1073/pnas.1908253116

Gorman, S. (2021, July 22). Lightning found to have ignited Oregon's mammoth Bootleg fire. *Reuters*. Retrieved from https://www.reuters.com/world/us/lightning-found-have-ignited-oregons-mammoth-bootleg-fire-2021-07-22/

Hall, B. L. (2007). Precipitation associated with lightning-ignited wildfires in Arizona and New Mexico. *International Journal of Wildland Fire*, *16*(2), 242-254. https://doi.org/10.1071/wf06075

Kalashnikov, D. A. (2023a). Data for Western U.S. Lightning-Fire-Precipitation paper (Version 1) [Dataset]. Zenodo. https://doi.org/10.5281/zenodo.8019079

Kalashnikov, D. A. (2023b). dmitri1357/Lightning-fire-precipitation [Software]. GitHub. Available at: https://github.com/dmitri1357/Lightning-fire-precipitation

Kalashnikov, D. A., Loikith, P. C., Catalano, A. J., Waliser, D. E., Lee, H., & Abatzoglou, J. T. (2020). A 30-Yr Climatology of Meteorological Conditions Associated with Lightning Days in the Interior Western United States. *Journal of Climate*, *33*(9), 3771-3785. https://doi.org/10.1175/jcli-d-19-0564.1

Kalashnikov, D. A., Abatzoglou, J. T., Nauslar, N. J., Swain, D. L., Touma, D., & Singh, D. (2022a). Meteorological and geographical factors associated with dry lightning in central and northern California. *Environmental Research: Climate*, *1*(2), 025001. https://doi.org/10.1088/2752-5295/ac84a0

Kalashnikov, D. A., Schnell, J. L., Abatzoglou, J. T., Swain, D. L., & Singh, D. (2022b). Increasing co-occurrence of fine particulate matter and ground-level ozone extremes in the western United States. *Science Advances*, *8*(1), eabi9386. https://doi.org/10.1126/sciadv.abi9386

Keeley, J. E., & Syphard, A. D. (2021). Large California wildfires: 2020 fires in historical context. *Fire Ecology*, *17*(22), 1-11. https://doi.org/10.1186/s42408-021-00110-7

Krumm, W. R. (1954). On the Cause of Downdrafts from Dry Thunderstorms over the Plateau Area of the United States. *Bulletin of the American Meteorological Society*, *35*(3), 122-125.

https://doi.org/10.1175/1520-0477-35.3.122

Larjavaara, M., Pennanen, J., & Tuomi, T. J. (2005). Lightning that ignites forest fires in Finland. *Agricultural and Forest Meteorology*, *132*(3-4), 171-180. https://doi.org/10.1016/j.agrformet.2005.07.005

Littell, J. S., McKenzie, D., Peterson, D. L., & Westerling, A. L. (2009). Climate and wildfire area burned in western U.S. ecoprovinces, 1916-2003. *Ecological Applications: A Publication of the Ecological Society of America*, *19*(4), 1003–1021. https://doi.org/10.1890/07-1183.1

Li, Y., Mickley, L. J., Liu, P., & Kaplan, J. O. (2020). Trends and spatial shifts in lightning fires and smoke concentrations in response to 21st century climate over the national forests and parks of the western United States. *Atmospheric Chemistry and Physics*, *20*(14), 8827-8838. https://doi.org/10.5194/acp-20-8827-2020

MacNamara, B. R., Schultz, C. J., & Fuelberg, H. E. (2020). Flash Characteristics and Precipitation Metrics of Western U.S. Lightning-Initiated Wildfires from 2017. *Fire*, *3*(1), 5. https://doi.org/10.3390/fire3010005

Moris, J. V., Conedera, M., Nisi, L., Bernardi, M., Cesti, G., & Pezzatti, G. B. (2020). Lightning-caused fires in the Alps: Identifying the igniting strokes. *Agricultural and Forest Meteorology*, *290*, 107990. https://doi.org/10.1016/j.agrformet.2020.107990

Nag, A. (2014). Recent Evolution of the U.S. National Lightning Detection Network. Paper presented at *Proceedings of the 23rd International Lightning Detection Conference*, Tucson, AZ, USA, 18-19 March 2014.

Nauslar, N., Kaplan, M., Wallmann, J., & Brown, T. (2013). A forecast procedure for dry thunderstorms. *Journal of Operational Meteorology*, *1*, 200-214.

https://doi.org/10.15191/nwajom.2013.0117

Nauslar, N. J. (2014). Examining the Lightning Polarity of Lightning Caused Wildfires. Paper presented at *Proceedings of the 23rd International Lightning Detection Conference*, Tucson, AZ, USA, 18-19 March 2014.

Pérez-Invernón, F. J., Huntrieser, H., & Moris, J. V. (2022). Meteorological Conditions Associated with Lightning Ignited Fires and Long-Continuing-Current Lightning in Arizona, New Mexico and Florida. *Fire*, *5*(4), 96. https://doi.org/10.3390/fire5040096

Pineda, N., Altube, P., Alcasena, F. J., Casellas, E., San Segundo, H., & Montanyà, J. (2022). Characterising the holdover phase of lightning-ignited wildfires in Catalonia. *Agricultural and Forest Meteorology*, *324*, 109111. https://doi.org/10.1016/j.agrformet.2022.109111

Pineda, N., & Rigo, T. (2017). The rainfall factor in lightning-ignited wildfires in Catalonia. *Agricultural and Forest Meteorology*, *239*, 249-263. https://doi.org/10.1016/j.agrformet.2017.03.016

Rorig, M. L., & Ferguson, S. A. (1999). Characteristics of Lightning and Wildland Fire Ignition in the Pacific Northwest. *Journal of Applied Meteorology*, *38*(11), 1565-1575. https://doi.org/10.1175/1520-0450(1999)038<1565:colawf>2.0.co;2

Schultz, C. J., Nauslar, N. J., Wachter, J. B., Hain, C. R., & Bell, J. R. (2019). Spatial, Temporal, and Electrical Characteristics of Lightning in Reported Lightning-Initiated Wildfire Events. *Fire*, *2*(2), 18. https://doi.org/10.3390/fire2020018

Short, K. C. (2014). A spatial database of wildfires in the United States, 1992-2011. *Earth System Science Data*, *6*(1), 1-27. https://doi.org/10.5194/essd-6-1-2014

Storm Prediction Center (SPC) Dry Thunderstorm Guidance Webpage. (2022). Retrieved December 20, 2022, from https://www.spc.noaa.gov/exper/dryt/

United States Forest Service. (1995). Description of the Ecoregions of the United States. 108 pp.

Vant-Hull, B., Thompson, T., & Koshak, W. (2018). Optimizing Precipitation Thresholds for Best Correlation Between Dry Lightning and Wildfires. *Journal of Geophysical Research: Atmospheres*, *123*(5), 2628-2639. https://doi.org/10.1002/2017jd027639

Wallmann, J., Milne, R., Smallcomb, C., & Mehle, M. (2010). Using the 21 June 2008 California Lightning Outbreak to Improve Dry Lightning Forecast Procedures. *Weather and Forecasting*, *25*(5), 1447-1462. https://doi.org/10.1175/2010WAF2222393.1

Wildland Fire Interagency Geospatial Services (WFIGS) - Wildland Fire Locations Full History. (2022). Retrieved July 23, 2022, from https://data-nifc.opendata.arcgis.com/datasets/nifc::wfigs-wildland-fire-locations-full-history/about

Wotton, B. M., Stocks, B. J., & Martell, D. L. (2005). An index for tracking sheltered forest floor moisture within the Canadian Forest Fire Weather Index System. *International Journal of Wildland Fire*, *14*(2), 169-182. https://doi.org/10.1071/WF04038

Zhang, J., Howard, K., Langston, C., Kaney, B., Qi, Y., Tang, L., et al. (2016). Multi-Radar Multi-Sensor (MRMS) Quantitative Precipitation Estimation: Initial Operating Capabilities. *Bulletin of the American Meteorological Society*, *97*(4), 621-638. https://doi.org/10.1175/BAMS-D-14-00174.1

Zhou, X., Josey, K., Kamareddine, L., Caine, M. C., Liu, T., Mickley, L. J., et al. (2021). Excess of COVID-19 cases and deaths due to fine particulate matter exposure during the 2020 wildfires in the United States. *Science Advances*, *7*(33), eabi8789. https://doi.org/10.1126/sciadv.abi8789

CHAPTER FIVE: PREDICTING CLOUD-TO-GROUND LIGHTNING IN THE WESTERN UNITED STATES FROM THE LARGE-SCALE ENVIRONMENT USING EXPLAINABLE NEURAL NETWORKS

Written for submission to *Journal of Geophysical Research: Atmospheres* and reproduced here in its original format.

Attributions:

Dmitri A. Kalashnikov designed the research, performed all analyses, and wrote the manuscript. D. Singh provided supervision and research direction, and helped edit the manuscript. F.V. Davenport and Z.M. Labe provided methodological guidance, feedback on the research, and manuscript edits. P.C. Loikith and J.T. Abatzoglou provided feedback on the research and helped edit the manuscript.

Abstract

Lightning is a major source of wildfire ignition in the western United States (WUS). We build and train Convolutional Neural Networks (CNNs) to predict the occurrence of cloud-to-ground lightning across the WUS during June-September from the spatial patterns of seven large-scale meteorological variables from reanalysis (1995-2022). Individually-trained CNN models at each 1° x 1° grid cell (n = 285 CNNs) show high skill at predicting lightning days across the WUS and perform best in parts of the interior Southwest where summertime lightning is most common. Further, interannual correlation between observed and predicted lightning days is high (median r = 0.87), demonstrating that locally-trained CNNs realistically capture year-to-year variation in lightning activity across the WUS. We then use an "eXplainable Artificial Intelligence" (XAI) technique called Layer-wise Relevance Propagation (LRP) to investigate the relevance of predictor variables to successful lightning prediction in each grid cell. Using maximum LRP values, our results show that two thermodynamic variables - ratio of surface moist static energy to free-tropospheric saturation moist static energy, and the 700-500 hPa lapse rate - are the most relevant lightning predictors for 96% of CNNs. As lightning is not directly simulated by global climate models, these CNNs could be used to parameterize lightning in climate models to assess changes in future lightning occurrence with projected climate change. Understanding changes in lightning risk and consequently lightning-caused wildfire risk across the WUS could inform fire management, planning, and disaster preparedness.

Plain Language Summary

Lightning is a major source of wildfire ignition in the western U.S. We use a machine learning technique called "Convolutional Neural Networks," or CNNs, to predict the occurrence of cloud-to-ground lightning across the western U.S. Our CNN models use seven meteorological variables

that are known to be important for lightning activity and are trained over the summer season (June-September) during 1995-2022. CNN models are trained at each individual latitude by longitude grid box and show high skill at predicting lightning days across the western U.S., especially in parts of the interior Southwest where summertime lightning is most common. Further, we show that CNNs realistically predict year-to-year variation of lightning across the region. We then use "eXplainable Artificial Intelligence" (XAI) to determine the relevance of each of the seven meteorological variables to successful lightning predictions at each grid cell. Our results show that two variables, describing aspects of atmospheric moisture and vertical instability, are most relevant for successful lightning predictions by the CNNs. Since lightning is not directly simulated by global climate models, the CNNs can be applied to climate model output to quantify future changes in lightning occurrence, and lightning-caused wildfire risk across the western U.S.

1. Introduction

In the western United States (WUS), summertime cloud-to-ground lightning is an important wildfire ignition source when occurring with limited precipitation ("dry lightning"). Although humans are responsible for most wildfire ignitions, lightning-caused fires account for the majority of burned area across this region (Abatzoglou et al., 2016; Balch et al., 2017; Brey et al., 2018; Janssen et al., 2023; Kalashnikov, Abatzoglou, et al., 2022; Komarek, 1967). Smoke from such fires can also have far-reaching air quality and human health impacts. For example, in August 2020, smoke from wildfires ignited by a widespread dry lightning outbreak in California resulted in extreme levels of air pollution across more than two-thirds of the WUS (Kalashnikov, Schnell, et al., 2022) and contributed to high human mortality and morbidity in multiple states

(Rosenthal et al., 2022; Zhou et al., 2021). Projected warming in the WUS is likely to increase burned area from wildfires – including those ignited by lightning – due to drier fuels (Barros et al., 2021; Li et al., 2020; Pérez-Invernón et al., 2023). Recent studies have also projected increases in lightning occurrence in the WUS (Finney et al., 2018; Janssen et al., 2023; Pérez-Invernón et al., 2023), lending urgency to understanding and anticipating societal impacts with continued warming.

Complicating future projection efforts is the fact that lightning cannot be directly simulated at the typically coarse spatial resolutions of Global Climate Models (GCMs) because of the inability to simulate the fine-scale physical processes associated with lightning activity. Previous studies of lightning using atmospheric reanalyses and GCMs have relied on convective parameterizations utilizing cloud top height (Janssen et al., 2023; Krause et al., 2014; Pérez-Invernón et al., 2023; Price & Rind, 1992), cloud droplet concentration (Michalon et al., 1999), cold cloud depth (Yoshida et al., 2009), convective ice flux (Finney et al., 2014; Finney et al., 2018; Janssen et al., 2023), cloud ice fraction (Han et al., 2021), convective precipitation and mass flux (Allen & Pickering, 2002; Magi, 2015), the product of convective available potential energy and precipitation rate (Chen et al., 2021; Romps et al., 2014), and other combinations of variables that are physically relevant for in-cloud charge separation and lightning production. (See Clark et al. [2017] and Etten-Bohm et al. [2021] for a comprehensive summary of lightning parameterizations). However, substantial disagreement in lightning projections can arise when using different parameterizations, and the best approach is not yet clear (Clark et al., 2017; Romps, 2019; Tost et al., 2007). Further, there are inherent uncertainties in representing convective cloud properties in GCMs (Etten-Bohm et al., 2021).

Due to these limitations, recent studies have developed relatively simple lightning parameterizations using large-scale dynamic and thermodynamic meteorological variables, which are directly simulated by GCMs. For example, Etten-Bohm et al. (2021) used logistic regression to predict lightning occurrence in the global tropics and subtropics from a set of dynamic and thermodynamic variables in reanalysis, with the intention of applying this statistical parameterization to GCMs. Similarly, Liu et al. (2022) used Random Forest models trained on a set of four meteorological variables to predict the global occurrence of thunderstorms. Bates et al. (2018) tested six statistical modeling approaches for predicting lightning days in Australia using a comprehensive set of 31 large-scale meteorological variables and found that logistic regression performed best. Other studies have used multiple linear regression to predict lightning flash density from meteorological variables that broadly describe the convective state of the atmosphere (Stolz et al., 2017; Veraverbeke et al., 2017). Notably, neural networks have been underutilized in lightning parameterization efforts in reanalyses and GCMs, with limited examples trained over relative short time periods (e.g., Cheng et al., 2024).

We aim to make lightning predictions using multivariate Convolutional Neural Networks (CNNs) trained on large-scale meteorological variables over a 28-year historical period (1995-2022) and evaluate whether CNNs offer advantages over a traditional statistical classifier. CNNs are a type of supervised deep learning image classification (Goodfellow et al., 2016; LeCun et al., 2015), and have shown promising potential in atmospheric and climate science at capturing complex and nonlinear physical relationships (Baño-Medina et al., 2021; Chattopadhyay et al., 2020; Dagon et al., 2022; Davenport & Diffenbaugh, 2021; Lagerquist et al., 2019; Molina et al., 2021; Trok et al., 2023). Another strength of CNNs is their inherent ability to differentiate spatial features as the input fields are two-dimensional, which can facilitate robust learning of important

atmospheric features for a given prediction task (Baño-Medina et al., 2021; Molina et al., 2021). Importantly, "eXplainable Artificial Intelligence" (XAI), a term encompassing the growing ecosystem of machine learning visualization methods, can disentangle the contribution of different variables and their spatial features to predictions, thus enabling physical insights into the governing processes (Davenport & Diffenbaugh, 2021; Ebert-Uphoff & Hilburn, 2020; Labe & Barnes, 2021; Mamalakis, Barnes, et al., 2022; Mamalakis, Ebert-Uphoff, et al., 2022; Mamalakis et al., 2023; McGovern et al., 2019; Molnar et al., 2022; Rudin, 2019; Toms et al., 2020). Here, we use an XAI technique known as Layer-wise Relevance Propagation (LRP; Bach et al., 2015) to investigate the relative importance of predictor variables and their spatial patterns to successful lightning prediction across the WUS.

In this study, we develop, train, and test individual CNNs to predict the daily occurrence of cloud-to-ground lightning at each 1° x 1° grid cell in the WUS (for a total of 285 CNNs) based on the spatial fields of seven large-scale meteorological variables. WUS thunderstorms are relatively rare and understudied compared to severe thunderstorms that commonly affect the central and eastern U.S, and there is a lack of lightning parameterizations developed specifically for this region. One exception is the recent work by Cheng et al. (2024), who used non-convolutional neural networks to predict lightning flash density in the WUS. However, their reported correlation with observations was relatively low (0.57), and CNNs trained at individual grid cells using locally-centered meteorological fields could improve predictions. By developing individual CNNs at each grid cell and predicting cloud-to-ground lightning at the daily scale, our approach offers two primary advantages over traditional lightning parameterization methods. *First*, our targeted approach provides refined spatial and temporal resolution compared to parameterization methods that assessed bulk lightning activity at national to global scales and at

monthly to annual aggregation (Allen & Pickering, 2002; Cheng et al., 2024; Clark et al., 2017; Finney et al., 2016; Finney et al., 2018; Magi, 2015; Price & Rind, 1992; Romps, 2019; Romps et al., 2014). Our development of predictor models at each grid cell is better suited for the WUS, since lightning climatology and associated meteorological patterns can vary considerably over short distances due to spatial heterogeneity of the terrain (Kalashnikov et al., 2020). *Second*, with few exceptions (e.g., Allen & Pickering, 2002), most previous studies have parameterized total lightning flash rate (including intra-cloud and cloud-to-ground) and occasionally estimated cloud-to-ground lightning in future projections using empirically-derived ratios (Krause et al., 2014; Pérez-Invernón et al., 2023; Price & Rind, 1994). To reduce uncertainty, we train CNNs to explicitly predict cloud-to-ground lightning as only this type of lightning poses the risk of wildfire ignition.

2. Data and Methods

2.1. Datasets

Daily gridded cloud-to-ground lightning flash totals (0.1° x 0.1°; 1995-2022) are from the National Lightning Detection Network (NLDN). Daily meteorological data are obtained or derived from the National Aeronautics and Space Administration's (NASA) Modern-Era Retrospective Analysis for Research and Applications, Version 2 (MERRA-2; Gelaro et al., 2017) that has a spatial resolution of 0.5° latitude x 0.625° longitude. All datasets are upscaled to 1° x 1° spatial resolution to create a larger sample size of lightning days in each grid cell to train the CNNs, while still capturing sub-regional variations in lightning activity. This resolution is additionally comparable to GCMs that are mostly output on 1° x 1° or coarser grids. A day in each 1° x 1° grid cell is characterized as a lightning day if any of the constituent 0.1° x 0.1°

NLDN grid cells experience cloud-to-ground lightning. MERRA-2 data are bilinearly interpolated and matched temporally and spatially with the lightning data at this resolution.

2.2. Study Domain

We construct CNNs to predict the daily occurrence of cloud-to-ground lightning (hereafter, "lightning") in each 1° x 1° grid cell over the conterminous WUS (Figure 1; 32°-49°N and Pacific coast to 104°W) over June-September (hereafter, "warm season"). We exclude grid cells that experience lightning on less than 10% of warm-season days (i.e., lightning fraction of <0.1), corresponding to Pacific coastal areas where lightning-caused wildfire ignitions are rare (Figure 1a-b; Brey et al., 2018; Kalashnikov et al., 2023). The total number of lightning days and corresponding lightning fraction are highest over the interior Southwest, as these areas are directly influenced by convection associated with the North American Monsoon (Adams & Comrie, 1997; Barlow et al., 1998). The most cloud-to-ground lightning days over the study period occurred at a grid cell in northern New Mexico (n = 2499), representing ~73.2% of all warm-season days (Figure 1b).

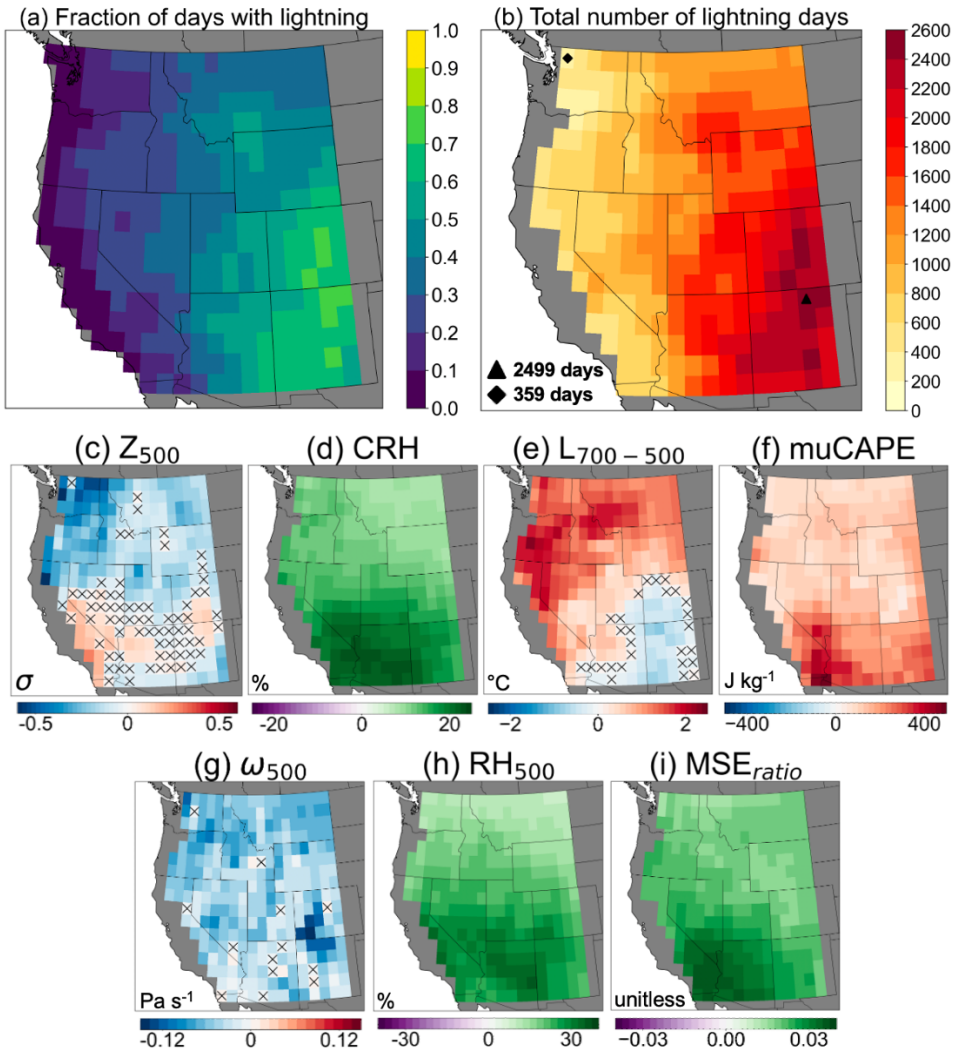

Figure 1. Spatial distribution of lightning and meteorological conditions. (a) Fraction and (b) total number of days with at least one cloud-to-ground lightning flash in 1° x 1° grid cells of the WUS during June-September (1995-2022). Markers and inset text in (b) denote the grid cells with the most and least cumulative lightning days between 1995-2022. (c-i) Differences in meteorological variables (full variable names provided in section 2.3) on lightning days relative to days without lightning. Hatching indicates that differences are insignificant ($P \geq 0.05$) between lightning and non-lightning days according to a two-tailed *t*-test. Areas along the Pacific coast shaded in gray in (b-i) are excluded from further analysis due to low sample size of lightning days (<10% of all days).

2.3. Meteorological Variables

We utilize a set of seven dynamic and thermodynamic variables that influence lightning occurrence, with variable selection informed by literature (Table S1). These variables broadly

describe moisture availability, atmospheric instability, and the large-scale atmospheric circulation which can influence both factors. Atmospheric circulation is captured through deseasonalized, standardized anomalies of 500 hPa geopotential height (Z_{500}), computed from 7-day windows centered on each calendar date in the 28-year record. To characterize atmospheric moisture, we use column-integrated relative humidity (CRH), defined as the ratio of vertically integrated atmospheric water vapor to its saturation counterpart (Mo et al., 2021; Wolding et al., 2020). CRH is analogous to total column water vapor but is a more direct proxy for liquid and ice content, as the amount of water vapor that can condense depends on the degree of saturation (Etten-Bohm et al., 2021; Mo et al., 2021). We also use 500 hPa relative humidity (RH_{500}) to capture "high-based" convection commonly associated with WUS thunderstorms, particularly outside the core monsoon region of the interior Southwest (Kalashnikov, Abatzoglou, et al., 2022; Krumm, 1954; Nauslar et al., 2013; Rorig et al., 2007). In these situations, moisture advection and cloud bases can be above 700 hPa and convection does not depend on the moisture profile below that level, thus limiting the usefulness of total-column quantities. Updraft strength is quantified through omega, or vertical velocity, at 500 hPa (ω_{500}) and the vertical temperature difference, or lapse rate, between the 700 and 500 hPa pressure levels ($L_{700\text{-}500}$). We also evaluated a larger set of variables as potential predictors, including omega and relative humidity at 700 hPa. However, these variables at 500 hPa show larger differences between lightning and non-lightning days across most of the domain (not shown).

We also use two derived variables that combine temperature and moisture into integrated metrics of instability that are indicators of environments favorable for convection - "most unstable" Convective Available Potential Energy (muCAPE) and the ratio of surface moist static energy to the free-troposphere saturation moist static energy (MSE_{ratio}). Our rationale for using

muCAPE over surface-based CAPE is that high-based convection can occur independently of surface-based instability (or lack thereof) in certain environments due to mid-tropospheric moisture and instability overlying a stable boundary layer, and previous studies have found CAPE to be relatively unimportant for lightning prediction over the WUS (Burrows et al., 2005; Liu et al., 2022). Rather than integrating from the surface, muCAPE is integrated vertically from the most unstable parcel in the lowest 300 hPa to the equilibrium level, and is therefore less sensitive to situations when convection initiates above the surface layer (Luong et al., 2017; Rochette et al., 1999). We compute muCAPE using the *MetPy* Python package (version 1.4.0; May et al., 2023). MSE is a thermodynamic quantity that combines temperature and moisture information and is conserved during adiabatic motions. The MSE_{ratio} can be used to diagnose convection, which occurs when the surface air parcel MSE is equal to the free-troposphere saturation MSE (e.g., $MSE_{ratio} = 1$). Our use of MSE_{ratio} is informed by its recent application in studies that sought to define a theoretical upper bound for near-surface temperatures by considering the convective (in)stability of the boundary layer (Noyelle et al., 2023; Zhang & Boos, 2023). More details on the derivation of CRH and MSE_{ratio} can be found in the supporting information.

Our overarching goal with the selection of these seven variables is to ensure that i) they are useful at differentiating lightning from non-lightning conditions across the WUS, and ii) they are "climate-invariant" (Beucler et al., 2024; Molina et al., 2021), meaning their relationship with lightning should be generalizable to a future, warmer climate in GCM projections. This entails using moisture quantities that are relative, rather than absolute, as the latter can be influenced by underlying shifts due to warming. For example, using measures of relative humidity (e.g., CRH and RH_{500}) is preferable to water vapor content and specific humidity. This is because future

saturation specific humidity will increase with temperature through the Clausius-Clapeyron relation, changing the saturation profile for a given amount of atmospheric water vapor and likely affecting the point at which convection is triggered (Beucler et al., 2024). Meanwhile, constant relative humidity is expected with warming (Douville et al., 2022). As proxies for upward vertical motion, $L_{700\text{-}500}$, muCAPE, ω_{500} and MSE_{ratio} should remain physically consistent over time. Finally, use of Z_{500} standardized anomalies preserves gradients in the anomaly fields irrespective of background tropospheric expansion, as future values would be calculated from a baseline period from that climate.

Figure 1c-i shows the differences in the local values of meteorological variables between lightning and non-lightning days at each grid cell (see Figure S1 for composite values on lightning days). We use a two-tailed *t*-test ($P < 0.05$) to test the significance of difference in meteorological variables on days with lightning versus non-lightning days. CRH, muCAPE, RH_{500}, and MSE_{ratio} are uniformly and significantly higher ($P < 0.05$) across the WUS on lightning days compared to non-lightning days, indicating more moisture and energy available for convection. However, magnitudes of these differences vary and are larger in areas to the south that are under the direct influence of the North American Monsoon. ω_{500} is generally more negative on lightning days compared to non-lightning days indicating stronger updrafts in the mid-troposphere (Figure 1g). In contrast, Z_{500} and $L_{700\text{-}500}$ show anomalies of the opposite sign between northern and portions of southern areas (Figure 1c,e). Lightning activity in areas on the North American Monsoon periphery, including the interior Northwest and northern Rocky Mountains, is frequently associated with mid-latitude disturbances which induce significantly lower Z_{500} and steeper $L_{700\text{-}500}$ through cold air advection aloft (Kalashnikov et al., 2020; Werth & Ochoa, 1993). The lack of steepened $L_{700\text{-}500}$ on lightning days in parts of the interior

Southwest is likely due to a seasonally unstable atmosphere that does not require large deviations to initiate convection (Adams & Souza, 2009; Kalashnikov et al., 2020).

2.4. CNN Architecture, Training, and Tuning

We train individual CNNs at each 1° x 1° grid cell (n = 285) to predict lightning occurrence using the seven meteorological variables as inputs (Figure 2). In this work, our CNNs are binary classifiers that automatically learn spatial patterns from the input data and output a probability of lightning (Class 1) or non-lightning (Class 0). Daily fields of each meteorological variable are remapped to equal-area 20 x 20 grids spanning 2000 km on each side (100 km x 100 km resolution), and centered on the grid cell for which the CNN is trained. The 2000 km distance is chosen to roughly approximate a Rossby half-wavelength (Stoll et al., 2023), thereby capturing large-scale circulation features. Although this distance could create unnecessarily large fields for thermodynamic variables, the CNNs will learn to select the most relevant spatial features within this domain during training (Baño-Medina et al., 2021). For each day, the input to each local CNN thus consists of a three-dimensional matrix (20 x 20 x 7; lat x lon x input variables) (Figure 2a). To increase stability and robustness during training, all input variables are rescaled by their maximum value across the full domain and time period. Training labels provided to the CNNs are the presence/absence of lightning from the NLDN in that 1° x 1° grid cell.

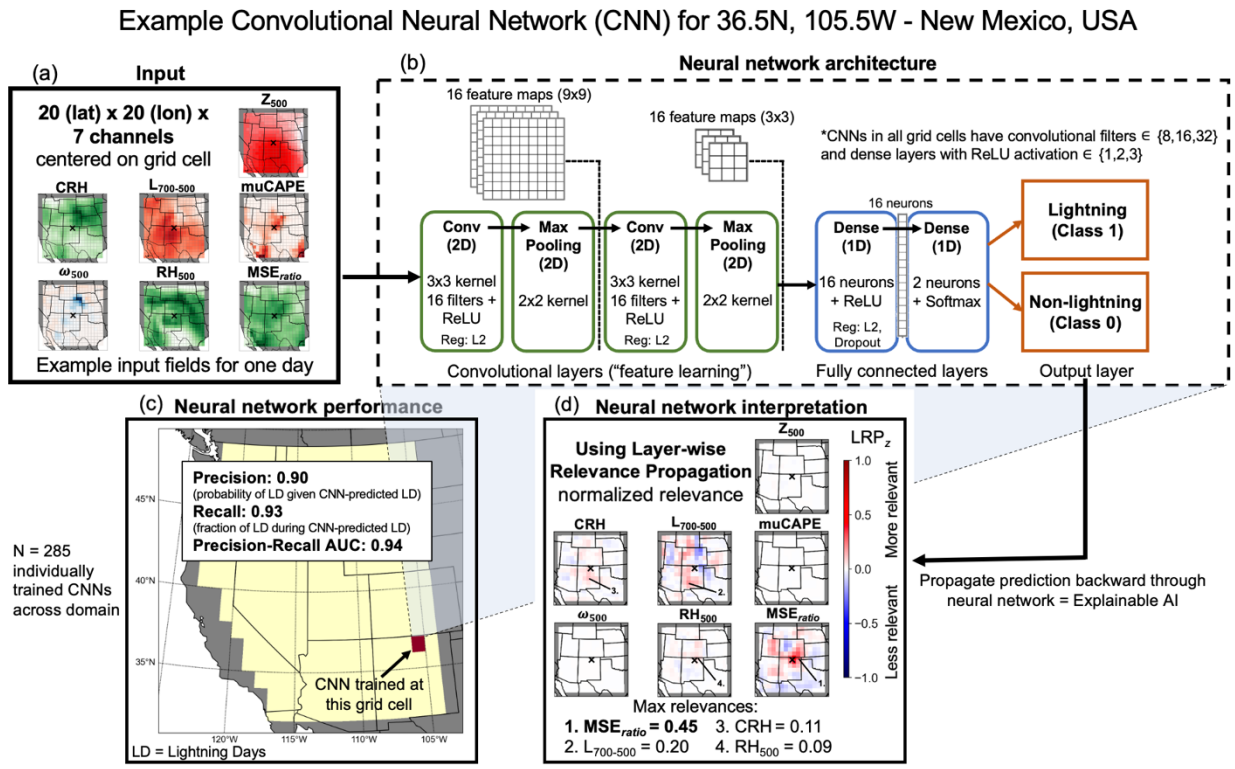

Figure 2. Example Convolutional Neural Network (CNN) trained at a grid cell in New Mexico (corresponding to the location with the largest number of lightning days in Figure 1b and denoted with black "x" in [a,d]) showing (a) input variables for one day interpolated to 2000 x 2000 km equal area grids centered on that grid cell, (b) schematic diagram of model architecture, and (c) model performance. (d) Composite relevance maps of each input variable for lightning predictions (Class 1), calculated using LRP_z. Red shading indicates positive contributions (relevance) to successful lightning predictions, with higher values indicating increased relevance. Inset numbers and marker lines in (d) indicate locations of maximum relevance for MSE_{ratio}, $L_{700\text{-}500}$, CRH, and RH_{500}, with corresponding values shown below (Z_{500}, muCAPE, and ω_{500} not shown due to low relevance).

We start with the same architecture for each CNN, but perform hyperparameter tuning separately for each grid cell. See Table S2 for a complete listing of tuned hyperparameters and the range of values over which optimization is conducted, and Figure S3 for the chosen hyperparameters at each grid cell. By adopting a comprehensive hyperparameter tuning strategy for each CNN, we seek to refine the approach of Cheng et al. (2024), who used a single CNN

architecture for all grid cells with a limited subset of tuned hyperparameters. A full description of the hyperparameter tuning process can be found in the supporting information.

The CNNs each have two convolutional layers that process input data utilizing 3x3 filters, each followed by a "max pooling" layer utilizing 2x2 filters. The output of the convolutional and max pooling layers is then passed to a set of 1-3 dense layers with 16 neurons each. An example of the CNN architecture for one location is shown in Figure 2b. We use He uniform initialization (He et al., 2015). The convolutional and first dense layer use the Rectified Linear Unit (ReLU) activation function. As a final step, inputs are vectorized and passed to a classification layer with two neurons and a Softmax activation function. Output from this layer consists of continuous probabilities of each classification (lightning or non-lightning) on that day scaled to a range of [0,1]. We define predicted lightning days as all days with a model-predicted lightning probability >0.5.

The CNNs are trained using 70% of the observed data (2391 days), with equal portions of the remaining 30% of the data withheld for validation and testing (Labe & Barnes, 2022). The validation dataset is used for hyperparameter tuning and early stopping during training, while the test dataset is withheld to assess the models' ability to generalize to unseen data. Due to class imbalance in many grid cells (Figure 1a), we use a stratified random split to ensure that training, validation, and testing datasets have the same ratio of lightning to non-lightning days. We train the CNNs using categorical cross-entropy as the loss function and the Adam gradient-descent optimizer (Kingma & Ba, 2014). Results obtained by using the RMSprop optimizer are similar (not shown). We use early stopping to end model training when validation loss begins to increase (patience = 10 epochs), which can help prevent overfitting (Davenport & Diffenbaugh, 2021).

See Figure S2 for the number of training epochs at each grid cell (WUS median = 210 epochs). The CNNs are built and trained using *TensorFlow 2.11.1* in Python (Abadi et al., 2015).

We use three metrics for evaluating the performance of the CNNs. *Precision* quantifies the fraction of CNN-predicted lightning days that actually observed lightning. We also quantify *recall*, also known as the Probability of Detection, which quantifies the fraction of observed lightning days that were correctly detected by the CNN, and the *precision-recall Area under the Curve (AUC)*, which synthesizes precision and recall into a single model performance metric (Figure 2c; an AUC > 0.5 indicates predictive skill that is better than random guessing). The precision-recall AUC is preferable to Receiver Operating Characteristic (ROC) AUC in this application due to the class imbalance in many grid cells (Davis & Goadrich, 2006). For each CNN, hyperparameters are tuned to maximize precision on the validation dataset. This choice of optimization metric is subjective and depends on the scientific problem (Davenport & Diffenbaugh, 2021). In our application, we seek to minimize false positives as this reduces overprediction of lightning.

2.5. CNN Explainability

Although the primary goal of this study is to predict lightning, we are also interested in understanding how the CNNs utilize the information contained in the predictor variables as this can yield physical insights. We use LRP, a post-hoc XAI technique, to interpret the CNN classifications following previous studies (Davenport & Diffenbaugh, 2021; Labe & Barnes, 2021, 2022; Mamalakis, Barnes, et al., 2022; Mamalakis, Ebert-Uphoff, et al., 2022; Toms et al., 2020). In this procedure, the CNNs are first trained, and the weights and biases are frozen. Then, daily predictions are propagated backward through the network while keeping track of the

relevance of information passed between neurons in different layers (Montavon et al., 2019). For each predictor variable, a heatmap of relevance scores is produced wherein locations with higher values indicate that their information was more relevant to the prediction. This illustrates a primary advantage of LRP since important features of the predictor variables can be visualized in the original spatial domain (McGovern et al., 2019; Davenport & Diffenbaugh, 2021). LRP is computed using the *iNNvestigate* Python package (version 2.0.2; Alber et al., 2019).

Although relevance maps are generated for all days including lightning and non-lightning predictions, we focus on visualizing relevance for lightning predictions only. We use the LRP_z variant (utilizing the *z*-rule for propagation; Bach et al., 2015) that allows us to track both positive and negative relevance (Labe & Barnes, 2022; Mamalakis, Ebert-Uphoff, et al., 2022). We also visualize relevance using a composite LRP variant (LRP_{comp}) following recommendations in Kohlbrenner et al. (2020). We implement LRP_{comp} using "LRPSequentialPresetA" from the *iNNvestigate* package, which consists of $LRP_{alpha\text{-}beta}$ (α=1, β=0) in the convolutional layers and $LRP_{epsilon}$ (ε=0.1) in the fully connected layers. Note that LRP_z is equivalent to the Input*Gradient XAI technique (Shrikumar et al., 2016) for neural networks that use ReLU activation (Mamalakis, Barnes, et al., 2022). Ultimately, the choice of XAI technique is subjective and no single method has consistently proven optimal (Bommer et al., 2023; Mamalakis, Barnes, et al., 2022; Molina et al., 2023; Sixt et al., 2019). Relevance maps are summed by grid cell for all lightning days in the period of record, and the summed values are further normalized across the predictor space to a range of [-1,1] for comparison of relative relevance. The resulting summed, normalized relevance maps indicate which variables, on average, contributed the most relevant information for successful lightning prediction and their corresponding spatial patterns. Since LRP_z output is inherently noisy and can be difficult to

interpret (Kohlbrenner et al., 2020; Montavon et al., 2019), the final LRP_z maps are smoothed with a gaussian filter (sigma = 0.8) to aid interpretation. Example LRP_z maps for the local CNN trained to predict lightning at 36.5N, 105.5W are shown in Figure 2d. To enable comparison of LRP values across all 285 CNNs, we extract the maximum LRP_z value for each variable (Figure 2d). For example, for this grid cell the maximum LRP_z value is associated with MSE_{ratio} (0.45) and is located at a pixel adjacent, and slightly northeast, of the lightning location (Figure 2d).

2.6. Logistic Regression

We compare the performance of CNNs in predicting lightning occurrence with logistic regression models (Bliss, 1935; McCullagh & Nelder, 1989) constructed at each 1° x 1° grid cell in the WUS to evaluate whether the CNNs provide an advantage over a traditional classification method. Logistic regression is a type of generalized linear model that, similar to CNNs, outputs a continuous probability of lightning occurrence for each day. We utilize the same seven meteorological variables as predictors. However, a key difference from CNNs is that inputs to the logistic regression consist only of the local value of each predictor from the grid cell for which the prediction is made, rather than the surrounding spatial fields. Logistic regression has been widely used for the prediction of climate phenomena both as a primary tool and as a baseline to compare with other machine learning approaches (Bates et al., 2018; Chattopadhyay et al., 2020; Etten-Bohm et al., 2021; Jergensen et al., 2019; Kamangir et al., 2020; Labe et al., 2023; Mayer & Barnes, 2021). Similar to the CNNs, we apply a hyperparameter tuning approach that seeks to maximize precision. We tune the L2 regularization factor and the magnitude of the class weights, and evaluate results using 4-fold cross validation. Logistic regression models are built and trained using the *scikit-learn* Python package (version 1.2.2; Pedregosa et al., 2011).

3. Results and Discussion

3.1. CNN Performance and Interpretation

The three performance metrics for all 285 local, individually-trained CNNs (one at each 1° x 1° grid cell) are shown in Figure 3a-f, and are obtained from the 15% of data that were withheld for testing at each grid cell. The median precision across the WUS is 0.76, recall is 0.77, and the AUC is 0.8 (Figure 3a-c). Across most of the WUS, AUC is substantially higher than 0.5, indicating that most local CNNs are skillful classifiers of lightning versus non-lightning days. Spatial variation in CNN performance is apparent and exhibits a nearly monotonic increase with increasing lightning fraction (Figure 3d-f). The best-performing models are in grid cells where lightning occurs on ≥60% of all warm-season days (Figure 1a) with a median precision/recall/AUC of 0.87/0.91/0.92, respectively (Figure 3d-f). This region encompasses Colorado and New Mexico and is under the direct influence of the North American Monsoon during the mid-late summer period, with frequent convective activity and therefore the largest sample size of lightning days for CNN training.

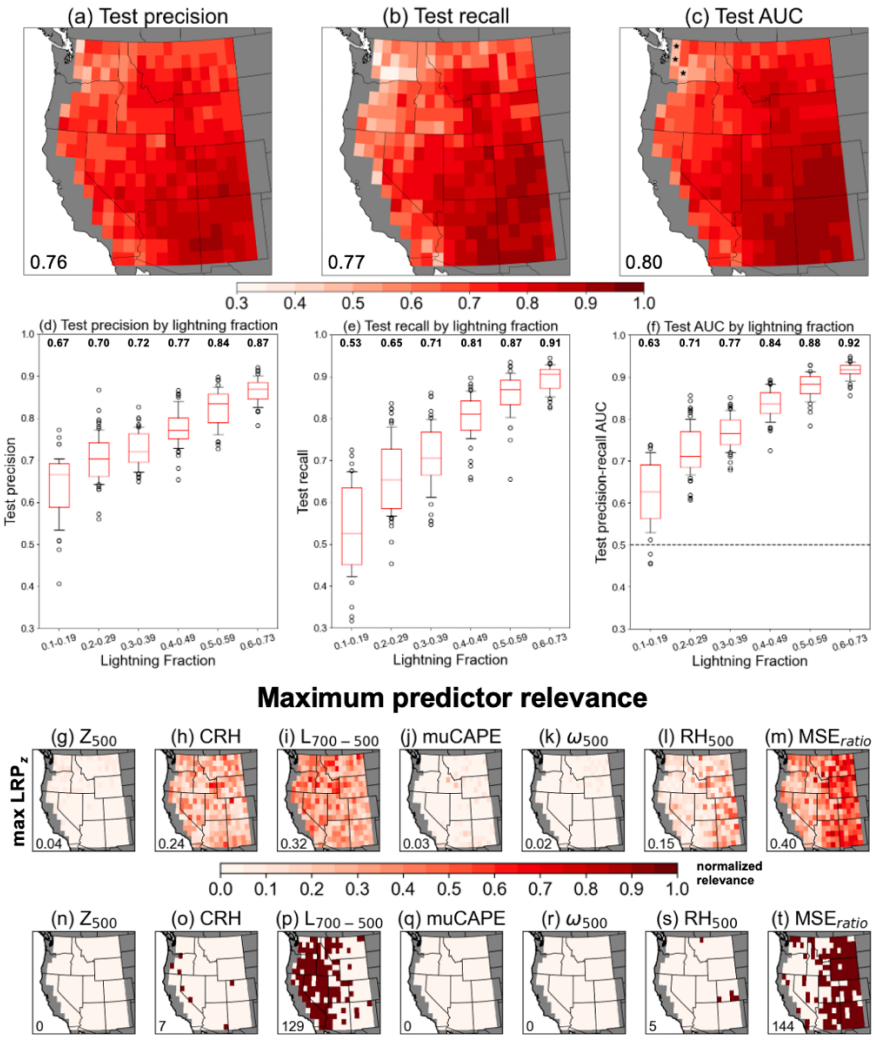

Figure 3. Performance metrics on test datasets for all CNNs individually trained in 1° x 1° grid cells (*n* = 285) quantified through (a) precision, (b) recall, and (c) precision-recall AUC. Inset text shows domain-median values. (d-f) Performance metrics binned by lightning fraction. Values above boxplots are the medians for each fraction bin. Dashed line in (f) corresponds to AUC = 0.5, indicating no predictive skill for a binary classifier, and black markers in (c) denote grid cells where AUC < 0.5. (g-m) Maximum relevance of each predictor for successful lightning-day predictions for each CNN computed from spatial fields of LRP_z (see Figure S5 for maximum relevance using LRP_{comp}). Higher values indicate increased relevance. Inset text shows mean domain-wide values of maximum relevance. (n-t) For each predictor, location of grid cells (maroon shading) where this predictor has highest relevance for successful lightning-day predictions in the corresponding CNN compared to the other variables. Inset text shows total number of CNNs where that predictor was most relevant.

The lowest performance is found in grid cells where lightning is rare, occurring on 10-19% of warm-season days (Figure 1a) and located in portions of interior Washington, Oregon, and California. In these grid cells, the median precision/recall/AUC is 0.67/0.53/0.63, respectively (Figure 3d-f). Although most grid cells have AUC > 0.5, three CNNs in central Washington have AUC < 0.5 indicating no improvement in lightning predictive ability over random guessing (Figure 3c). The lower classification performance in areas of infrequent lightning activity is similar to results obtained by Bates et al. (2018) for Australia, and could result from an insufficient sample size of lightning days for model training. Further, it is also possible that the chosen set of meteorological predictors may not fully describe lightning conditions here. This region lies at the periphery of the monsoonal circulation and is prone to high-based "dry" thunderstorms, which can produce lightning from narrow layers of elevated moisture and instability that may not be captured by our analysis (Abatzoglou et al., 2016; Kalashnikov, Abatzoglou, et al., 2022; Nauslar et al., 2013).

We assess the relevance of individual predictor variables to successful lightning-day predictions for each CNN (Figure 3g-t). For each variable and grid cell, the relevance maps show the maximum LRP_z (smoothed, see *Methods*) associated with lightning-day predictions for the CNN trained at that location. MSE_{ratio} has the highest domain-averaged maximum-LRP_z of 0.4, and is particularly high in the eastern half of the domain (Figure 3m; Figure S4). $L_{700\text{-}500}$ has the second-highest maximum-LRP_z of 0.32, with higher values in central and western portions of the domain (Figure 3i). MSE_{ratio} is the most relevant predictor variable for 144 of the CNNs (~51%; Figure 3t), mainly in the eastern half of the domain, while $L_{700\text{-}500}$ is the most relevant for an additional 129 CNNs (~45%; Figure 3p) mainly in the western half of the domain. Together, these variables represent the most relevant lightning predictors for 273 of the 285 CNNs (~96%).

The increased relevance of $L_{700\text{-}500}$ in areas further west is consistent with steepened mid-tropospheric lapse rates associated with lightning days outside the North American Monsoon core (Figure 1e), which promote convection by increasing instability (Kalashnikov et al., 2020; Kalashnikov, Abatzoglou, et al., 2022). The increased relevance of MSE_{ratio} in eastern areas is likely related to their location under the direct influence of the North American Monsoon. MSE_{ratio} is a relatively simple, surface-based proxy for convection and may sufficiently describe conditions favorable for lightning in this region where moisture, sensible heating, and orographic lifting for parcel ascent are frequently present during monsoon season (Adams & Souza, 2009). CRH does not show a clear spatial pattern with areas of higher and lower relevance throughout the WUS (Figure 3h), and RH_{500} appears to be more relevant over the eastern periphery (Figure 3l).

Results obtained from LRP_{comp} are similar with MSE_{ratio} and $L_{700\text{-}500}$ representing the most relevant predictors for ~93% of CNNs (Figure S5). However, $L_{700\text{-}500}$ is the most relevant predictor using LRP_{comp} when averaged across the WUS (Figure S5c; note that relevance values of LRP_z and LRP_{comp} are not directly comparable due to different propagation rules). Another notable difference when using LRP_{comp} compared to LRP_z is that CRH emerges as the most relevant predictor for 20 CNNs (~7%; Figure S5i), largely concentrated in the interior Northwest. The other predictor variables – Z_{500}, muCAPE, and ω_{500} – show much lower relevance for lightning predictions across the WUS when using both LRP_z and LRP_{comp} (Figure 3g,j,k; Figure S5a,d,e). These findings may be counterintuitive, particularly for muCAPE, which is widely used to quantify convective environments both in research and in operational forecasting. We note that it is important to distinguish between predictor relevance from the perspective of CNNs attempting to predict lightning and actual physical importance for convection and lightning

production. Since our goal is to predict the daily occurrence of lightning (≥1 cloud-to-ground flash) rather than the lightning flash density, it is likely that the CNNs prioritized the information contained in relatively simple convective proxies like MSE_{ratio} and $L_{700\text{-}500}$ during the training process.

To illustrate the contribution of local meteorological conditions on lightning days and their relevance to CNN predictions, we highlight a grid cell in northern Idaho (Figure 4; also highlighted as Cell 2 in Figure 5). This grid cell is located in the steep and forested terrain of the northern Rocky Mountains, an area of frequent lightning-caused wildfires during the warm season (Komarek, 1967; Werth & Ochoa, 1993). On lightning days, negative Z_{500} anomalies are present to the southwest of this grid cell with positive anomalies located to the northeast (Figure 4a). This composite reflects the canonical "ridge breakdown" pattern transition conducive to lightning activity over much of the arid interior WUS, as an incoming mid-level trough displaces ridging eastward (Dettinger et al., 1999; Kalashnikov et al., 2020; Werth & Ochoa, 1993). This pattern produces steeper $L_{700\text{-}500}$ than is typical on non-lightning days (Figure 4j) as colder air aloft advects over a residually warm surface airmass. The circulation around the trough additionally promotes mid-tropospheric moisture transport to the region from the south and southwest (Rorig & Ferguson, 1999). This is reflected in significantly ($P < 0.05$) increased values of CRH, RH_{500}, and MSE_{ratio} on lightning days (Figure 4i,m,n). Similarly, muCAPE (Figure 4k; increased values indicating more energy available for convection) and ω_{500} (Figure 4l; decreased values indicating greater upward vertical velocity) are significantly more favorable for convection on lightning versus non-lightning days.

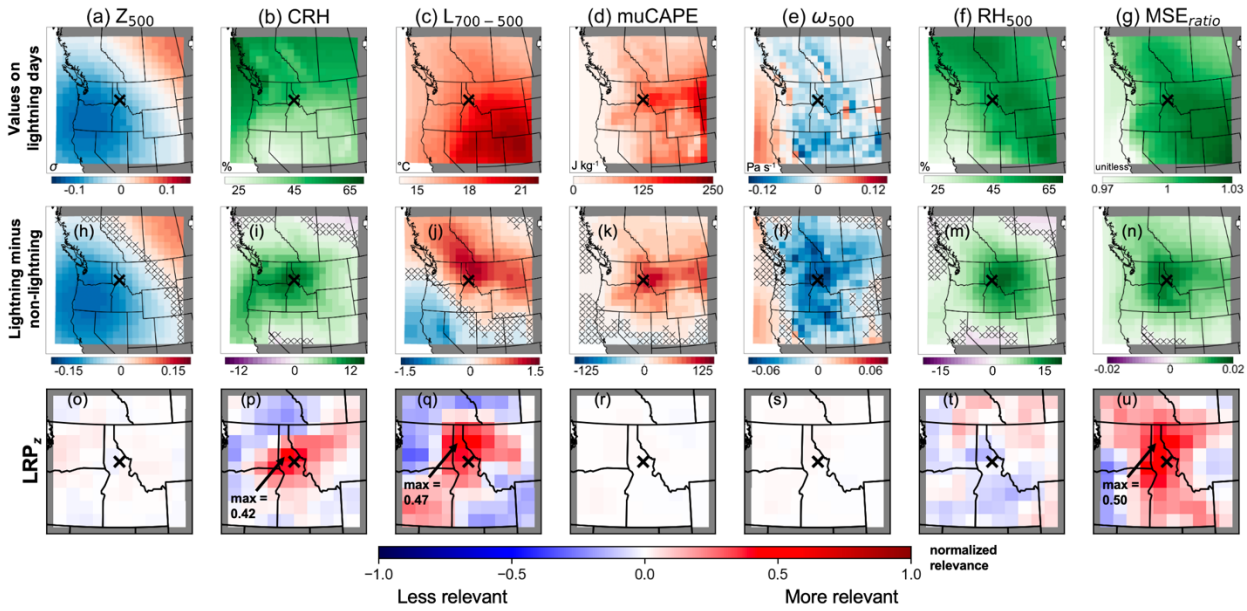

Figure 4. (a-g) Meteorological variables on lightning days for an example grid cell in northern Idaho (46.5N, 115.5W), denoted by black marker. (h-n) Difference in values of each variable on lightning days relative to non-lightning days at this example grid cell. (o-u) LRP_z fields showing relevance of individual pixels in each predictor's spatial field for successful lightning-day predictions. Red shading indicates positive contributions (relevance) to successful lightning predictions, with higher values indicating increased relevance. Inset numbers and arrows indicate locations of maximum relevance for (p) CRH, (q) $L_{700-500}$, and (u) MSE_{ratio}. Note that LRP_z maps are zoomed in to 1000 km domains around the target grid cell. Hatching in (h-n) indicates that differences are insignificant ($P \geq 0.05$) according to a two-tailed *t*-test.

MSE_{ratio} is the most relevant lightning predictor for the CNN trained at this grid cell, with maximum-LRP_z of 0.5 (Figure 4u). However, this is only nominally higher than the maximum-LRP_z for $L_{700-500}$ (0.47; Figure 4q) and CRH (0.42; Figure 4p), suggesting that all three variables are highly relevant to successful lightning prediction at this grid cell. Moreover, the CNN successfully utilized values of these variables from the wider region to make lightning predictions at this location (red shading in Figure 4p,q,u). Interestingly, the relevance values of RH_{500} are generally negative around the lightning location (blue shading, Figure 4t). RH_{500} patterns in these areas on lightning days therefore suggest to the CNN that lightning should *not* be predicted, representing a source of confusion or "contradictory evidence" (Kohlbrenner et al.,

2020). The reasons for this are unclear, as values of RH_{500} are significantly larger on lightning versus non-lightning days (Figure 4m) congruent with general enhancement of RH_{500} on lightning days across the domain in Figure (1h). Results from LRP_{comp} confirm the relevance of MSE_{ratio}, $L_{700\text{-}500}$, and CRH to lightning prediction at this grid cell (Figure S6). However, RH_{500} also appears relevant in disagreement with the negative relevance obtained from LRP_z (Figure S6f).

3.2. Comparison with Logistic Regression

We also compare results obtained from CNNs with those obtained from logistic regression models similarly trained at each 1° x 1° grid cell and optimized for precision. Overall, logistic regression performs comparably when aggregated across the WUS (median precision/recall/AUC of 0.71/0.83/0.8, respectively; Figure S7a-c). However, CNNs demonstrate improvement in precision across most of the WUS (in ~69.5% of grid cells; Figure S7d). Higher precision for CNNs is widespread and pronounced across the western and northern periphery, where some grid cells exhibit a >20% increase compared to logistic regression (Figure S7d). Our CNNs therefore help mitigate false positives in lightning classification by ensuring that a larger fraction of predicted lightning days observe lightning. However, some of these differences may result from the different levels of complexity in the hyperparameter tuning applied to CNNs versus logistic regression when optimizing for precision, as CNNs have more tunable parameters. Conversely, CNNs lead to generally lower recall (i.e., more false negatives, or lightning occurring on predicted "non-lightning" days) compared to logistic regression (~68% of grid cells have higher recall using logistic regression; Figure S7e). AUC values are generally similar, with ~47% of grid cells observing higher values using CNNs and ~53% using logistic

regression (Figure S7f). These results indicate that when considering overall model performance, CNNs do not offer a systematic advantage over logistic regression across the domain, and the best type of model to parameterize lightning may vary by location.

3.3. Lightning Parameterization

We apply the trained CNNs to meteorological fields over the full 1995-2022 period of record and generate predictions of lightning days (Figure 5). Figure 5a shows the total number of predicted lightning days over the study period and their spatial patterns. The geographical distribution of CNN-predicted lightning days is very similar to observations in Figure 1b, as the CNNs realistically capture the northwest-to-southeast gradient of increasing lightning activity across the WUS (Figure 5a). CNNs generally underpredict lightning days in the Pacific Northwest, western Great Basin, and northern Rockies where lightning is relatively rare (Figure 5b; Figure S8a). However, this underprediction could stem from our decision to optimize the CNNs for precision, which limits false positives but can lead to underprediction. Meanwhile, CNNs overpredict lightning days in the rest of the interior WUS where lightning occurs more frequently. However, across all CNNs, the differences between the total number of predicted lightning days and the number of observed lightning days are within 25% (Figure 5b). The CNNs additionally capture the seasonal cycle of lightning activity, with a pronounced peak in predicted lightning days over the interior Southwest in July-August similar to observations (Figure S9f-g). Our results demonstrate that CNNs are able to skillfully reproduce the long-term climatology of lightning days across the WUS over the historical period. Further, the locally-trained CNNs developed in this study appear to be substantially more skillful at predicting lightning over the WUS compared to recent, large-scale lightning parameterization efforts over the tropics and

subtropics. For example, Etten-Bohm et al. (2021) used a global logistic regression model and reported widespread underprediction of lightning days. Similarly, using regionally-trained Random Forest models to predict individual thunderstorms, Liu et al. (2022) noted large differences between predictions and observations locally exceeding 100%.

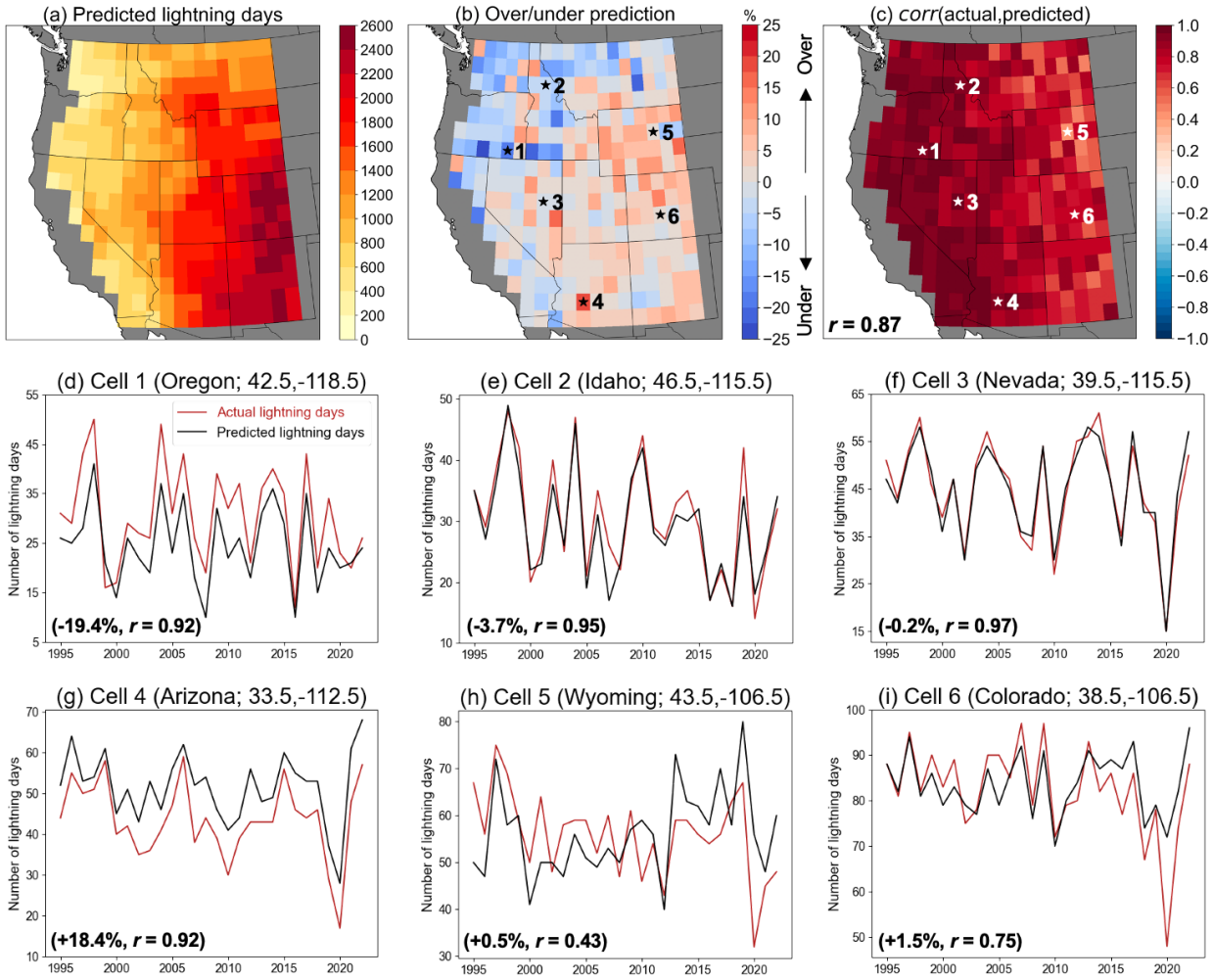

Figure 5. Lightning parameterization. (a) Total number of lightning days predicted by locally-trained CNNs between June-September (1995-2022), and (b) corresponding prediction error compared to observations. (c) Interannual correlation between actual and predicted lightning days, with inset text showing domain median. (d-i) Time series of actual and predicted lightning days for six example grid cells, with locations indicated in (b-c). Note that Cell 2 is the example grid cell highlighted in Figure 4. Text in the bottom left in (d-i) refers to the corresponding prediction errors and Pearson's correlation coefficients.

Interannual correlation between predicted and observed lightning days is shown in Figure 5c. The CNNs succeed in realistically capturing year-to-year variations in the number of lightning days across the WUS when compared to observations, as all correlation coefficients are between 0.43 and 0.99 (median $r = 0.87$). Nearly 40% of CNNs (113 of 285) have interannual correlation >0.9, largely concentrated in the western half of the domain (Figure 5c; Figure S8b). Generally lower correlation is found in the eastern half of the domain, where the median correlation reduces to 0.73 in grid cells with ≥60% lightning fraction (Figure S8b). These results represent a reversal of the spatial patterns in Figure 3, wherein higher model performance (based on classification metrics) is found in southeastern areas with lower performance further west. One possible explanation is that areas further west are reliant on transient episodes of favorable moisture and instability conditions to generate lightning activity, as they lie outside the monsoon core (Abatzoglou & Brown, 2009; Kalashnikov et al., 2020; Nauslar et al., 2013; van Wagtendonk & Cayan, 2008). Consequently, the frequency of these episodes is subject to higher interannual variability that may be easier for the CNNs to discern over seasonal timescales, compared to locations further east, resulting in higher interannual correlation with observations despite lower classification performance at the daily timescale (Figure 3).

We compare the actual and CNN-predicted lightning days over 1995-2022 at six example grid cells (Figure 5d-i), with the aim of studying cases of success and failure (Ebert-Uphoff & Hilburn, 2020). The CNN at Cell 1 (southeastern Oregon; Figure 5d) represents an example of high interannual correlation ($r = 0.92$) but with consistent underprediction (-19.4% over the period of record). Conversely, the CNN at Cell 4 (Arizona; Figure 5g) is an example of high interannual correlation ($r = 0.92$) but with consistent overprediction (+18.4%, largest in the domain). Cell 2 (northern Idaho; Figure 5e) and Cell 3 (Nevada; Figure 5f) are examples of both

high interannual correlation (r = 0.95 and 0.97, respectively) and low prediction error (-3.7% and -0.2%), and highlight the ability of the locally-trained CNNs to accurately reproduce the climatology of lightning days. On the other hand, the CNN at Cell 5 (Wyoming; Figure 5h) exhibits systematic underprediction until 2011 and overprediction in following years despite capturing most of the peaks in lightning activity (Figure 5h). The CNNs at this grid cell and Cell 6 (Colorado, Figure 5i) are notable for their inability to predict the magnitude of anomalously low lightning activity in 2020. The 2020 monsoon season was historically dry in the interior Southwest with limited convective activity (Hoell et al., 2022; Ren et al., 2022), and resulted in the lowest number of lightning days at five of the six example grid cells (all except Cell 1; Figure 5e-i). However, the lack of lightning days was better predicted by the CNNs further west, particularly in Cells 2 and 3 in Idaho and Nevada, respectively (Figure 5e-f).

To understand the systematic overprediction by the CNN for Cell 4 in Arizona, we compare composite values of the predictor variables for this CNN on false positive days, when lightning was predicted but did not occur, with values on true positive days when lightning was correctly predicted (Figure 6). On false positive days, quantities of moisture and convective energy are suppressed compared to true positive days, as CRH, muCAPE, RH_{500}, and MSE_{ratio} are significantly lower ($P < 0.05$) over the grid cell and surrounding region (Figure 6b,d,f,g). The absolute values of these variables are still generally high on false positive days (Figure S10), likely signaling to the CNN that at least marginally favorable conditions for convection exist and making it difficult to distinguish from true positive days. Values of Z_{500}, $L_{700\text{-}500}$, and ω_{500} are generally higher on false positive days but these differences are insignificant near the lightning location in all three cases (Figure 6a,c,e).

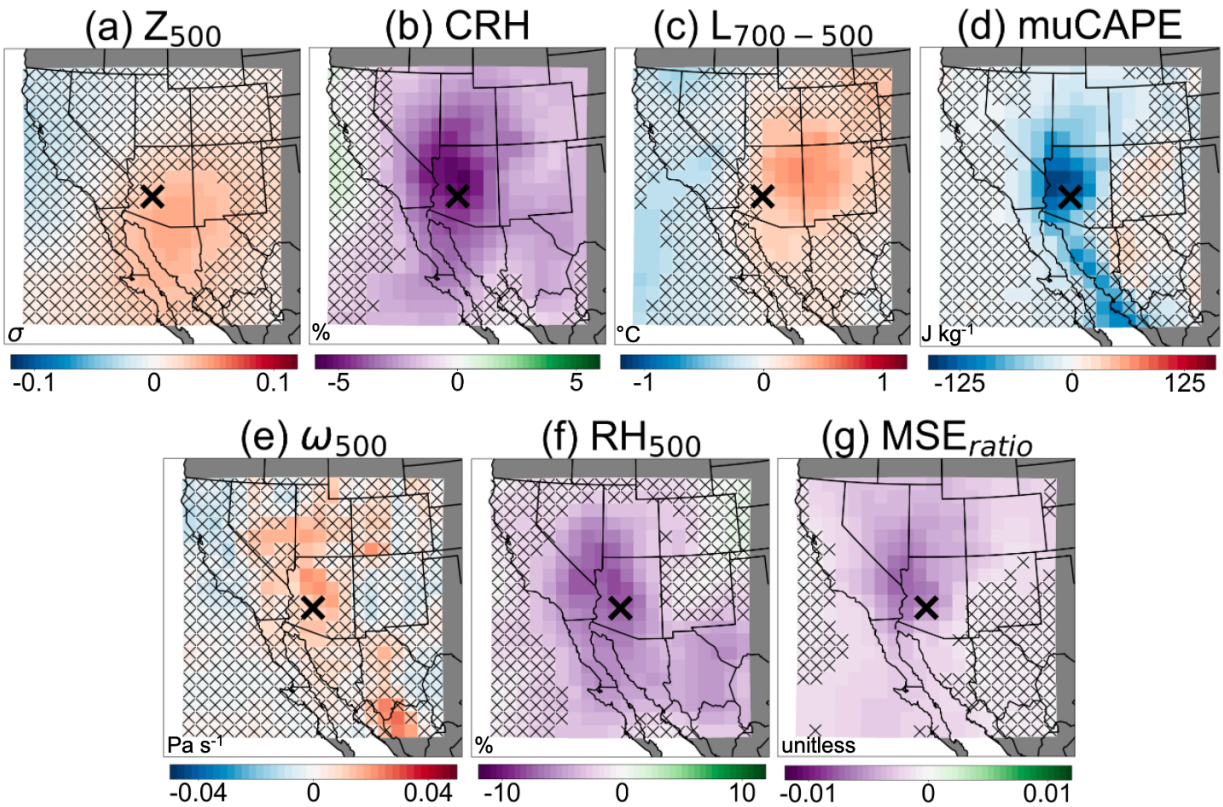

Figure 6. Difference in meteorological variables between false positive days (when lightning was predicted but did not occur) and true positive days (when lightning was correctly predicted) for the CNN with the largest overprediction in the domain (black marker). This grid cell is located in Arizona (33.5N, 112.5W) and corresponds to Cell 4 in Figure 5. Positive values indicate higher quantity on false positive days (false positive minus true positive). Hatching indicates that differences are insignificant ($P \geq 0.05$) between false positive and true positive days according to a two-tailed *t*-test.

3.4. Prediction Confidence

As CNNs output a continuous probability of lightning for each day, we examine this prediction probability ("confidence") on all predicted lightning days (i.e., days with a predicted lightning probability >0.5). In performing this analysis, we ask the question of whether lightning days with high prediction confidence (closer to 1) exhibit meaningfully different characteristics compared to days with lower prediction confidence (closer to 0.5). The CNNs generally predict lightning with high confidence across the WUS (median = 0.86; Figure 7a). Prediction confidence tends to be higher in the western parts of the domain and lower over Montana and

Wyoming, where the geography shifts to the Great Plains with a different climatology compared to the rest of the WUS. Days when lightning was correctly predicted have a systematically higher prediction confidence compared to days when lightning was falsely predicted across all CNNs (Figure 7b). This finding confirms that CNN predictions are more likely to be physically correct with higher prediction confidence, in agreement with Mayer & Barnes (2021).

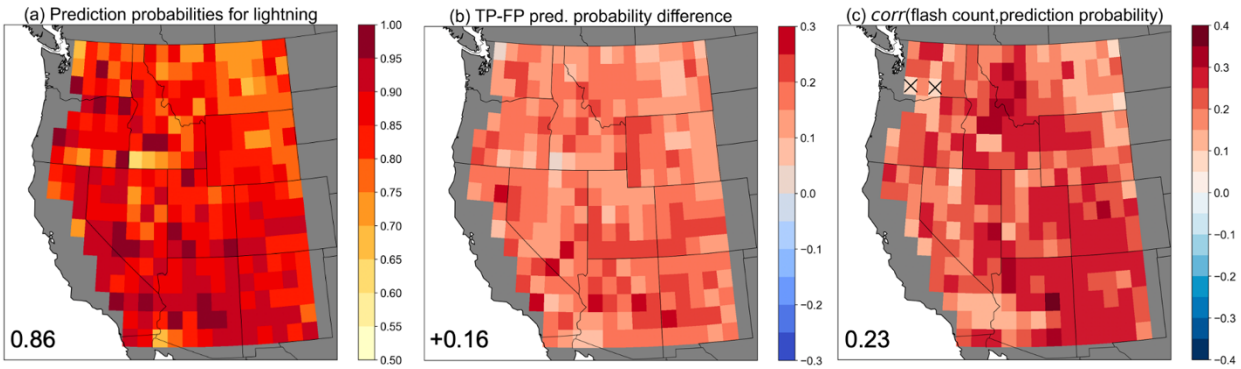

Figure 7. (a) Median prediction probabilities ("confidence") for all days on which lightning was predicted by locally-trained CNNs in each grid cell. (b) Differences in lightning-day prediction confidence between true positive days (TP) and false positive days (FP). (c) Correlation coefficients between lightning-day prediction confidence and the total number of observed cloud-to-ground lightning flashes on that day. Hatching in (c) indicates that correlation is insignificant ($P \geq 0.05$). Inset text shows domain-median values.

Further, all CNNs exhibit positive correlation between prediction confidence and the total *quantity* of cloud-to-ground lightning flashes on that day. This correlation, although weak (domain median $r = 0.23$), is significant at all but two CNNs in the WUS (Figure 7c). We also analyze the top-10% most confident lightning-day predictions for each CNN (Mayer & Barnes, 2021). Lightning flash counts on days with the top-10% most confident lightning predictions are typically higher by a factor of 2.47 (domain median) compared to days with less confident lightning predictions (Figure S11). These results carry important implications for applying our CNN-based lightning parameterizations to GCMs, as an increase in cloud-to-ground lightning

flash quantity can be expected for more confident predictions in future climates, leading to refined projections of wildfire ignition risk when weather and fuel conditions align.

4. Summary and Conclusions

In this study, we develop locally-trained CNNs at each 1° x 1° grid cell in the WUS to predict the daily occurrence of cloud-to-ground lightning over June-September, 1995-2022. Two-dimensional fields of seven dynamic and thermodynamic meteorological variables are used as predictors in the CNNs – Z_{500}, CRH, $L_{700\text{-}500}$, muCAPE, ω_{500}, RH_{500}, and MSE_{ratio}. All seven variables show significant differences between lightning and non-lightning days across most of the domain, with values of moisture and instability significantly larger on lightning days (Figure 1). The locally-trained CNNs are skillful at predicting lightning occurrence across the WUS (median AUC = 0.8) and perform best in parts of the interior Southwest where summertime lightning is most common (AUC > 0.9) (Figure 3). CNN classification performance is similar to baseline logistic regression models across the domain in terms of AUC, but outperforms logistic regression when using precision as the benchmark at ~69% of grid cells. Our CNNs therefore offer a more conservative approach to parameterizing lightning as the false positive rate, or lightning overprediction, is minimized compared to logistic regression in the majority of the WUS.

We use LRP_z, an XAI technique, to investigate the regional relevance of predictor variables to successful lightning prediction. Using maximum LRP_z values, our results show that MSE_{ratio} and $L_{700\text{-}500}$ are consistently most relevant, and together represent the top lightning predictors for ~96% of CNNs (Figure 3). These results are largely consistent when using a different XAI technique (LRP_{comp}), and suggest an important role for relatively simple convective proxies when

predicting the occurrence of cloud-to-ground lightning on daily timescales. We acknowledge that other variables that are physically important for lightning might not be prioritized by the CNNs during training (leading to lower relevance), likely due to variables such as MSE_{ratio} and $L_{700\text{-}500}$ offering more direct proxies for convection. Additionally, XAI techniques can struggle to produce physically truthful explanations when multicollinearity between predictors is present (Au et al., 2022; Krell et al., 2023).

To test the ability of the locally-trained CNNs to reliably parameterize lightning occurrence across the WUS, we apply the trained models to meteorological fields over the full 1995-2022 period and generate lightning-day predictions. Although there is general underprediction along the northern and western periphery and overprediction elsewhere, the differences between predicted and observed lightning days are within 25% for all CNNs (Figure 5b). Strong interannual correlation (domain median $r = 0.87$) between observed and predicted lightning days demonstrates that the CNNs also realistically capture year-to-year variation in lightning activity across the WUS (Figure 5c). Additionally, we show that higher prediction confidence on individual days leads to more accurate predictions and correlates with increased lightning activity (Figure 7).

We note several possible limitations to our analysis. First, the relatively short cloud-to-ground lightning data record limits the sample size for training CNNs, particularly in western parts of the domain where lightning is rare. Second, the predictor variables used herein are spatially averaged over 1° degree latitude-longitude and to a daily resolution, which could mask conditions favorable for lightning activity on finer spatial and sub-daily timescales. In particular, this could help explain the lower classification performance in Pacific coastal states where lightning depends on more transient episodes of favorable meteorological conditions compared

to areas in the monsoon core. Alternately, it is also possible that conditions may appear conducive to lightning at the daily resolution, but the necessary combination of ingredients may not align at the sub-daily scale to produce thunderstorms. Third, constraints of the NLDN sensor network and the MERRA-2 reanalysis could affect the identification of lightning and non-lightning days and the CNN training based on the associated meteorological conditions. For instance, some cloud-to-ground lightning may be missed by the NLDN, which has a 95% detection efficiency (Nag, 2014). Further, reanalysis products may not always reliably simulate convective parameters compared to sounding observations (Taszarek et al., 2018).

Our manuscript makes a novel contribution to predicting lightning by using CNNs compared to existing parameterization efforts that use logistic regression or Random Forests, since CNNs are nonlinear and explicitly incorporate spatial information of predictor variables. The CNNs are therefore able to capture spatial fields of input variables that may hold predictive clues beyond their local values at that grid cell, and XAI techniques can illustrate the importance of spatial features thus yielding physical insights into these predictions. Our methodology could be extended to predict days at higher thresholds of lightning activity or days with dry lightning (occurring with <2.5 mm daily precipitation). An important application of our CNN-based parameterizations is their use in GCMs to evaluate potential changes in lightning under different climates, a challenging problem that currently has high uncertainty since lightning is not directly simulated by GCMs. Our parameterizations are based on variables that are simulated by GCMs and avoid using cloud, precipitation, and convective mass variables that need to be parameterized in GCMs and can have large uncertainties (Etten-Bohm et al., 2021). The locally-trained CNNs developed in this study appear to be substantially more skillful at predicting lightning over the WUS compared to recent, large-scale lightning parameterizations over the

tropics and subtropics (e.g., Etten-Bohm et al., 2021; Liu et al., 2022), highlighting the advantages of localized parameterizations. Applying the parameterizations developed in this study to GCMs would enable the quantification of future lightning activity across the WUS and refine projections of lightning-caused wildfires.

Acknowledgments

We thank Vaisala, Inc. for collecting the NLDN lightning data used in this study. This research used resources from the Center for Institutional Research Computing at Washington State University. This work was supported by NASA awards 80NSSC21K1603 (DAK and DS) and 80NSSC21K1501 (PCL), and by NSF award OAI-2019762 (JTA). ZML acknowledges support under CIMES award NA18OAR4320123 from the National Oceanic and Atmospheric Administration (NOAA), U.S. Department of Commerce. We express our gratitude to Hugo Kyo Lee and Yunsoo Choi for initial methodological discussions during 2019 NASA Jet Propulsion Laboratory internship (DAK).

Open Research

NLDN data are sourced from the National Centers for Environmental Information Severe Weather Data Inventory (https://www.ncei.noaa.gov/pub/data/swdi/database-csv/v2/). MERRA-2 data were acquired from NASA's Goddard Earth Sciences Data Information Services Center (GES DISC; https://disc.gsfc.nasa.gov/datasets?keywords=merra-2&page=1). Datasets used to perform analyses are available at the following Zenodo repository: https://doi.org/10.5281/zenodo.10685571 (Kalashnikov, 2024a). Analysis code can be accessed at the following GitHub repository: https://github.com/dmitri1357/CNNs-lightning-prediction (Kalashnikov, 2024b).

References

Abadi, M., Agarwal, A., Barham, P., Brevdo, E., Chen, Z., Citro, C., et al. (2015). TensorFlow: Large-scale machine learning on heterogeneous distributed systems. Retrieved from https://static.googleusercontent.com/media/research.google.com/en//pubs/archive/45166.pdf

Abatzoglou, J. T., & Brown, T. J. (2009). Influence of the Madden–Julian oscillation on summertime cloud-to-ground lightning activity over the continental United States. *Monthly Weather Review*, *137*(10), 3596–3601. https://doi.org/10.1175/2009MWR3019.1

Abatzoglou, J. T., Kolden, C. A., Balch, J. K., & Bradley, B. A. (2016). Controls on interannual variability in lightning-caused fire activity in the western US. *Environmental Research Letters*, *11*(4), 045005. https://doi.org/10.1088/1748-9326/11/4/045005

Adams, D. K., & Comrie, A. C. (1997). The North American monsoon. *Bulletin of the American Meteorological Society*, *78*(10), 2197–2213. https://doi.org/10.1175/1520-0477(1997)078<2197:TNAM>2.0.CO;2

Adams, D. K., & Souza, E. P. (2009). CAPE and convective events in the Southwest during the North American monsoon. *Monthly Weather Review*, *137*(1), 83–98. https://doi.org/10.1175/2008MWR2502.1

Alber, M., Lapuschkin, S., Seegerer, P., Hägele, M., Schütt, K. T., Montavon, G, et al. (2019). iNNvestigate neural networks! *Journal of Machine Learning Research*, *20*(93), 1-8. Retrieved from https://www.jmlr.org/papers/volume20/18-540/18-540.pdf

Allen, D. J., & Pickering, K. E. (2002). Evaluation of lightning flash rate parameterizations for use in a global chemical transport model. *Journal of Geophysical Research*, *107*(D23), ACH 15-1-ACH 15-21. https://doi.org/10.1029/2002JD002066

Au, Q., Herbinger, J., Stachl, C., Bischl, B., & Casalicchio, G. (2022). Grouped feature importance and combined features effect plot. *Data Mining and Knowledge Discovery*, *36*(4), 1401–1450. https://doi.org/10.1007/s10618-022-00840-5

Bach, S., Binder, A., Montavon, G., Klauschen, F., Müller, K.-R., & Samek, W. (2015). On pixel-wise explanations for non-linear classifier decisions by layer-wise relevance propagation. *PloS One*, *10*(7), e0130140. https://doi.org/10.1371/journal.pone.0130140

Balch, J. K., Bradley, B. A., Abatzoglou, J. T., Nagy, R. C., Fusco, E. J., & Mahood, A. L. (2017). Human-started wildfires expand the fire niche across the United States. *Proceedings of the National Academy of Sciences of the United States of America*, *114*(11), 2946–2951. https://doi.org/10.1073/pnas.1617394114

Baño-Medina, J., Manzanas, R., & Gutiérrez, J. M. (2021). On the suitability of deep convolutional neural networks for continental-wide downscaling of climate change projections. *Climate Dynamics*, *57*(11–12), 2941–2951. https://doi.org/10.1007/s00382-021-05847-0

Barlow, M., Nigam, S., & Berbery, E. H. (1998). Evolution of the North American monsoon system. *Journal of Climate*, *11*(9), 2238–2257. https://doi.org/10.1175/1520-0442(1998)011<2238:EOTNAM>2.0.CO;2

Barros, A. M. G., Day, M. A., Preisler, H. K., Abatzoglou, J. T., Krawchuk, M. A., Houtman, R., & Ager, A. A. (2021). Contrasting the role of human- and lightning-caused wildfires on

future fire regimes on a Central Oregon landscape. *Environmental Research Letters*, *16*(6), 064081. https://doi.org/10.1088/1748-9326/ac03da

Bates, B. C., Dowdy, A. J., & Chandler, R. E. (2018). Lightning prediction for Australia using multivariate analyses of large-scale atmospheric variables. *Journal of Applied Meteorology and Climatology*, *57*(3), 525–534. https://doi.org/10.1175/JAMC-D-17-0214.1

Beucler, T., Gentine, P., Yuval, J., Gupta, A., Peng, L., Lin, J., et al. (2024). Climate-invariant machine learning. *Science Advances*, *10*(6), adj7250. https://doi.org/10.1126/sciadv.adj7250

Bliss, C. I. (1935). The calculation of the dosage-mortality curve. *Annals of Applied Biology*, 22, 134-167. https://doi.org/10.1111/j.1744-7348.1935.tb07713.x

Bommer, P., Kretschmer, M., Hedström, A., Bareeva, D., & Höhne, M. M.-C. (2023). Finding the right XAI method -- A Guide for the Evaluation and Ranking of Explainable AI Methods in Climate Science. *arXiv [cs.LG]*. Retrieved from https://arxiv.org/abs/2303.00652

Brey, S. J., Barnes, E. A., Pierce, J. R., Wiedinmyer, C., & Fischer, E. V. (2018). Environmental conditions, ignition type, and air quality impacts of wildfires in the southeastern and western United States. *Earth's Future*, *6*(10), 1442–1456. https://doi.org/10.1029/2018EF000972

Burrows, W. R., Price, C., & Wilson, L. J. (2005). Warm season lightning probability prediction for Canada and the northern United States. *Weather and Forecasting*, *20*(6), 971–988. https://doi.org/10.1175/WAF895.1

Chattopadhyay, A., Hassanzadeh, P., & Pasha, S. (2020). Predicting clustered weather patterns: A test case for applications of convolutional neural networks to spatio-temporal climate data. *Scientific Reports*, *10*(1), 1-13. https://doi.org/10.1038/s41598-020-57897-9

Chen, Y., Romps, D. M., Seeley, J. T., Veraverbeke, S., Riley, W. J., Mekonnen, Z. A., & Randerson, J. T. (2021). Future increases in Arctic lightning and fire risk for permafrost carbon. *Nature Climate Change*, *11*(5), 404–410. https://doi.org/10.1038/s41558-021-01011-y

Cheng, W.-Y., Kim, D., Henderson, S., Ham, Y.-G., Kim, J.-H., & Holzworth, R. H. (2024). Machine learning based lightning parameterizations for CONUS. *Artificial Intelligence for the Earth Systems*, Early Online Release. https://doi.org/10.1175/AIES-D-23-0024.1

Clark, S. K., Ward, D. S., & Mahowald, N. M. (2017). Parameterization-based uncertainty in future lightning flash density. *Geophysical Research Letters*, *44*(6), 2893–2901. https://doi.org/10.1002/2017GL073017

Dagon, K., Truesdale, J., Biard, J. C., Kunkel, K. E., Meehl, G. A., & Molina, M. J. (2022). Machine learning-based detection of weather fronts and associated extreme precipitation in historical and future climates. *Journal of Geophysical Research Atmospheres*, *127*(21), e2022JD037038. https://doi.org/10.1029/2022jd037038

Davenport, F. V., & Diffenbaugh, N. S. (2021). Using machine learning to analyze physical causes of climate change: A case study of U.S. Midwest extreme precipitation. *Geophysical Research Letters*, *48*(15), e2021GL093787. https://doi.org/10.1029/2021gl093787

Davis, J., & Goadrich, M. (2006). The relationship between Precision-Recall and ROC curves. In *Proceedings of the 23rd international conference on Machine learning - ICML '06*. New York, New York, USA: ACM Press. https://doi.org/10.1145/1143844.1143874

Dettinger, M. D., Cayan, D. R., & Brown, T. J. (1999). Summertime intraseasonal and interannual lightning variations in the western United States. In *Proceedings of the 24th Annual NOAA Climate Diagnostics and Prediction Workshop*, Tucson, Arizona, USA.

Douville, H., Qasmi, S., Ribes, A., & Bock, O. (2022). Global warming at near-constant tropospheric relative humidity is supported by observations. *Communications Earth & Environment*, *3*(1), 1-7. https://doi.org/10.1038/s43247-022-00561-z

Ebert-Uphoff, I., & Hilburn, K. (2020). Evaluation, tuning, and interpretation of neural networks for working with images in meteorological applications. *Bulletin of the American Meteorological Society*, *101*(12), E2149–E2170. https://doi.org/10.1175/BAMS-D-20-0097.1

Etten-Bohm, M., Yang, J., Schumacher, C., & Jun, M. (2021). Evaluating the relationship between lightning and the large-scale environment and its use for lightning prediction in global climate models. *Journal of Geophysical Research Atmospheres*, *126*(5), e2020JD033990. https://doi.org/10.1029/2020jd033990

Finney, D. L., Doherty, R. M., Wild, O., Huntrieser, H., Pumphrey, H. C., & Blyth, A. M. (2014). Using cloud ice flux to parametrise large-scale lightning. *Atmospheric Chemistry and Physics*, *14*(23), 12665–12682. https://doi.org/10.5194/acp-14-12665-2014

Finney, D. L., Doherty, R. M., Wild, O., & Abraham, N. L. (2016). The impact of lightning on tropospheric ozone chemistry using a new global lightning parametrisation. *Atmospheric Chemistry and Physics*, *16*(12), 7507–7522. https://doi.org/10.5194/acp-16-7507-2016

Finney, D. L., Doherty, R. M., Wild, O., Stevenson, D. S., MacKenzie, I. A., & Blyth, A. M. (2018). A projected decrease in lightning under climate change. *Nature Climate Change*, *8*(3), 210–213. https://doi.org/10.1038/s41558-018-0072-6

Gelaro, R., McCarty, W., Suárez, M. J., Todling, R., Molod, A., Takacs, L., et al. (2017). The modern-Era Retrospective Analysis for Research and Applications, Version 2 (MERRA-2). *Journal of Climate*, *30*(13), 5419–5454. https://doi.org/10.1175/JCLI-D-16-0758.1

Goodfellow, I., Bengio, Y., & Courville, A. (2016). Deep Learning. *MIT Press*. Retrieved from: https://www.deeplearningbook.org/

Han, Y., Luo, H., Wu, Y., Zhang, Y., & Dong, W. (2021). Cloud ice fraction governs lightning rate at a global scale. *Communications Earth & Environment*, *2*(1), 1-9. https://doi.org/10.1038/s43247-021-00233-4

He, K., Zhang, X., Ren, S., Sun, J. (2015). Delving deep into rectifiers: Surpassing human-level performance on ImageNet classification. In *Proceedings of the IEEE International Conference on Computer Vision (ICCV), 2015*, 1026-1034. Retrieved from https://openaccess.thecvf.com/content_iccv_2015/html/He_Delving_Deep_into_ICCV_2015_paper.html

Hoell, A., Quan, X.-W., Hoerling, M., Fu, R., Mankin, J., Simpson, I., et al. (2022). Record low North American monsoon rainfall in 2020 reignites drought over the American southwest. *Bulletin of the American Meteorological Society*, *103*(3), S26–S32. https://doi.org/10.1175/BAMS-D-21-0129.1

Janssen, T. A. J., Jones, M. W., Finney, D., van der Werf, G. R., van Wees, D., Xu, W., & Veraverbeke, S. (2023). Extratropical forests increasingly at risk due to lightning fires. *Nature Geoscience*, *16*, 1136-1144. https://doi.org/10.1038/s41561-023-01322-z

Jergensen, G. E., McGovern, A., Lagerquist, R., & Smith, T. (2019). Classifying convective storms using machine learning. *Weather and Forecasting*, *35*(2), 537–559. https://doi.org/10.1175/WAF-D-19-0170.1

Kalashnikov, D. A. (2024a). Supporting datasets for CNNs-lightning prediction paper (Version 1) [Dataset]. Zenodo. https://doi.org/10.5281/zenodo.10685571

Kalashnikov, D. A. (2024b). dmitri1357/CNNs-lightning-prediction [Software]. GitHub. Available at: https://github.com/dmitri1357/CNNs-lightning-prediction

Kalashnikov, D. A., Loikith, P. C., Catalano, A. J., Waliser, D. E., Lee, H., & Abatzoglou, J. T. (2020). A 30-yr climatology of meteorological conditions associated with lightning days in the interior western United States. *Journal of Climate*, *33*(9), 3771–3785. https://doi.org/10.1175/JCLI-D-19-0564.1

Kalashnikov, D. A., Schnell, J. L., Abatzoglou, J. T., Swain, D. L., & Singh, D. (2022). Increasing co-occurrence of fine particulate matter and ground-level ozone extremes in the western United States. *Science Advances*, *8*(1), eabi9386. https://doi.org/10.1126/sciadv.abi9386

Kalashnikov, D. A., Abatzoglou, J. T., Nauslar, N. J., Swain, D. L., Touma, D., & Singh, D. (2022). Meteorological and geographical factors associated with dry lightning in central and northern California. *Environmental Research: Climate*, *1*(2), 025001. https://doi.org/10.1088/2752-5295/ac84a0

Kalashnikov, D. A., Abatzoglou, J. T., Loikith, P. C., Nauslar, N. J., Bekris, Y., & Singh, D. (2023). Lightning-ignited wildfires in the western United States: Ignition precipitation and associated environmental conditions. *Geophysical Research Letters*, *50*(16), e2023GL103785. https://doi.org/10.1029/2023GL103785

Kamangir, H., Collins, W., Tissot, P., & King, S. A. (2020). A deep-learning model to predict thunderstorms within 400 km^2 South Texas domains. *Meteorological Applications*, *27*(2), e1905. https://doi.org/10.1002/met.1905

Kingma, D. P., & Ba, J. (2014). Adam: A method for stochastic optimization. *arXiv [cs.LG]*. Retrieved from https://arxiv.org/abs/1412.6980

Kohlbrenner, M., Bauer, A., Nakajima, S., Binder, A., Samek, W., & Lapuschkin, S. (2020). Towards best practice in explaining neural network decisions with LRP. In *2020 International Joint Conference on Neural Networks (IJCNN)*. Glasgow, United Kingdom: IEEE. https://doi.org/10.1109/ijcnn48605.2020.9206975

Komarek, E. V. Sr. (1967). The nature of lightning fires. In *Proceedings 7th Tall Timbers Fire Ecology Conference*, 5–41. Retrieved from https://talltimbers.org/wp-content/uploads/2014/03/Komarek1967_op-1.pdf

Krause, A., Kloster, S., Wilkenskjeld, S., Paeth, H. (2014). The sensitivity of global wildfires to simulated past, present, and future lightning frequency. *Journal of Geophysical Research: Biogeosciences*, *119*, 312-322. https://doi.org/10.1002/2013JG002502

Krell, E., Kamangir, H., Collins, W., King, S. A., & Tissot, P. (2023). Aggregation strategies to improve XAI for geoscience models that use correlated, high-dimensional rasters. *Environmental Data Science*, *2*(e45), 1-22. https://10.1017/eds.2023.39

Krumm, W. R. (1954). On the cause of downdrafts from dry thunderstorms over the plateau area of the United States. *Bulletin of the American Meteorological Society*, *35*(3), 122–125.

Labe, Z. M., & Barnes, E. A. (2021). Detecting climate signals using explainable AI with single-forcing large ensembles. *Journal of Advances in Modeling Earth Systems*, *13*(6), e2021MS002464. https://doi.org/10.1029/2021ms002464

Labe, Z. M., & Barnes, E. A. (2022). Predicting slowdowns in decadal climate warming trends with explainable neural networks. *Geophysical Research Letters*, *49*(9), e2022GL098173. https://doi.org/10.1029/2022gl098173

Labe, Z. M., Barnes, E. A., & Hurrell, J. W. (2023). Identifying the regional emergence of climate patterns in the ARISE-SAI-1.5 simulations. *Environmental Research Letters*, *18*(4), 044031. https://doi.org/10.1088/1748-9326/acc81a

Lagerquist, R., McGovern, A., & Gagne, D. J., II. (2019). Deep learning for spatially explicit prediction of synoptic-scale fronts. *Weather and Forecasting*, *34*(4), 1137–1160. https://doi.org/10.1175/WAF-D-18-0183.1

LeCun, Y., Bengio, Y., Hinton, G. (2015). Deep learning. *Nature*, *521*, 436-444. https://doi.org/10.1038/nature14539

Li, Y., Mickley, L. J., Liu, P., & Kaplan, J. O. (2020). Trends and spatial shifts in lightning fires and smoke concentrations in response to 21st century climate over the national forests and parks of the western United States. *Atmospheric Chemistry and Physics*, *20*(14), 8827–8838. https://doi.org/10.5194/acp-20-8827-2020

Liu, N., Liu, C., & Tissot, P. E. (2022). Relative importance of large-scale environmental variables to the world-wide variability of thunderstorms. *Journal of Geophysical Research Atmospheres*, *127*(17), e2021JD036065. https://doi.org/10.1029/2021jd036065

Luong, T. M., Castro, C. L., Chang, H.-I., Lahmers, T., Adams, D. K., & Ochoa-Moya, C. A. (2017). The More Extreme Nature of North American Monsoon Precipitation in the Southwestern United States as Revealed by a Historical Climatology of Simulated Severe Weather Events. *Journal of Applied Meteorology and Climatology*, *56*(9), 2509-2529. https://doi.org/10.1175/JAMC-D-16-0358.1

Magi, B. I. (2015). Global lightning parameterization from CMIP5 climate model output. *Journal of Atmospheric and Oceanic Technology*, *32*(3), 434–452. https://doi.org/10.1175/JTECH-D-13-00261.1

Mamalakis, A., Barnes, E. A., & Ebert-Uphoff, I. (2022). Investigating the fidelity of explainable artificial intelligence methods for applications of convolutional neural networks in geoscience. *Artificial Intelligence for the Earth Systems*, *1*(4), 1–42. https://doi.org/10.1175/AIES-D-22-0012.1

Mamalakis, A., Ebert-Uphoff, I., & Barnes, E. A. (2022). Neural network attribution methods for problems in geoscience: A novel synthetic benchmark dataset. *Environmental Data Science*, *1*(e8), 1-17. https://doi.org/10.1017/eds.2022.7

Mamalakis, A., Barnes, E. A., & Hurrell, J. W. (2023). Using explainable artificial intelligence to quantify "climate distinguishability" after stratospheric aerosol injection. *Geophysical Research Letters*, *50*(20), e2023GL106137. https://doi.org/10.1029/2023gl106137

May R. M., et al. (2023). MetPy: A Python package for meteorological data. *Unidata*. https://doi.org/10.5065/D6WW7G29

Mayer, K. J., & Barnes, E. A. (2021). Subseasonal forecasts of opportunity identified by an explainable neural network. *Geophysical Research Letters*, *48*(10), e2020GL092092. https://doi.org/10.1029/2020gl092092

McCullagh, P., & Nelder, J. A. (1989). Generalized Linear Models (2nd ed.). London: Chapman and Hall.

McGovern, A., Lagerquist, R., Gagne, J. D. II, Jergensen, G. E., Elmore, K. L., Homeyer, C. R., & Smith, T. (2019). Making the black box more transparent: Understanding the physical

implications of machine learning. *Bulletin of the American Meteorological Society*, *100*(11), 2175–2199. https://doi.org/10.1175/BAMS-D-18-0195.1

Michalon, N., Nassif, A., Saouri, T., Royer, J. F., & Pontikis, C. A. (1999). Contribution to the climatological study of lightning. *Geophysical Research Letters*, *26*(20), 3097–3100. https://doi.org/10.1029/1999GL010837

Mo, R., So, R., Brugman, M. M., Mooney, C., Liu, A. Q., Jakob, M., et al. (2021). Column relative humidity and primary condensation rate as two useful supplements to atmospheric river analysis. *Water Resources Research*, *57*(11), e2021WR029678. https://doi.org/10.1029/2021wr029678

Molina, M. J., Gagne, D. J., & Prein, A. F. (2021). A benchmark to test generalization capabilities of deep learning methods to classify severe convective storms in a changing climate. *Earth and Space Science*, *8*(9), e2020EA001490. https://doi.org/10.1029/2020ea001490

Molina, M. J., O'Brien, T. A., Anderson, G., Ashfaq, M., Bennett, K. E., Collins, W. D., et al. (2023). A review of recent and emerging machine learning applications for climate variability and weather phenomena. *Artificial Intelligence for the Earth Systems*, *2*(4), 1-17. https://doi.org/10.1175/aies-d-22-0086.1

Molnar, C., König, G., Herbinger, J., Freiesleben, T., Dandl, S., Scholbeck, C. A., et al. (2022). General pitfalls of model-agnostic interpretation methods for machine learning models. In *xxAI - Beyond Explainable AI* (pp. 39–68). Cham: Springer International Publishing. https://doi.org/10.1007/978-3-031-04083-2_4

Montavon, G., Binder, A., Lapuschkin, S., Samek, W., Müller, K-R. (2019). Layer-wise relevance propagation: An Overview. In *Explainable AI: Interpreting, Explaining and*

Visualizing Deep Learning (pp. 193–209). Cham: Springer International Publishing. https://doi.org/10.1007/978-3-030-28954-6_10

Nag, A. (2014). Recent evolution of the U.S. National Lightning Detection Network. In *Proceedings of the 23rd International Lightning Detection Conference*, Tucson, Arizona, USA.

Nauslar, N., Kaplan, M., Wallmann, J., & Brown, T. (2013). A forecast procedure for dry thunderstorms. *Journal of Operational Meteorology*, *1*(17), 200–214. Retrieved from http://nwafiles.nwas.org/jom/articles/2013/2013-JOM17/2013-JOM17.pdf

Noyelle, R., Zhang, Y., Yiou, P., Faranda, D. (2023). Maximal reachable temperatures for Western Europe in current climate. *Environmental Research Letters*, *18*(9), 094061. https://doi.org/10.1088/1748-9326/acf679

Pedregosa, F., Varoquaux, G., Gramfort, A., Michel, V., Thirion, B., Grisel, O., et al. (2011). Scikit-learn: Machine Learning in Python. *Journal of Machine Learning Research*, *12*, 2825-2830. Retrieved from https://www.jmlr.org/papers/volume12/pedregosa11a/pedregosa11a.pdf

Pérez-Invernón, F. J., Gordillo-Vázquez, F. J., Huntrieser, H., & Jöckel, P. (2023). Variation of lightning-ignited wildfire patterns under climate change. *Nature Communications*, *14*(1), 1-11. https://doi.org/10.1038/s41467-023-36500-5

Price, C., & Rind, D. (1992). A simple lightning parameterization for calculating global lightning distributions. *Journal of Geophysical Research*, *97*(D9), 9919–9933. https://doi.org/10.1029/92JD00719

Price, C., & Rind, D. (1994). Possible implications of global climate change on global lightning distributions and frequencies. *Journal of Geophysical Research*, *99*(D5), 10823-10831. https://doi.org/10.1029/94JD00019

Ren, L., Yang, Y., Wang, H., Wang, P., Yue, X., & Liao, H. (2022). Widespread wildfires over the western United States in 2020 linked to emissions reductions during COVID-19. *Geophysical Research Letters*, *49*(15), e2022GL099308. https://doi.org/10.1029/2022GL099308

Rochette, S. M., Moore, J. T., & Market, P. S. (1999). The importance of parcel choice in elevated CAPE computations. *National Weather Digest*, *23*, 20-32. Retrieved from http://nwafiles.nwas.org/digest/papers/1999/Vol23No4/Pg20-Rochette.pdf

Romps, D. M. (2019). Evaluating the future of lightning in cloud-resolving models. *Geophysical Research Letters*, *46*(24), 14863–14871. https://doi.org/10.1029/2019GL085748

Romps, D. M., Seeley, J. T., Vollaro, D., & Molinari, J. (2014). Projected increase in lightning strikes in the United States due to global warming. *Science*, *346*(6211), 851–854. https://doi.org/10.1126/science.1259100

Rorig, M. L., & Ferguson, S. A. (1999). Characteristics of lightning and wildland fire ignition in the Pacific Northwest. *Journal of Applied Meteorology*, *38*(11), 1565–1575. https://doi.org/10.1175/1520-0450(1999)038<1565:COLAWF>2.0.CO;2

Rorig, M. L., McKay, S. J., Ferguson, S. A., & Werth, P. (2007). Model-generated predictions of dry thunderstorm potential. *Journal of Applied Meteorology and Climatology*, *46*(5), 605–614. https://doi.org/10.1175/JAM2482.1

Rosenthal, N., Benmarhnia, T., Ahmadov, R., James, E., & Marlier, M. E. (2022). Population co-exposure to extreme heat and wildfire smoke pollution in California during 2020.

Environmental Research: Climate, *1*(2), 025004. https://doi.org/10.1088/2752-5295/ac860e

Rudin, C. (2019). Stop explaining black box machine learning models for high stakes decisions and use interpretable models instead. *Nature Machine Intelligence*, *1*(5), 206–215.

Shrikumar, A., Greenside, P., Shcherbina, A., & Kundaje, A. (2016). Not Just a Black Box: Learning Important Features Through Propagating Activation Differences. *arXiv [cs.LG]*. Retrieved from https://arxiv.org/abs/1605.01713

Sixt, L., Granz, M., & Landgraf, T. (2019). When explanations lie: Why many modified BP attributions fail. *arXiv [cs.LG]*. Retrieved from http://arxiv.org/abs/1912.09818

Stoll, P. J., Graversen, R. G., & Messori, G. (2023). The global atmospheric energy transport analysed by a wavelength-based scale separation. *Weather and Climate Dynamics*, *4*(1), 1–17. https://doi.org/10.5194/wcd-4-1-2023

Stolz, D. C., Rutledge, S. A., Pierce, J. P., & van den Heever, S. C. (2017). A global lightning parameterization based on statistical relationships among environmental factors, aerosols, and convective clouds in the TRMM climatology. *Journal of Geophysical Research Atmospheres*, *122*(14), 7461-7492. https://doi.org/10.1002/2016JD026220

Taszarek, M., Brooks, H. E., Czernecki, B., Szuster, P., & Fortuniak, K. (2018). Climatological Aspects of Convective Parameters over Europe: A Comparison of ERA-Interim and Sounding Data. *Journal of Climate*, *31*(11), 4281-4308. https://doi.org/10.1175/JCLI-D-17-0596.1

Toms, B. A., Barnes, E. A., & Ebert-Uphoff, I. (2020). Physically interpretable neural networks for the geosciences: Applications to earth system variability. *Journal of Advances in Modeling Earth Systems*, *12*(9), e2019MS002002. https://doi.org/10.1029/2019ms002002

Tost, H., Jöckel, P., Lelieveld, J. (2007). Lightning and convection parameterisations – uncertainties in global modelling. *Atmospheric Chemistry and Physics*, *7*(17), 4553-4568. https://doi.org/10.5194/acp-7-4553-2007

Trok, J. T., Davenport, F. V., Barnes, E. A., & Diffenbaugh, N. S. (2023). Using machine learning with partial dependence analysis to investigate coupling between soil moisture and near-surface temperature. *Journal of Geophysical Research Atmospheres*, *128*(12), e2022JD038365. https://doi.org/10.1029/2022jd038365

Veraverbeke, S., Rogers, B. M., Goulden, M. L., Jandt, R. R., Miller, C. E., Wiggins, E. B., & Randerson, J. T. (2017). Lightning as a major driver of recent large fire years in North American boreal forests. *Nature Climate Change*, *7*(7), 529–534. https://doi.org/10.1038/NCLIMATE3329

van Wagtendonk, J. W., & Cayan, D. R. (2008). Temporal and spatial distribution of lightning strikes in California in relation to large-scale weather patterns. *Fire Ecology*, *4*(1), 34–56. https://doi.org/10.4996/fireecology.0401034

Werth, P., & Ochoa, R. (1993). The evaluation of Idaho wildfire growth using the Haines Index. *Weather and Forecasting*, *8*(2), 223-234. https://doi.org/10.1175/1520-0434(1993)008<0223:teoiwg>2.0.co;2

Wolding, B., Dias, J., Kiladis, G., Ahmed, F., Powell, S. W., Maloney, E., & Branson, M. (2020). Interactions between moisture and tropical convection. Part I: The coevolution of moisture and convection. *Journal of the Atmospheric Sciences*, *77*(5), 1783–1799. https://doi.org/10.1175/JAS-D-19-0225.1

Yoshida, S., Morimoto, T., Ushio, T., & Kawasaki, Z. (2009). A fifth-power relationship for lightning activity from Tropical Rainfall Measuring Mission satellite observations. *Journal of Geophysical Research*, *114*(D9), 1-10. https://doi.org/10.1029/2008jd010370

Zhang, Y., & Boos, W. R. (2023). An upper bound for extreme temperatures over midlatitude land. *Proceedings of the National Academy of Sciences of the United States of America*, *120*(12), e2215278120. https://doi.org/10.1073/pnas.2215278120

Zhou, X., Josey, K., Kamareddine, L., Caine, M. C., Liu, T., Mickley, L. J., et al. (2021). Excess of COVID-19 cases and deaths due to fine particulate matter exposure during the 2020 wildfires in the United States. *Science Advances*, *7*(33), eabi8789. https://doi.org/10.1126/sciadv.abi8789

References from the Supporting Information

Belkin, M., Hsu, D., Ma, S., & Mandal, S. (2019). Reconciling modern machine-learning practice and the classical bias-variance trade-off. *Proceedings of the National Academy of Sciences of the United States of America*, *116*(32), 15849–15854. https://doi.org/10.1073/pnas.1903070116

Dagon, K., Sanderson, B. M., Fisher, R. A., & Lawrence, D. M. (2020). A machine learning approach to emulation and biophysical parameter estimation with the Community Land Model, version 5. *Advances in Statistical Climatology, Meteorology and Oceanography*, *6*(2), 223–244. https://doi.org/10.5194/ascmo-6-223-2020

Srivastava, N., Hinton, G., Krizhevsky, A., Sutskever, I., & Salakhutdinov, R. (2014). Dropout: A simple way to prevent neural networks from overfitting. *Journal of Machine Learning*

Research, *15*, 1929-1958. Retrieved from

https://jmlr.org/papers/volume15/srivastava14a/srivastava14a.pdf

CHAPTER SIX: SUMMARY

This dissertation consists of four studies, and they are presented in the second through fifth chapters. In the second chapter, I examine the spatiotemporal characteristics of $PM_{2.5}$/ozone co-occurrences and associated population exposure in the western U.S. (WUS). My results show that the frequency, spatial extent, and temporal persistence of extreme $PM_{2.5}$/ozone co-occurrences have increased significantly between 2001-2020, increasing annual population exposure to multiple harmful air pollutants by ~25 million person-days/year. Using a clustering methodology to characterize daily weather patterns, I identify significant increases in atmospheric ridging patterns conducive to widespread $PM_{2.5}$/ozone co-occurrences and population exposure. I further link the spatial extent of co-occurrence to the extent of extreme heat and wildfires. My results suggest an increasing potential for co-occurring air pollution episodes in the WUS with continued climate change.

In the third chapter, I characterize the climatology of dry lightning and the associated meteorological conditions in central and northern California during the warm season (May-October) when wildfire risk is highest. Across this domain, nearly half (~46%) of all cloud-to-ground lightning flashes occurred as dry lightning during the study period. I find that higher elevations (>2000m) receive more dry lightning compared to lower elevations (<1000m) with activity concentrated in July-August. Although local meteorological conditions show substantial spatial variation, I find regionwide enhancements in mid-tropospheric moisture and instability on dry lightning days relative to background climatology. Additionally, surface temperatures, lower-tropospheric dryness, and mid-tropospheric instability are increased across the region on dry versus wet lightning days. I also identify widespread dry lightning outbreaks in the historical record, quantify their seasonality and spatial extent, and analyze associated large-scale

atmospheric patterns. Three of these four atmospheric patterns are characterized by different configurations of ridging over the continental interior and offshore troughing. Understanding the meteorology of dry lightning across this region can inform forecasting of possible wildfire ignitions and is relevant for assessing changes in dry lightning and wildfire risk in climate projections.

In the fourth chapter, I combine wildfire, lightning and precipitation datasets to quantify ignition precipitation amounts associated with lightning-ignited wildfires across ecoprovinces of the WUS. The median precipitation for all lightning-ignited wildfires is 2.8mm but varies with vegetation and fire characteristics. “Holdover” fires not detected until 2-5 days following ignition occur with significantly higher precipitation (5.1mm) compared to fires detected promptly after ignition (2.5mm), and with cooler and wetter environmental conditions. Further, I find substantial variation in precipitation associated with promptly-detected (1.7-4.6mm) and holdover (3.0-7.7mm) fires across ecoprovinces. Consequently, my results show that the widely-used 2.5mm threshold for defining dry lightning does not fully capture lightning ignition risk, and incorporating ecoprovince-specific precipitation amounts would better inform WUS wildfire prediction and management.

In the fifth chapter, I build and train Convolutional Neural Networks (CNNs) to predict the occurrence of cloud-to-ground lightning across the WUS during June-September from the spatial patterns of seven large-scale meteorological variables from reanalysis (1995-2022). Individually-trained CNN models at each 1° x 1° grid cell (n = 285 CNNs) show high skill at predicting lightning days across the WUS and perform best in parts of the interior Southwest where summertime lightning is most common. Further, interannual correlation between observed and predicted lightning days is high (median r = 0.87), demonstrating that locally-trained CNNs

realistically capture year-to-year variation in lightning activity across the WUS. I then use an "eXplainable Artificial Intelligence" (XAI) technique called Layer-wise Relevance Propagation (LRP) to investigate the relevance of predictor variables to successful lightning prediction in each grid cell. Using maximum LRP values, my results show that two thermodynamic variables - ratio of surface moist static energy to free-tropospheric saturation moist static energy, and the 700-500 hPa lapse rate - are the most relevant lightning predictors for 96% of CNNs. As lightning is not directly simulated by global climate models, these CNNs could be used to parameterize lightning in climate models to assess changes in future lightning occurrence with projected climate change. Understanding changes in lightning risk and consequently lightning-caused wildfire risk across the WUS could inform fire management, planning, and disaster preparedness.

Since lightning is a major source of WUS wildfire ignition, my dissertation aimed to advance our understanding of dry lightning in the WUS and its associated meteorological conditions, wildfire ignitions, air quality impacts, and future projections. In doing so, I attempted to address multiple grand challenges related to lightning and wildfire research specifically as they pertain to the WUS region. These challenges include the quantification of ignition-relevant precipitation amounts that are useful for short-term forecasting of lightning-caused wildfire risk, the parameterization of lightning which can be used to project future lightning occurrence using global climate models, and the examination of dry lightning meteorology over fire-prone areas of California that can be useful for both operational forecasting and future projections. Finally, I showed how increasing wildfire activity is linked to the increasing co-occurrence of multiple harmful air pollutants, which can inform societal adaptation strategies to a future with more wildfires.

APPENDIX

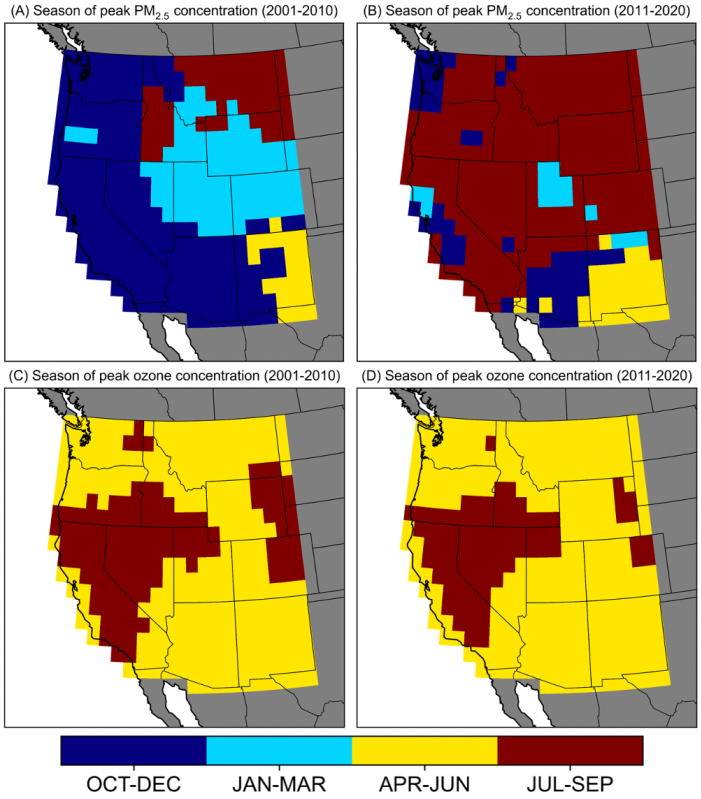

Fig. S1. Peak seasons of mean $PM_{2.5}$ and ozone concentrations. Seasons of peak average concentrations of $PM_{2.5}$ (top) and ozone (bottom) during 2001-2010 (left) and 2011-2020 (right) at each grid cell.

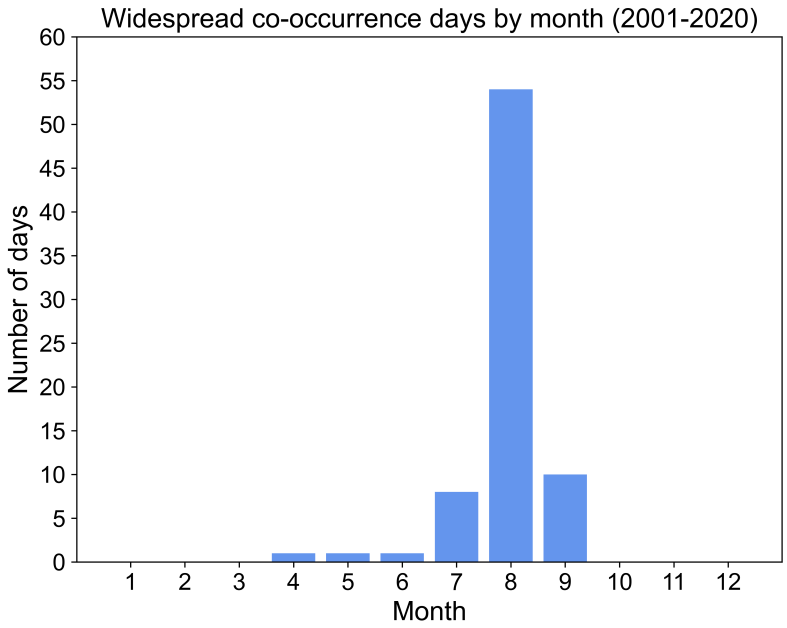

Fig. S2. Seasonality of widespread co-occurrence days. Total number of widespread $PM_{2.5}$/ozone co-occurrence days (≥25% of the western US) during each calendar month, 2001-2020.

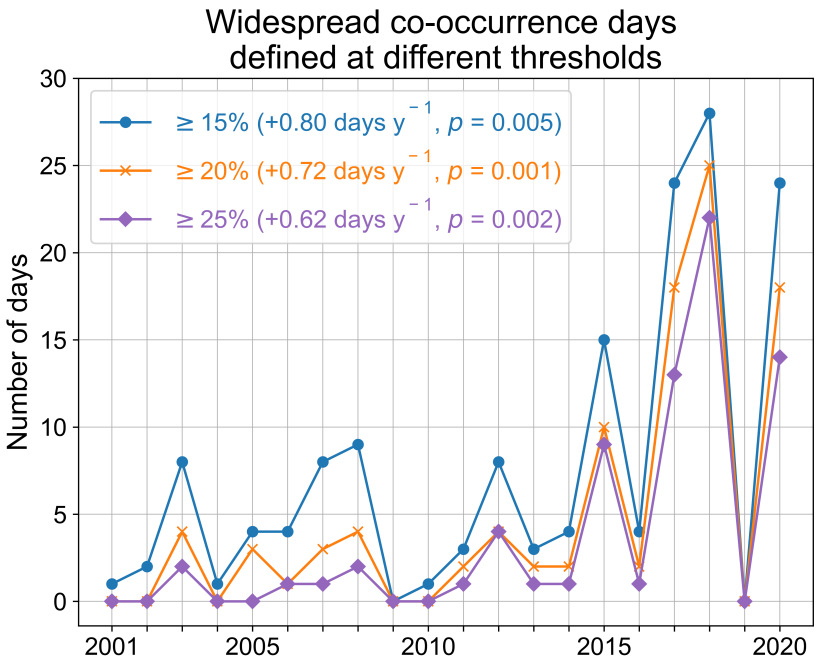

Fig. S3. Widespread $PM_{2.5}$/ozone co-occurrence days during July-September at different thresholds. Days with simultaneous local $PM_{2.5}$/ozone co-occurrences affecting ≥15% (green), ≥20% (brown), and ≥25% (blue) of western US grid cells, 2001-2020. Text indicates annual linear trends and *p*-values based on a non-parametric permutation test.

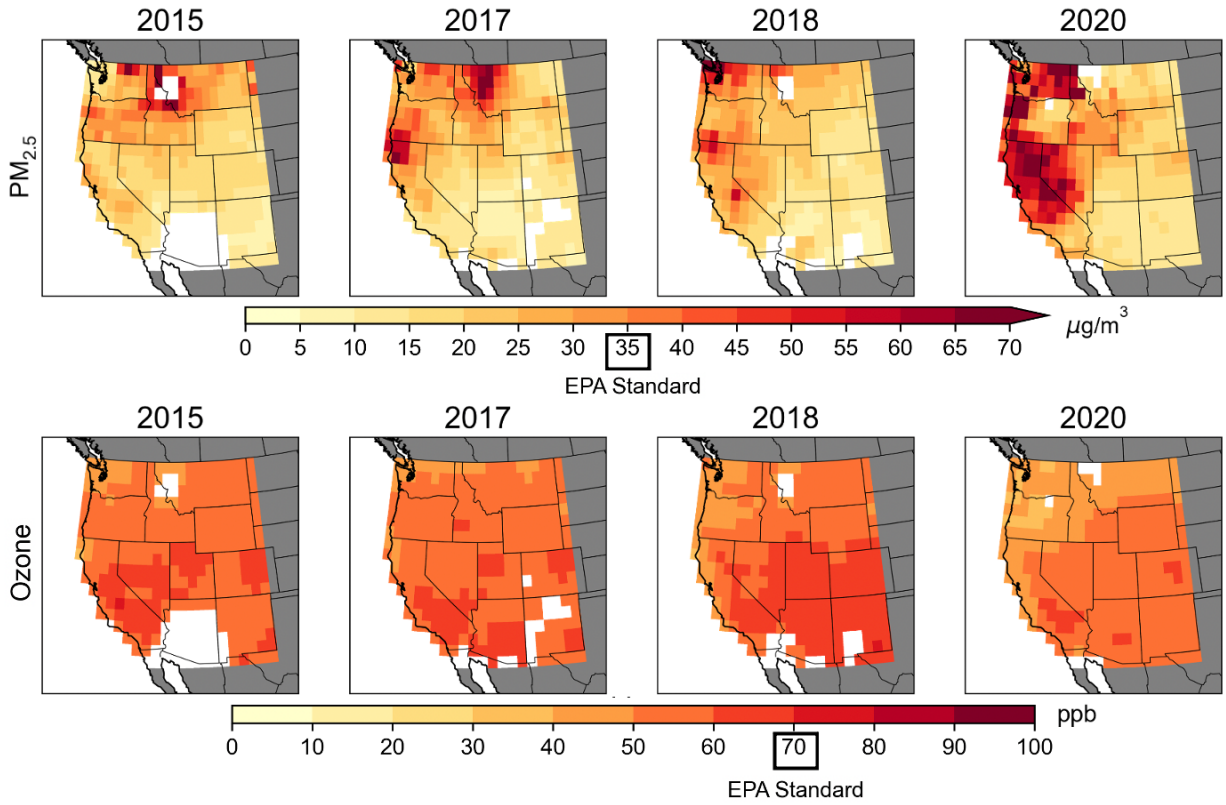

Fig. S4. $PM_{2.5}$ and ozone concentrations on co-occurrence days. Average concentrations of $PM_{2.5}$ (top row) and MDA8 ozone (bottom row) on all local co-occurrence days during July-September of 2015, 2017, 2018, and 2020. Corresponding EPA regulatory health standards are 35 μg/m^3 for $PM_{2.5}$ and 70 ppb for ozone. White shading indicates that no co-occurrence days were recorded in those grid cells during July-September of that year.

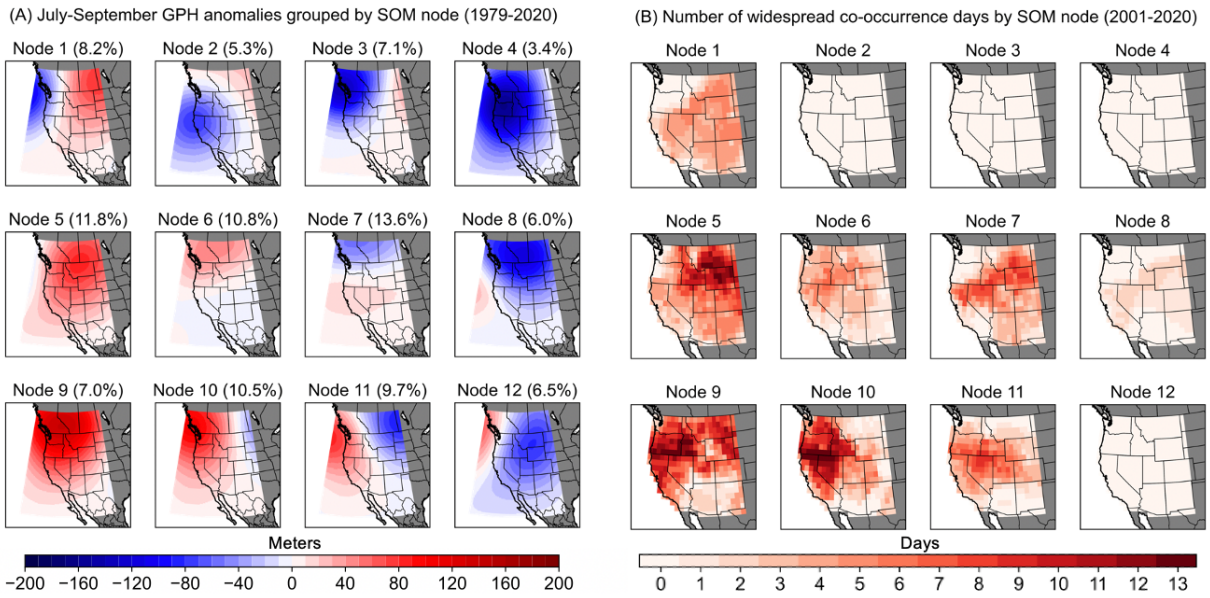

Fig. S5. All 12 nodes of the Self-Organizing Map (SOM). (**A**) Geopotential height (GPH) anomalies for each SOM node trained over 1979-2020. (**B**) Number of widespread $PM_{2.5}$/ozone co-occurrence days (2001-2020) associated with each node. Values in parentheses in plot (**A**) indicate the frequency of each SOM node relative to all July-September days during the period of overlap with air pollution data (2001-2020).

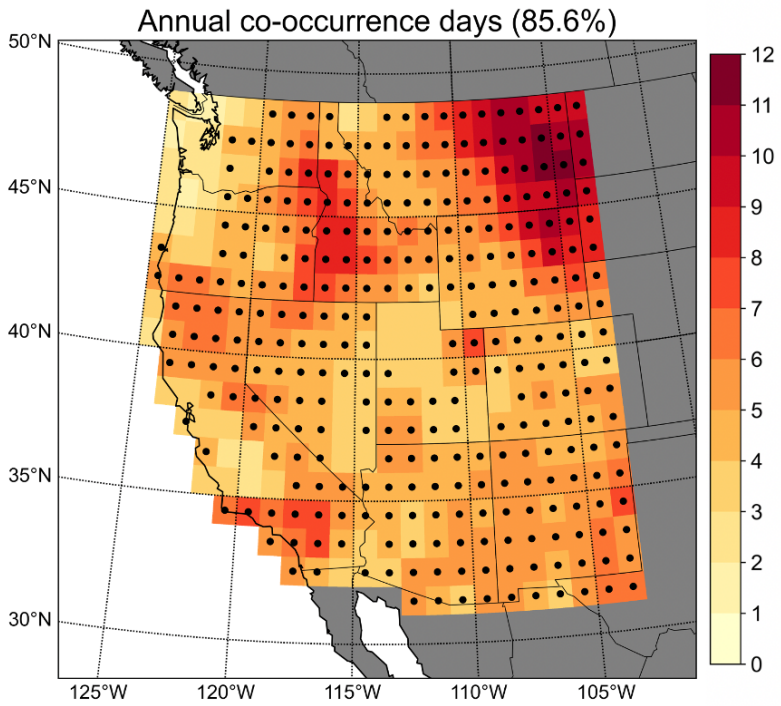

Fig. S6. Annual frequency of co-occurrence days. Average number of local annual $PM_{2.5}$/ozone co-occurrence days at each grid cell. Black dots denote grid cells averaging more than 3.65 days/year, the number expected by random chance from a joint probability distribution. Value in parentheses indicates the percentage of western US grid cells averaging more co-occurrence days than expected by random chance.

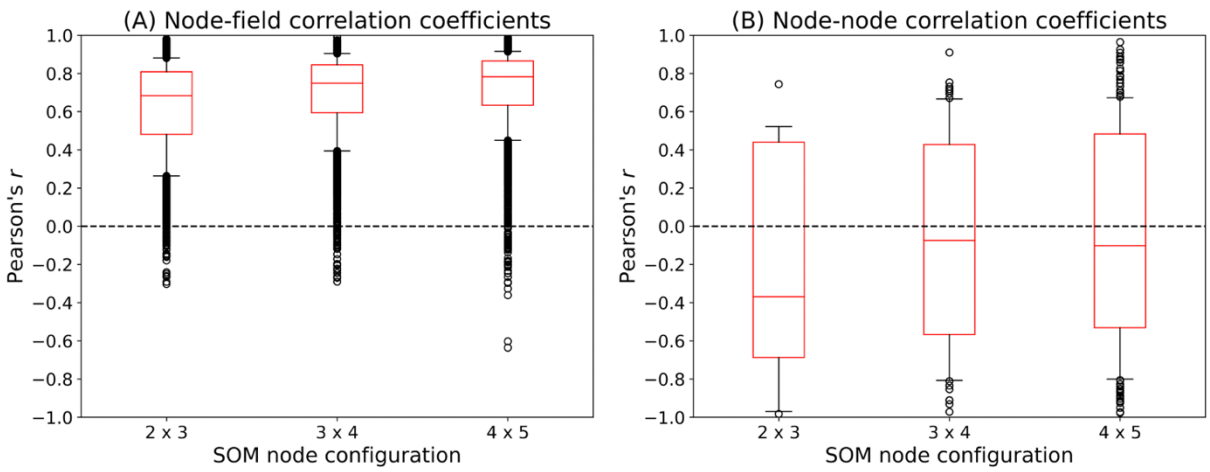

Fig. S7. Spatial correlation coefficients for three SOM node configurations. Correlation coefficients (**A**) between each SOM node pattern and the individual constituent patterns in that node, and (**B**) between every unique combination of node pairs. Higher correlation coefficients in plot (**A**) indicate that individual days are well-represented by the node pattern into which they are assigned, and in plot (**B**) indicate greater redundancy of nodes in the SOM.

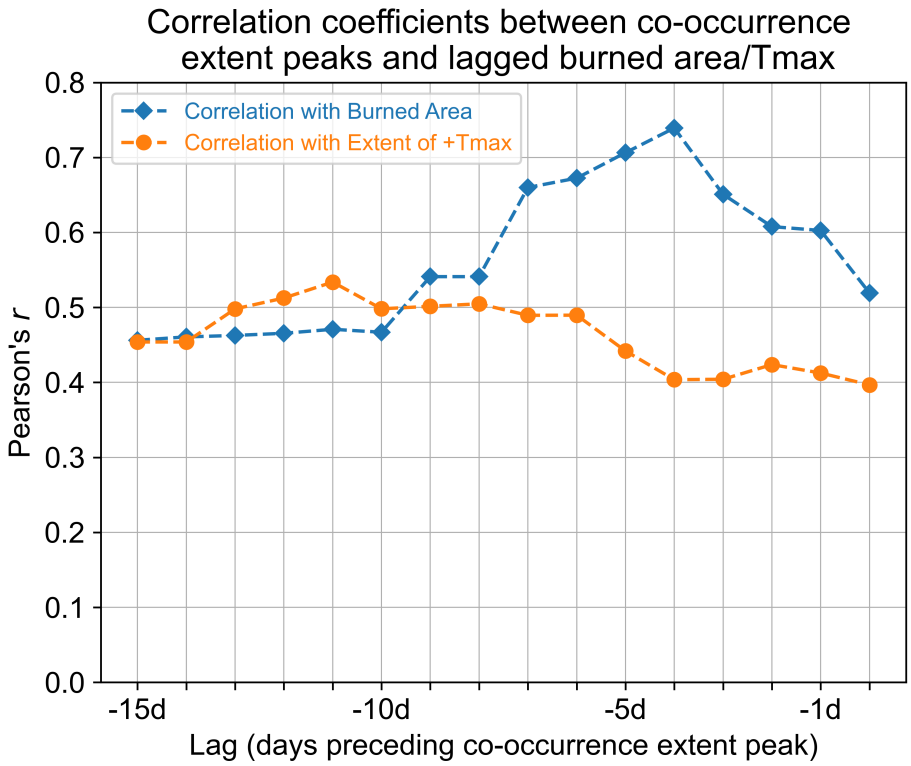

Fig. S8. Lagged relationship widespread co-occurrences, burned area, and maximum temperatures. 7-day lagged correlation coefficients between temporally independent peaks in widespread $PM_{2.5}$/ozone co-occurrence spatial extent (≥25% of western US, n = 21) and peaks in daily burned area in the western US and southwest Canada (blue dashes), and between peaks in widespread co-occurrence extent and peaks in the extent of positive maximum temperature (+Tmax) anomalies >1 standard deviation above local daily climatologies in the western US (orange dashes) for all lags between 0-15 days preceding $PM_{2.5}$/ozone co-occurrence.

Table S1. Top 15 days with the largest extent of local $PM_{2.5}$/ozone co-occurrences in the western US (2001-2020).

Rank	Date	Percent of western US grid cells	Population exposed, in millions
1	2020-08-24	68.5	36.7
2	2020-08-22	67.5	42.6
3	2020-08-25	66.4	27.9
4	2020-08-21	66.1	46.3
5	2020-08-23	64.3	36.7
6	2018-08-02	56.0	19.7
7	2018-08-01	54.4	20.4
8	2018-08-10	53.9	19.5
9	2018-08-09	51.7	35.5
10	2020-08-26	50.9	22.0
11	2015-08-20	50.7	30.1
12	2020-08-20	50.1	41.3
13	2017-09-02	46.9	42.4
14	2015-08-21	46.9	25.8
15	2018-08-08	46.1	34.7

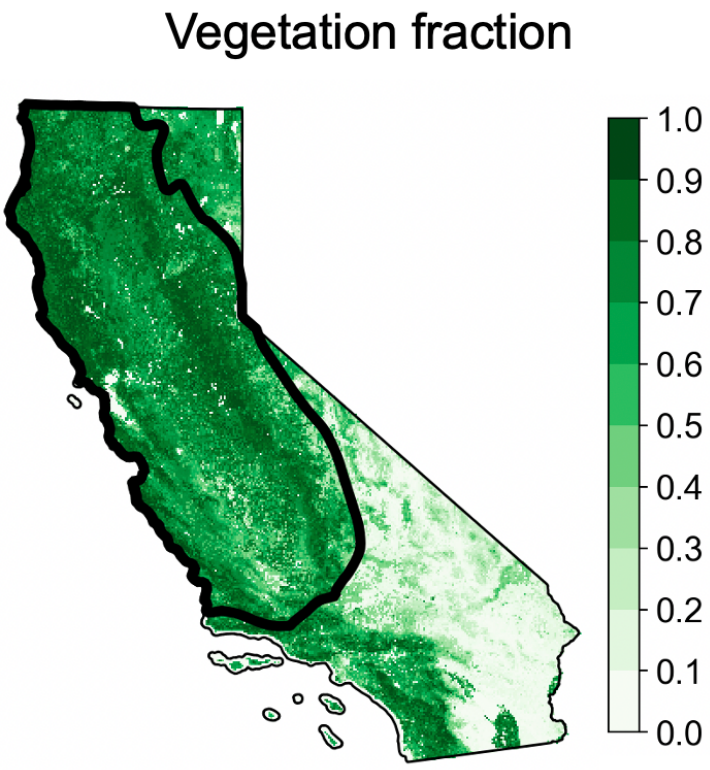

Figure S.1. Vegetation fraction from the Moderate Resolution Imaging Spectroradiometer at each 250m grid cell.

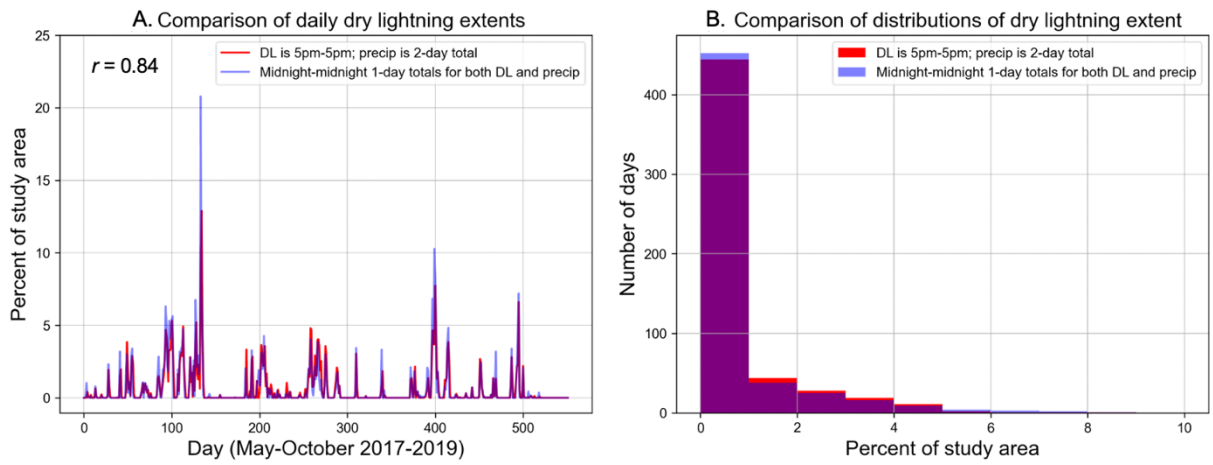

Figure S.2. Comparison of dry lightning (DL) spatial extent using dry lightning data binned from 5 PM-5PM and 2-day precipitation (red) with dry lightning data binned from midnight-midnight and 1-day precipitation (blue). The (A) time series and (B) histograms of daily DL extent are shown for all days (n = 552). Pearson's correlation (r) is shown in (A) and is significant at $P < 0.05$.

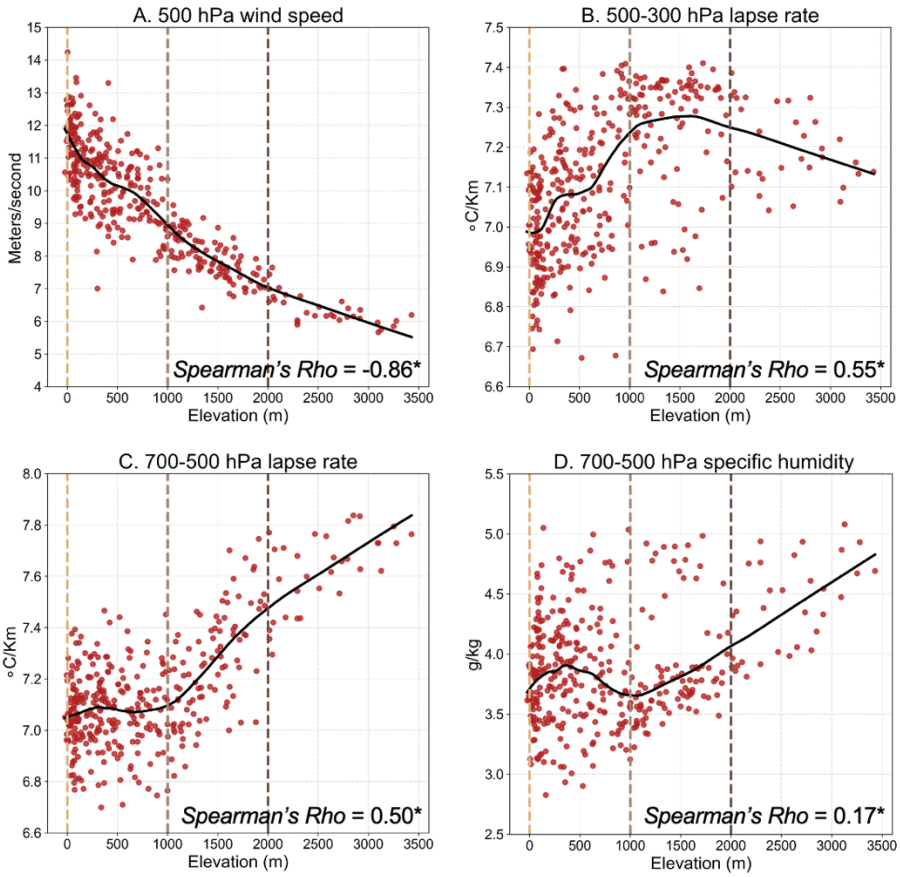

Figure S.3. Scatter plots of surface elevation and select meteorological variables on dry lightning days for each 0.25° ERA5 grid cell in the domain. Vertical dashes denote elevation zones as in figure 2. LOWESS curves are shown for each pairwise relationship. Text indicates Spearman's rank correlation with asterisks denoting significant ($P < 0.05$) relationships.

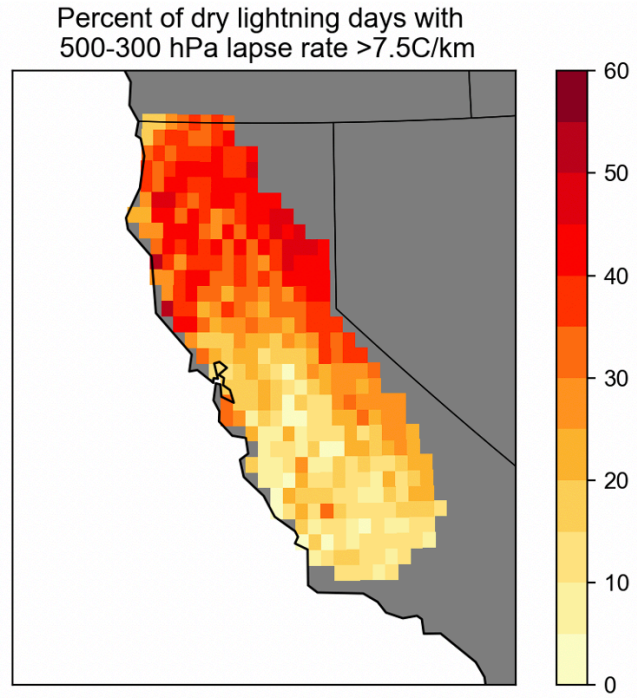

Figure S.4. Percent of dry lightning days at each 0.25° ERA5 grid cell with 500-300 hPa lapse rates (UTLR) of >7.5°C km^{-1} over May-October 1987-2020.

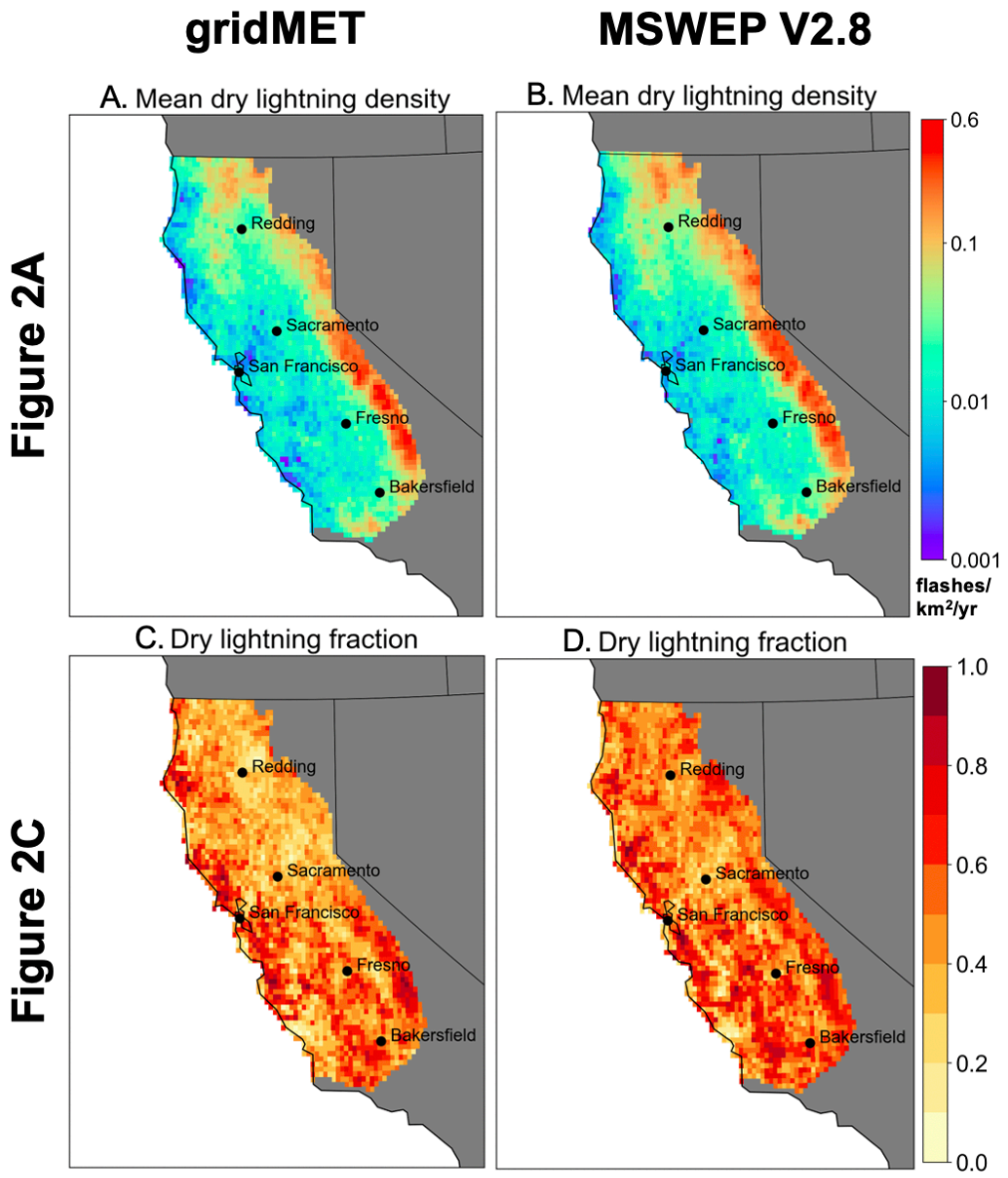

Figure S.5. Comparison of figures 2(A) (top) and 2(C) (bottom) when dry lightning is defined using precipitation from gridMET (left) and the Multi-Source Weighted-Ensemble Precipitation (MSWEP) V2.8 (right) datasets.

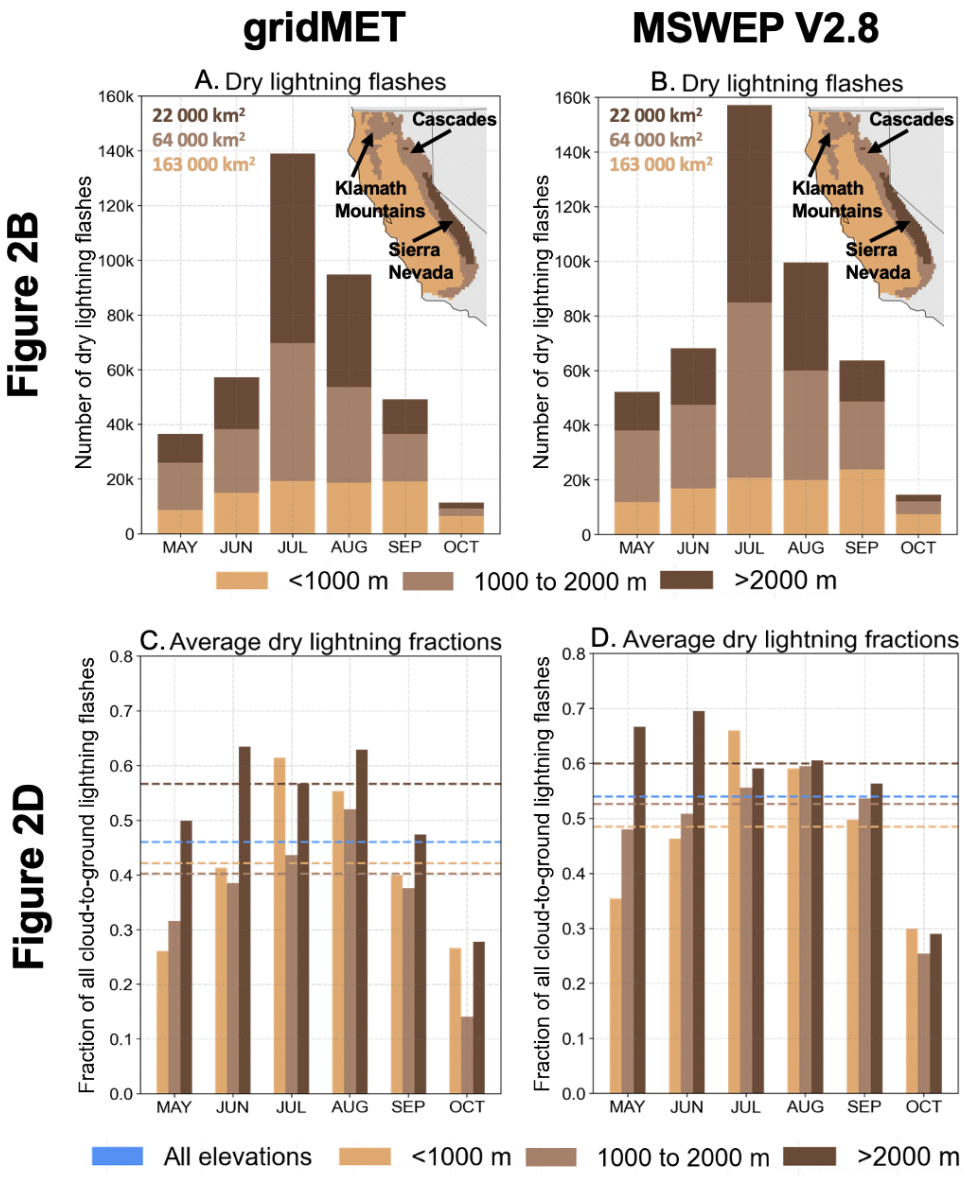

Figure 2B

Figure 2D

Figure S.6. As in figure S.4, but comparing figures 2(B) and 2(D).

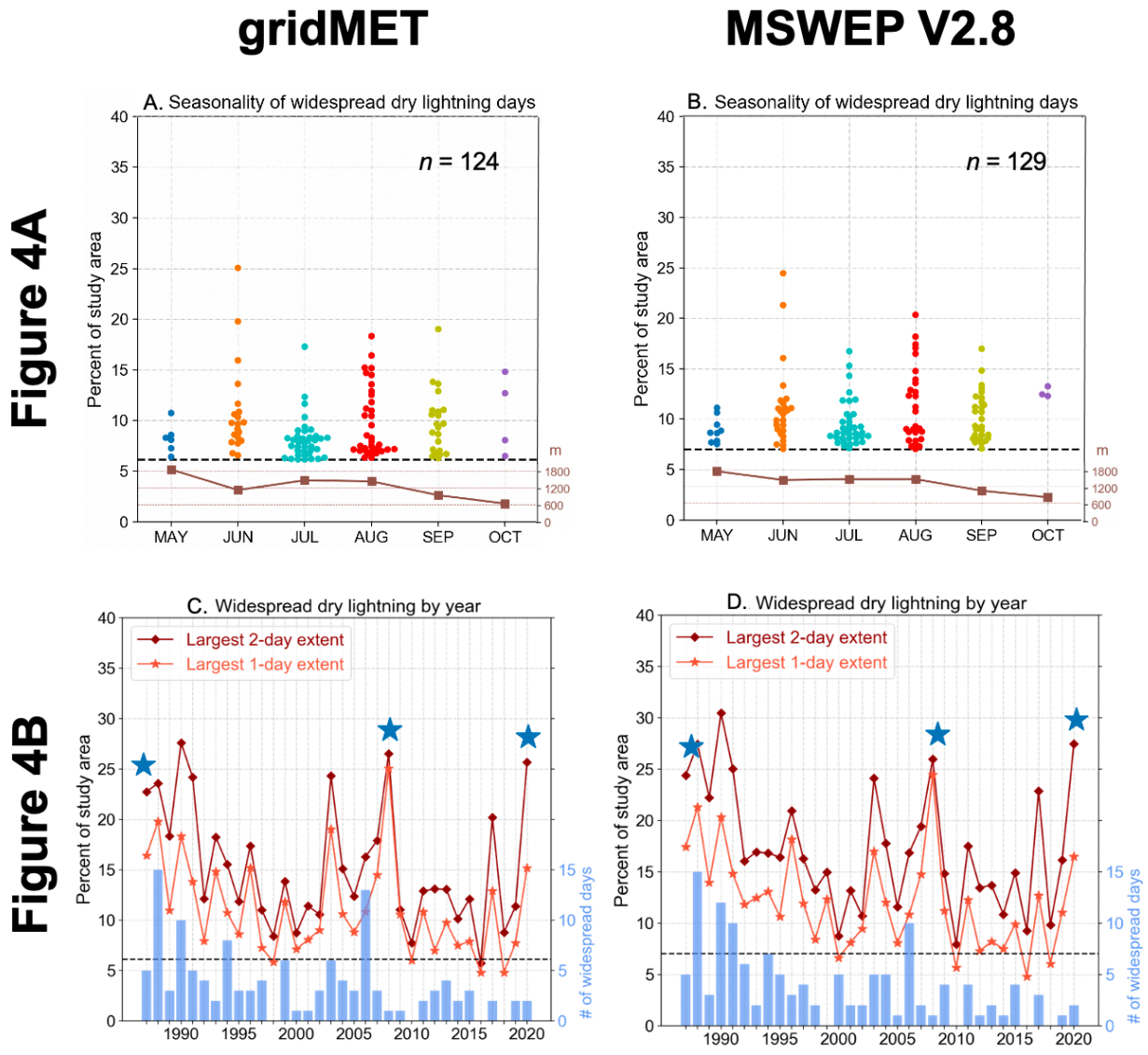

Figure S.7. As in figures S.4 and S.5, but comparing figures 4(A) and 4(B).

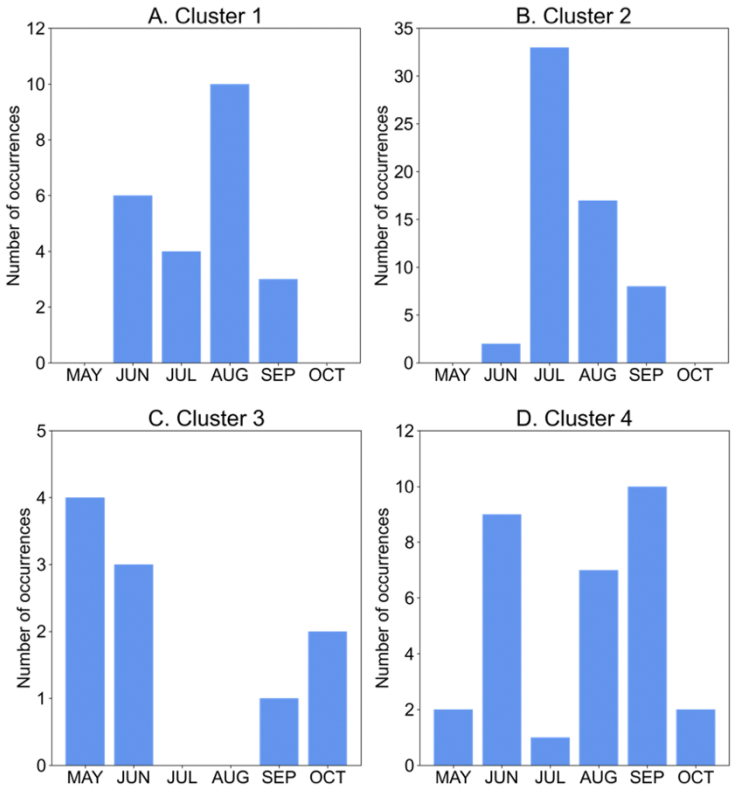

Figure S.8. Monthly occurrences of each *k*-means cluster during May-October 1987-2020. Clusters are the same as in Figure 5.

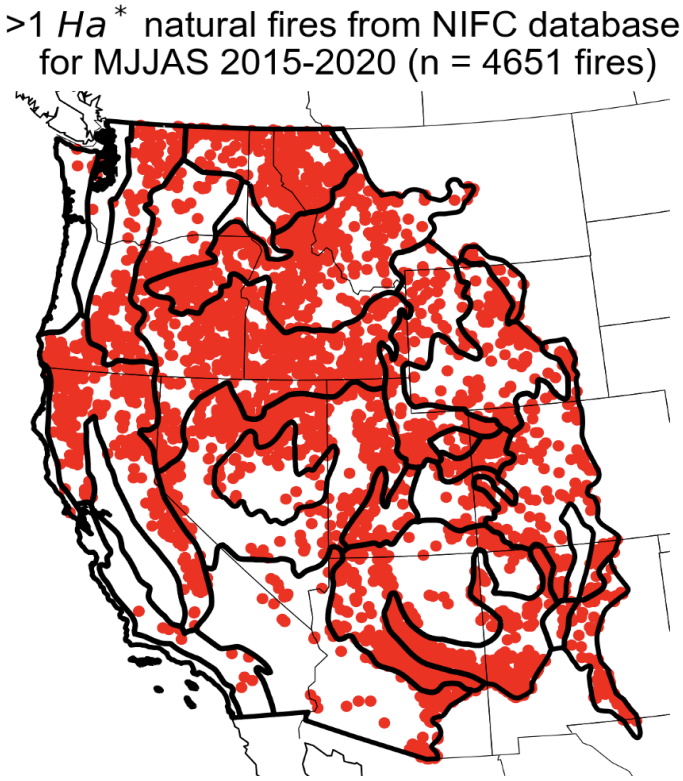

Figure S1. Locations of all naturally-caused wildfires (red dots) from the National Interagency Fire Center database (May-September [MJJAS], 2015-2020) that were matched to cloud-to-ground lightning using spatiotemporal search criteria. Only fires with final burned areas >1 ha are included. Thick black outlines denote Bailey's Ecoprovince boundaries.

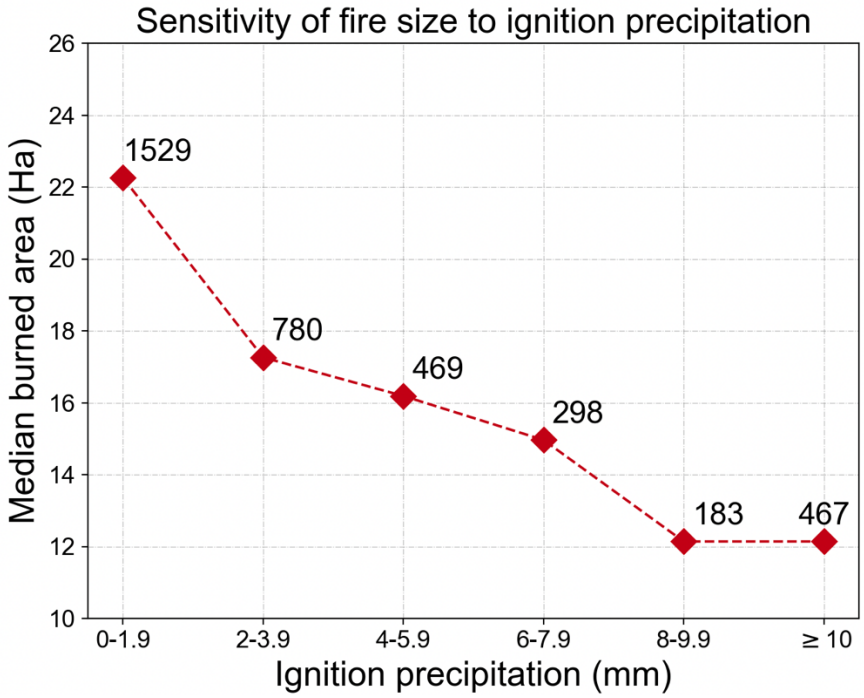

Figure S2. Median burned area of all WUS LIWs binned by ignition precipitation amounts. Text accompanying datapoints shows number of LIWs in each bin.

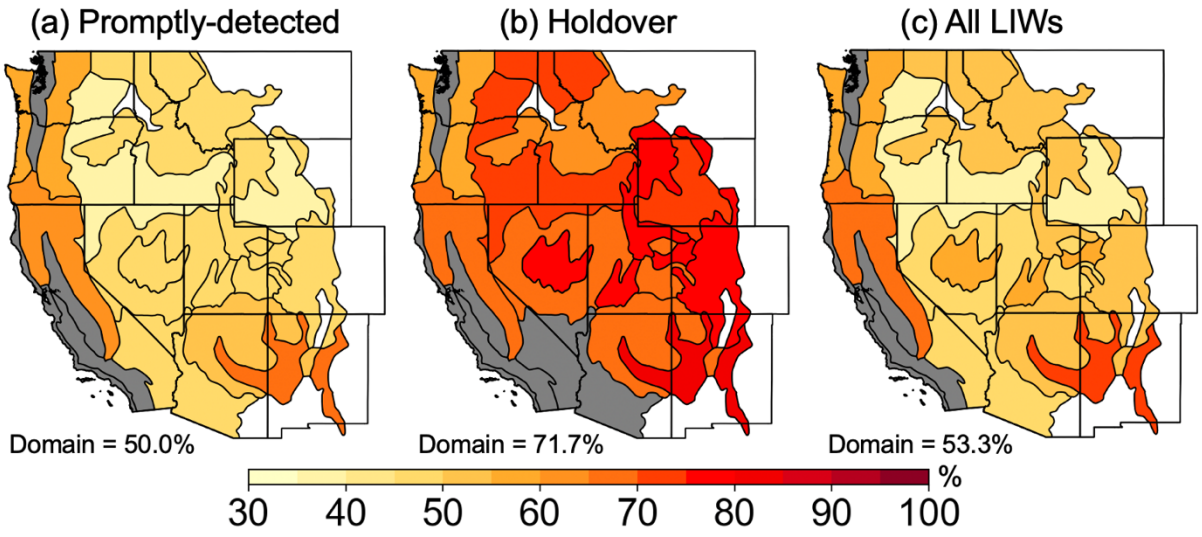

Figure S3. Percentage of LIWs occurring with ≥2.5mm median ignition precipitation in ecoprovinces for (a) promptly-detected, (b) holdover, and (c) all LIWs. Text below maps indicates domain-aggregated percentages. Ecoprovinces shaded in gray were not considered due to low sample sizes of LIWs.

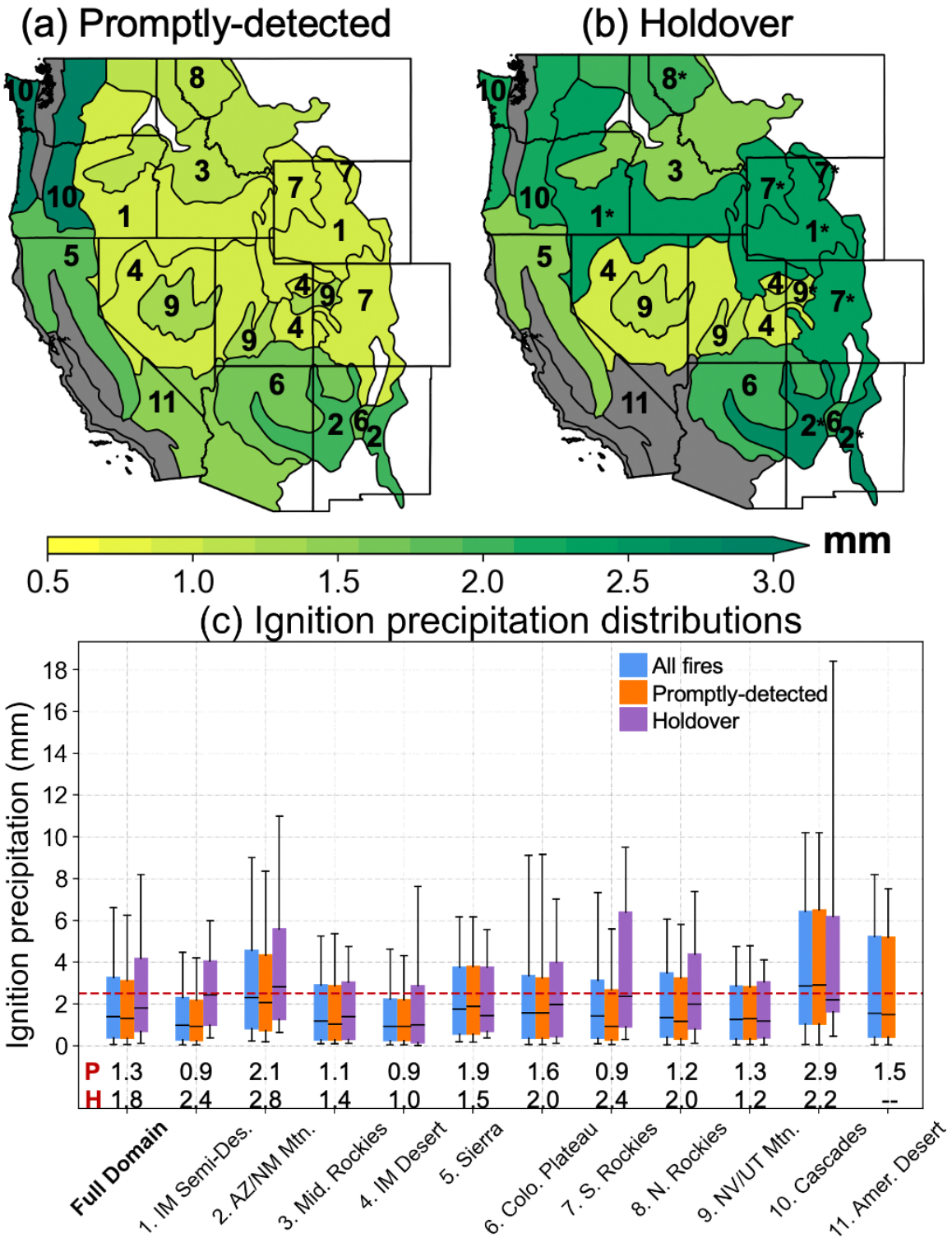

Figure S4. Ignition precipitation amounts as in Figure 2a-c, but using IMERG precipitation instead of MRMS.

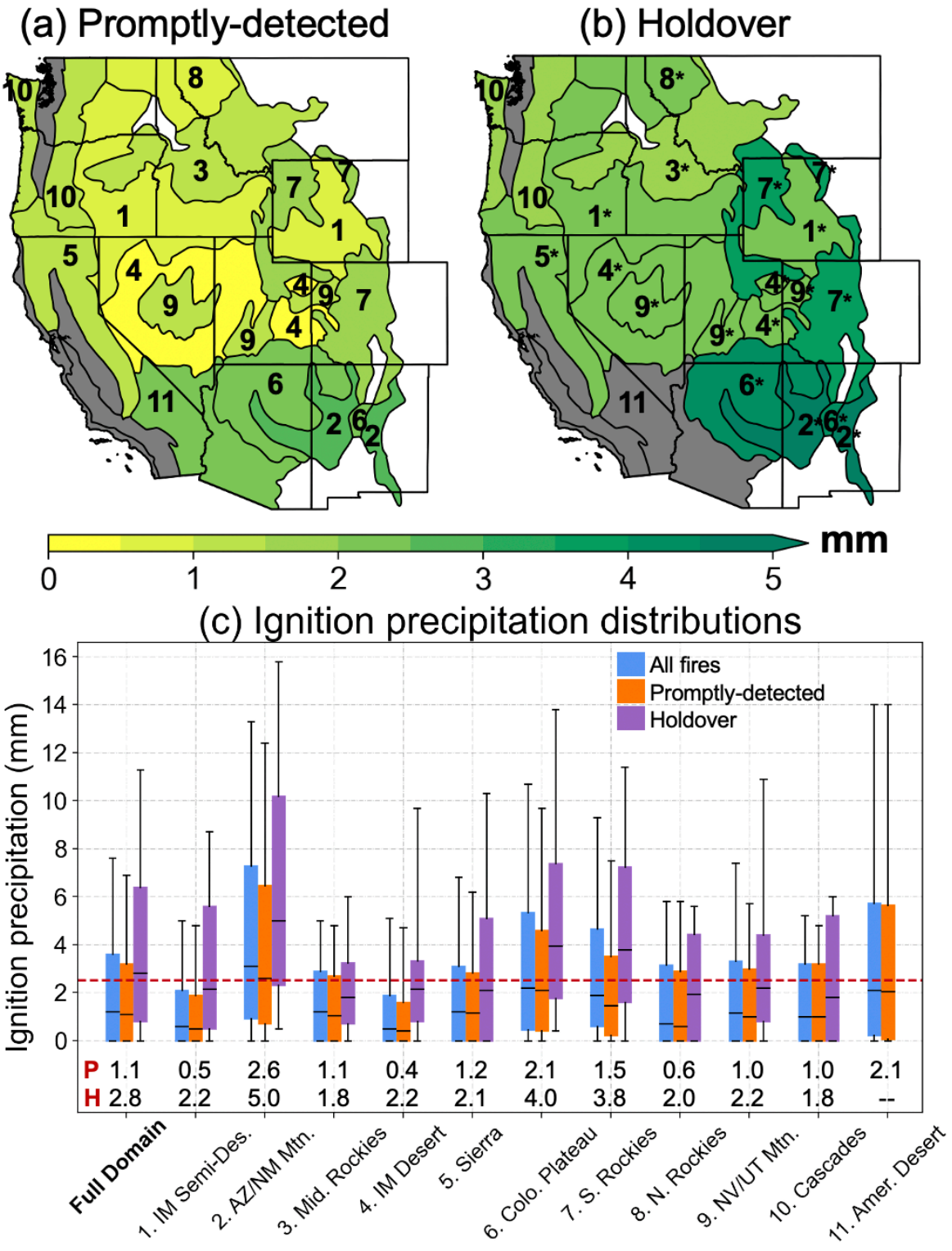

Figure S5. Ignition precipitation amounts as in Figure 2a-c, but using gridMET precipitation instead of MRMS.

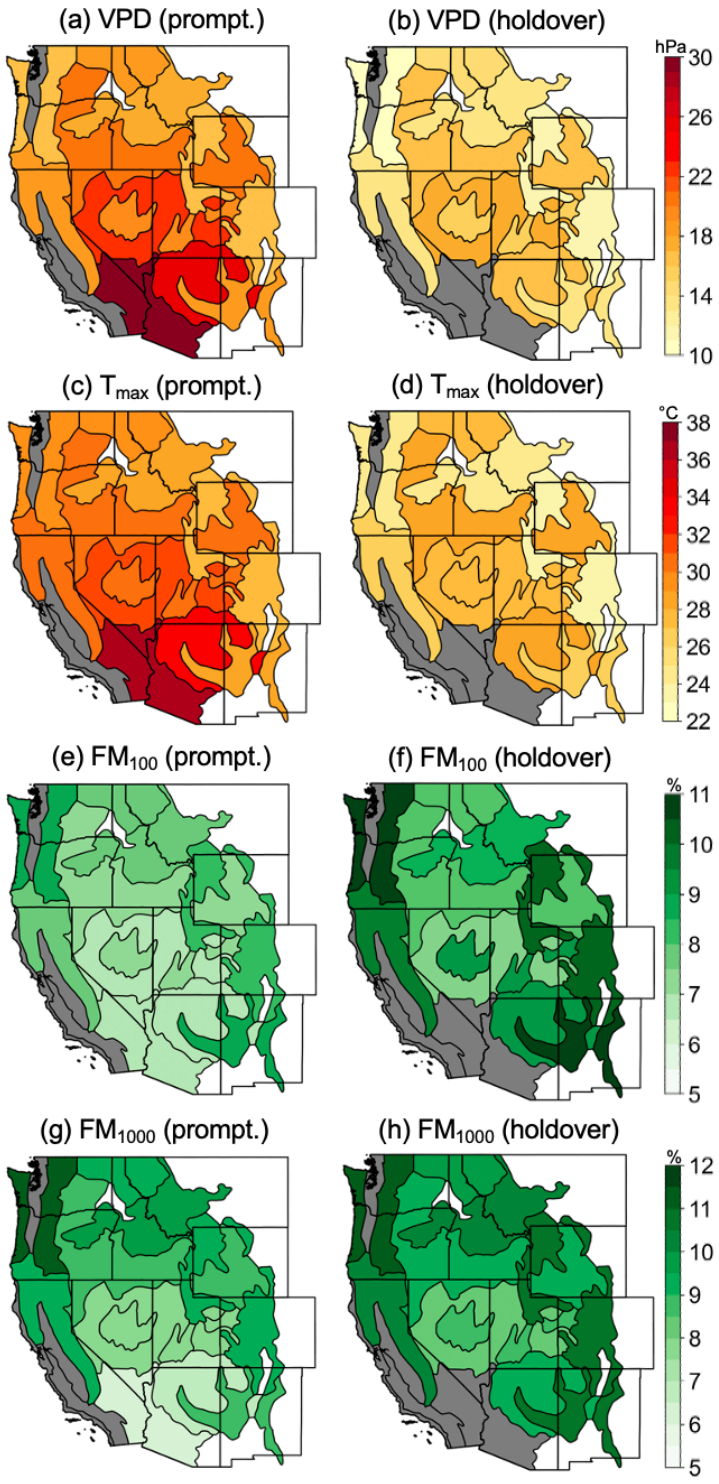

Figure S6. As in Figure 4, but showing actual values during promptly-detected (left column) and holdover (right column) LIWs. Ecoprovinces shaded in gray were not considered due to low sample sizes of LIWs.

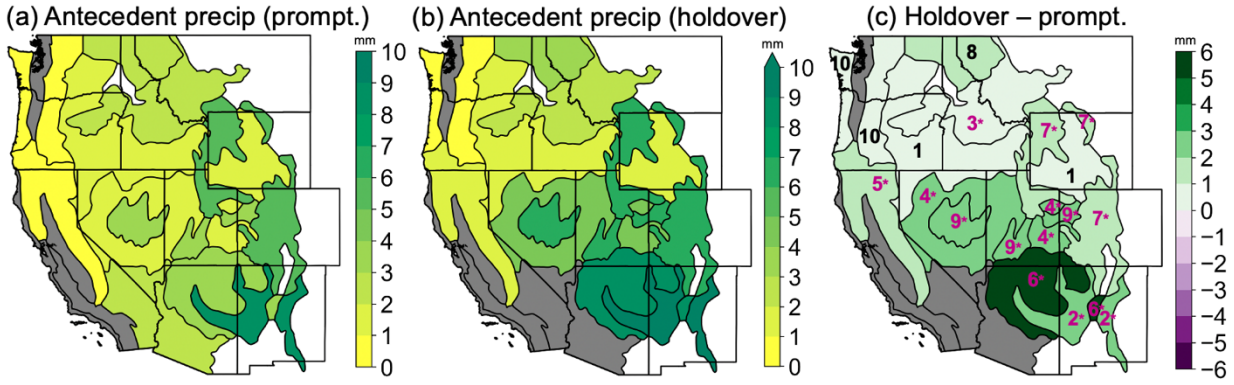

Figure S7. Median accumulated precipitation over the seven days preceding (a) promptly-detected, and (b) holdover LIWs, and (c) their differences across ecoprovinces. Fuchsia numbers with asterisks in (c) indicate statistically significant difference ($P < 0.10$) between the promptly-detected and holdover distributions based on the Mann-Whitney U test. Ecoprovinces shaded in gray were not considered due to low sample sizes of LIWs.

Abbreviated Ecoprovince Name	Full Ecoprovince Name
1 – IM Semi-Desert	Intermountain Semi-Desert
2 – AZ/NM Mountains	Arizona-New Mexico Mountains Semi-Desert-Open Woodland-Coniferous Forest-Alpine Meadow
3 – Middle Rockies	Middle Rocky Mountain Steppe-Coniferous Forest-Alpine Meadow
4 – IM Desert	Intermountain Semi-Desert and Desert
5 – Sierra	Sierran Steppe-Mixed Forest-Coniferous Forest-Alpine Meadow
6 – CO Plateau	Colorado Plateau Semi-Desert
7 – Southern Rockies	Southern Rocky Mountain Steppe-Open Woodland-Coniferous Forest-Alpine Meadow
8 – Northern Rockies	Northern Rocky Mountain Forest-Steppe-Coniferous Forest-Alpine Meadow
9 – NV/UT Mountains	Nevada-Utah Mountains-Semi-Desert-Coniferous Forest-Alpine Meadow
10 – Cascades	Cascade Mixed Forest-Coniferous Forest-Alpine Meadow
11 – American Desert	American Semi-Desert and Desert
12 – CA Coast Range	California Coastal Range Open Woodland-Shrub-Coniferous Forest-Meadow
13 – North CA Coast	Northern California Coast
14 – Pacific Lowlands	Pacific Lowland Mixed Forest
15 – CA Coast	California Coastal Chapparral Forest and Shrub
16 – CA Steppe	California Dry Steppe

Table S1. Full names of Bailey's Ecoprovinces of the western US.

APPENDIX D: SUPPLEMENTAL MATERIAL FOR CHAPTER FIVE

Text S1: *Column-integrated relative humidity*

The column-integrated relative humidity (CRH) is computed as follows:

$$\mathrm{IWV} = \frac{1}{g}\int_{p_t}^{p_b} q\mathrm{d}p \tag{1}$$

$$\mathrm{IWV}_s(p_t) = \frac{1}{g}\int_{p_t}^{p_b} q_s\mathrm{d}p \tag{2}$$

$$\mathrm{CRH} = \frac{\mathrm{IWV}}{\mathrm{IWV}_s} \tag{3}$$

where IWV and $\mathrm{IWV_s}$ are the integrated water vapor and its saturation counterpart, g is gravitational acceleration, q and q_s are the specific humidity and its saturation counterpart, and p_b and p_t are the pressures at the bottom (surface) and top of the air column, respectively. We set p_t = 300 hPa as atmospheric water content above this level is negligible (Mo et al., 2021).

Text S2: *MSE ratio*

The MSE_{ratio} is computed as follows:

$$\mathrm{MSE}_{surf} = c_pT + L_vq + gZ_s \tag{4}$$

$$\mathrm{MSE}_{sat} = c_pT_{500} + L_vqs_{500} + gZ_{500} \tag{5}$$

$$\mathrm{MSE}_{ratio} = \frac{\mathrm{MSE}_{surf}}{\mathrm{MSE}_{sat}} \tag{6}$$

where MSE_{surf} is the surface MSE, MSE_{sat} is the saturation MSE at 500 hPa, c_p is the specific heat of air at constant pressure, L_v is the latent heat of vaporization, g is the gravitational acceleration, T and T_{500} are the temperatures at 2 meters and 500 hPa, respectively, q is the specific humidity at 2 meters, qs_{500} is the saturation specific humidity at 500 hPa, and Z_s and Z_{500}

are the geopotential heights at the surface and 500 hPa, respectively. We use the 500 hPa pressure level to represent the free troposphere following previous studies (Noyelle et al., 2023; Zhang & Boos, 2023).

Text S3: *Hyperparameter tuning*

For hyperparameter tuning, we implement a modified version of the hierarchical hyperparameter selection approach of Davenport & Diffenbaugh (2021). For each CNN, hyperparameters are sequentially tuned in pairs using a grid search that tests all parameter combinations for that pair, and for each combination we use 4-fold cross validation to evaluate model performance (Davenport & Diffenbaugh, 2021). We first tune architecture parameters including the number of convolutional filters and the number of dense layers (Figure 2b). Next, we tune the regularization parameters consisting of the L2 ("ridge") regularization factor and the dropout rate. Ridge regularization adds a penalty term to the loss function equivalent to the square of the neuron activations, thereby helping to prevent overfitting during training and improving model generalization (Belkin et al., 2019; Dagon et al., 2020; Davenport & Diffenbaugh, 2021). Dropout is a form of regularization that helps prevent overfitting by ignoring ("dropping out") a portion of neurons and their connections during training (Srivastava et al., 2014). Next, we tune the algorithm parameters consisting of the learning rate and batch size. Finally, we adjust the class weights that are applied during training. Class weights are helpful to address the class imbalance between lightning and non-lightning days at most grid cells, as CNNs could achieve high accuracy by simply predicting the minority class 100% of the time. For the minority class, weights are tested on a gradient from no class weight to the inverse of the class imbalance (Labe & Barnes, 2022).

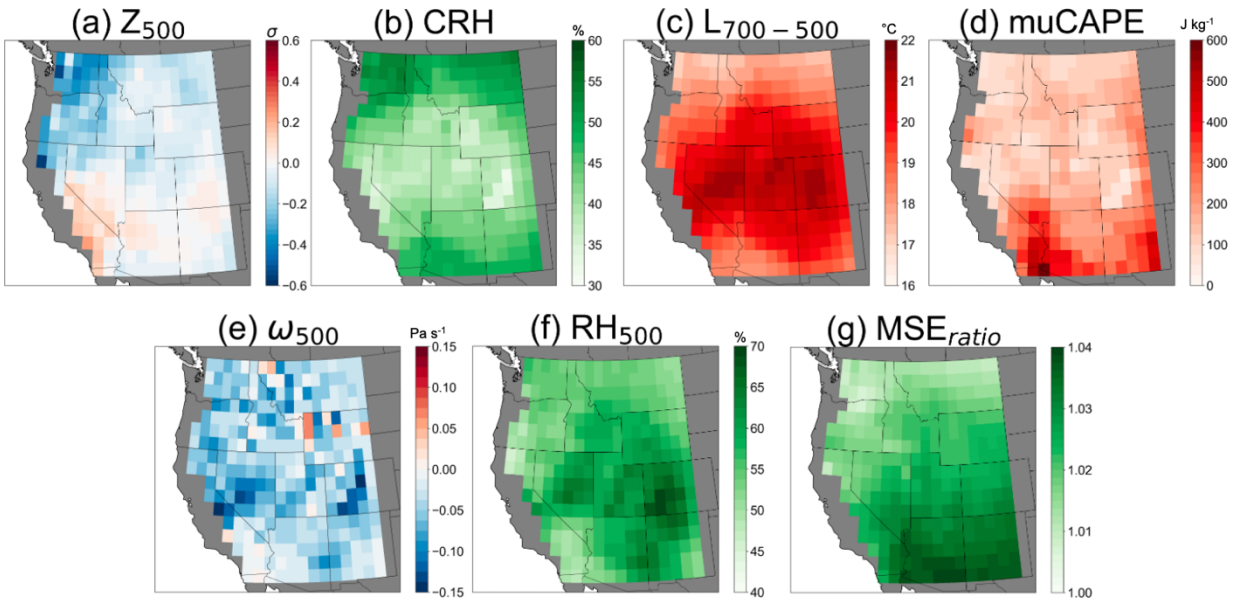

Figure S1. Composites of meteorological variables on lightning days at each 1° x 1° grid cell during June-September, 1995-2022. Differences from non-lightning days are shown in Figure 1.

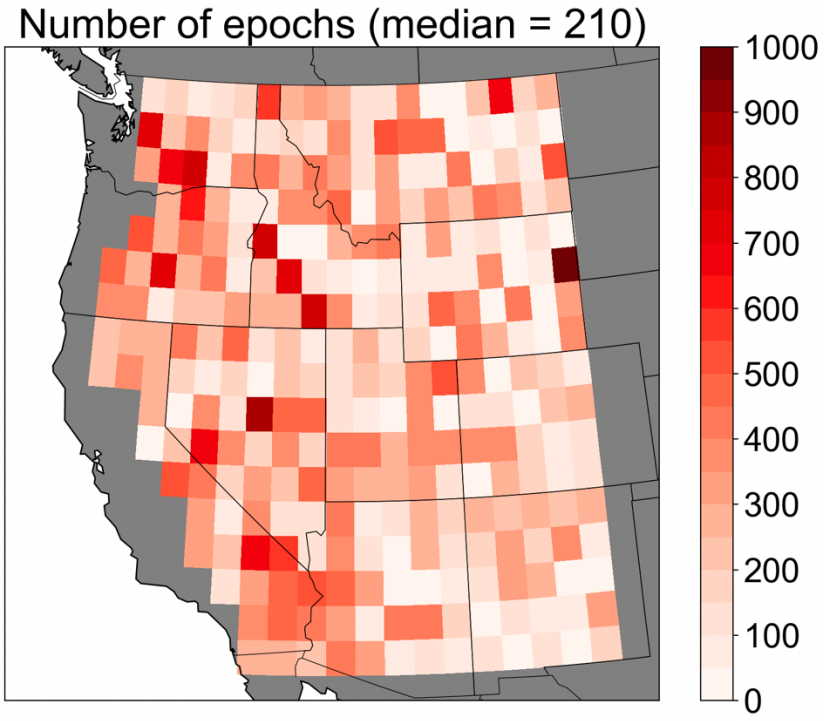

Figure S2. Number of training epochs for each CNN in 1° x 1° grid cells. The domain-median number of epochs is shown in parentheses.

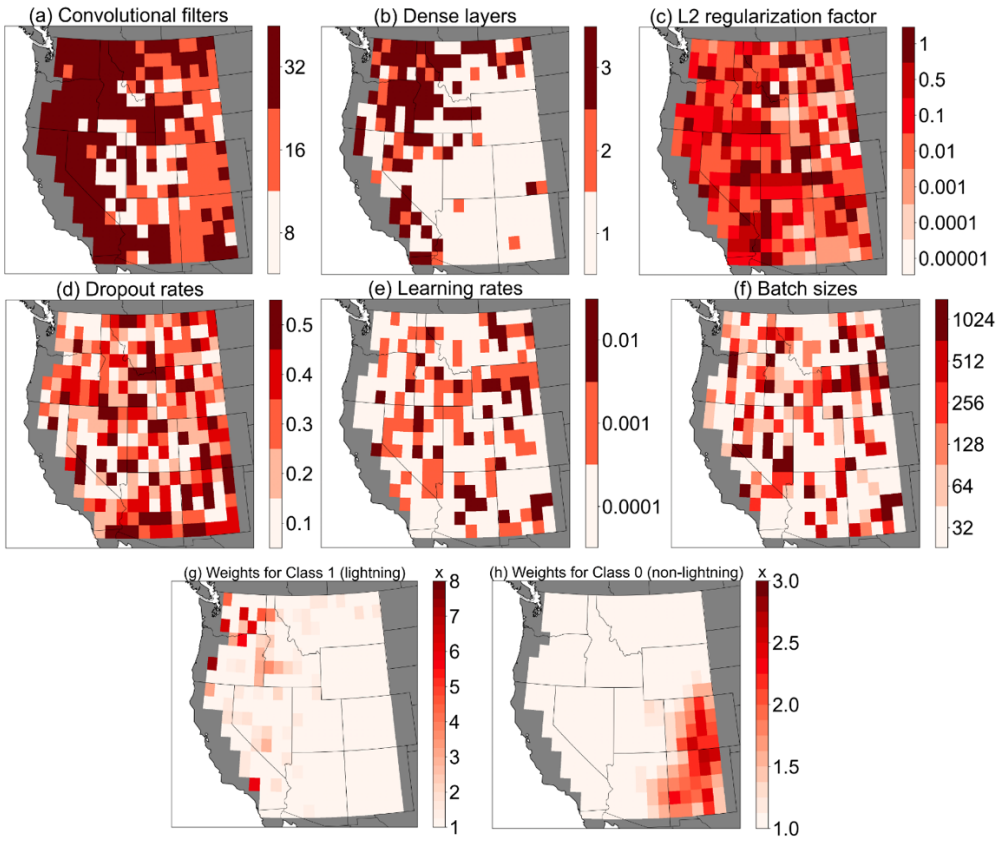

Figure S3. Tuned hyperparameters for each CNN in 1° x 1° grid cells. In (g-h), class weights represent multipliers applied to the minority class during training.

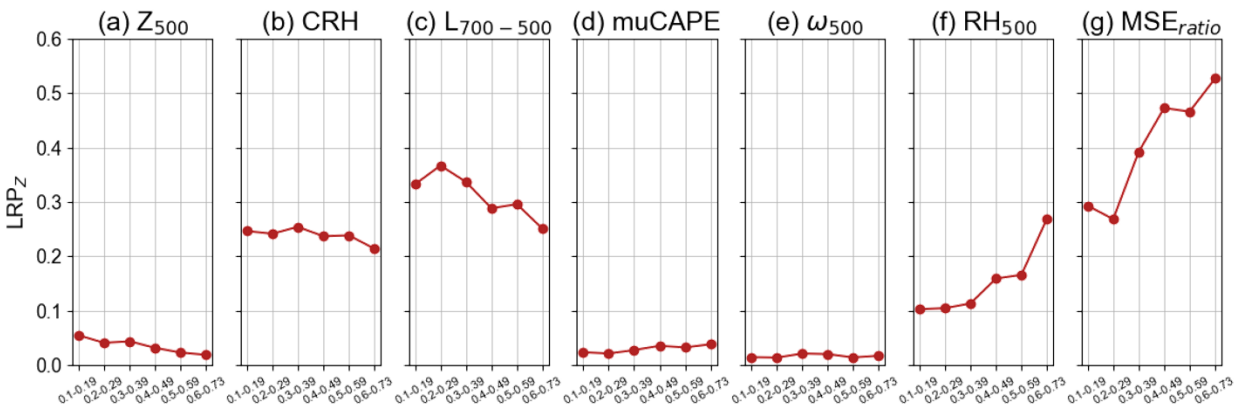

Figure S4. Mean values of maximum LRP_z binned by lightning fraction. Data corresponds to maps in Figure 3g-m.

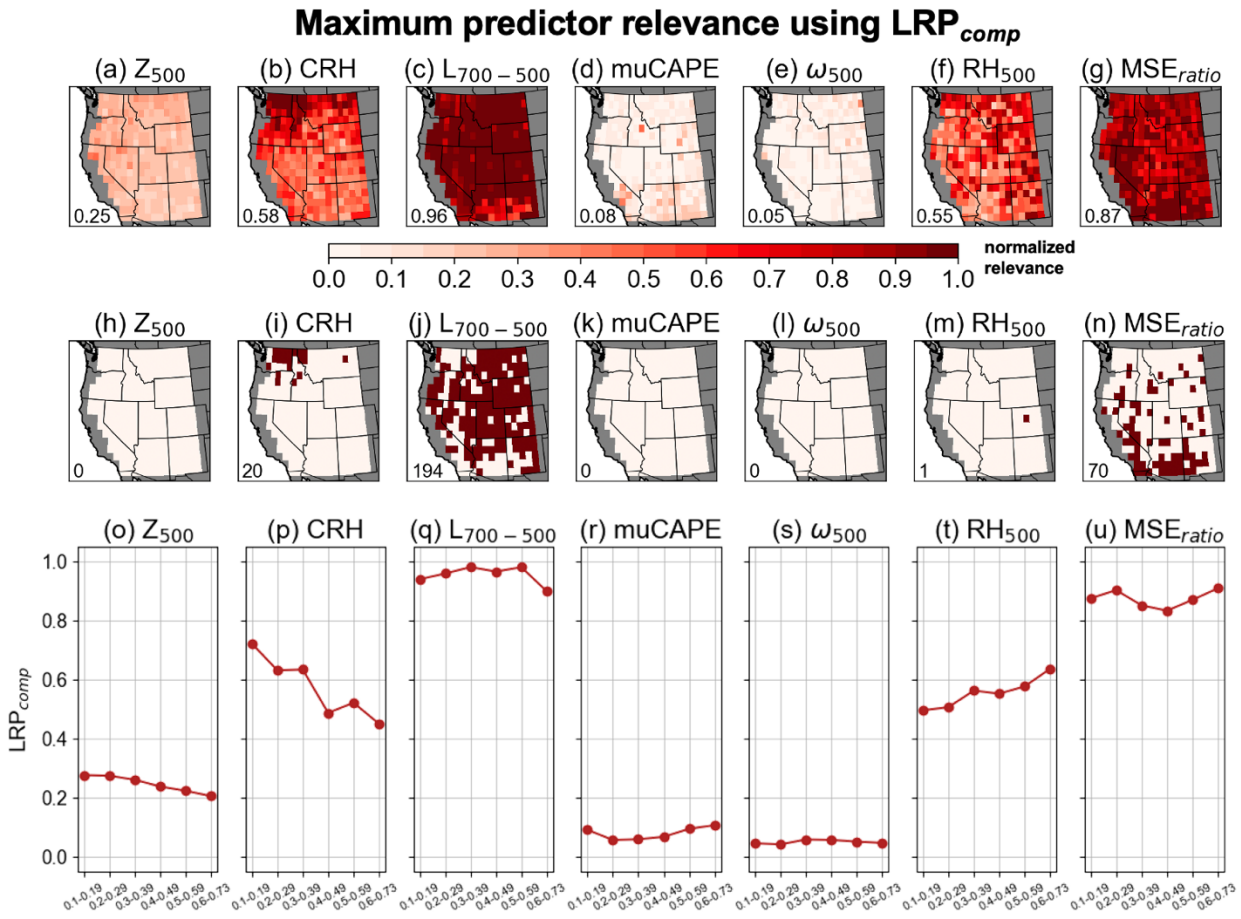

Figure S5. As in Figures 3 and S4, but using LRP$_{comp}$ for predictor relevance.

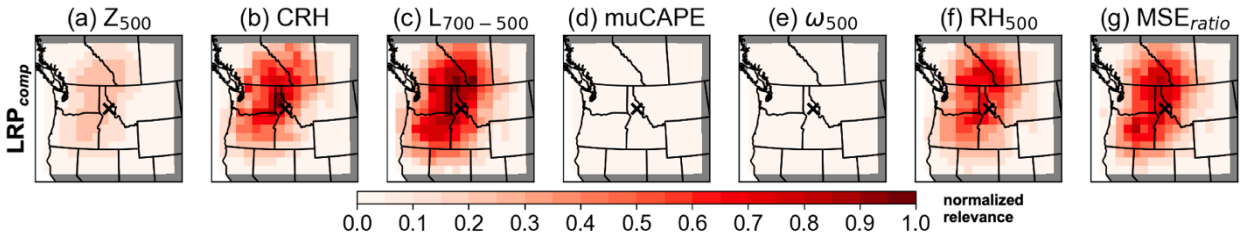

Figure S6. As in Figure 4o-u, but using LRP_{comp} for predictor relevance at example grid cell in northern Idaho (46.5N, 115.5W), denoted by black marker and shown in Figure 5 (Cell 2).

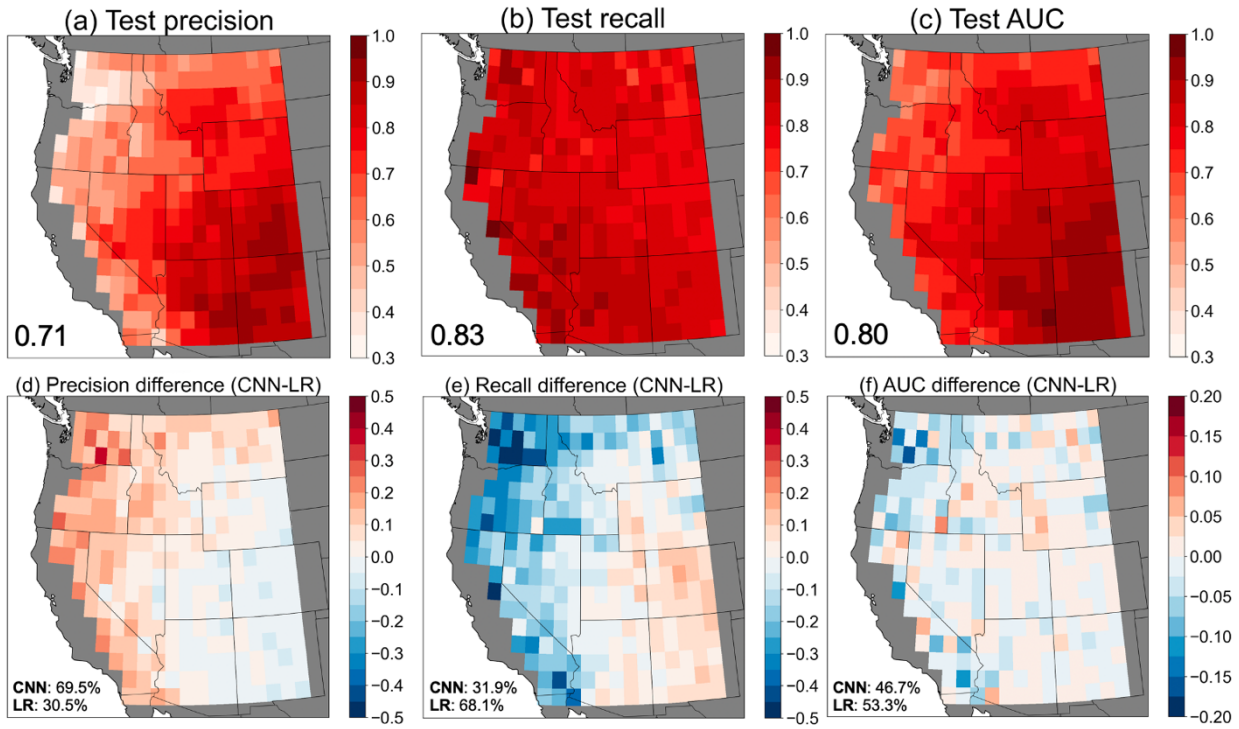

Figure S7. (a-c) Performance metrics as in Figure 3, but for logistic regression models. (d-f) Differences between CNNs and logistic regression across domain. Inset text shows the percent of grid cells that had better performance for each model and metric.

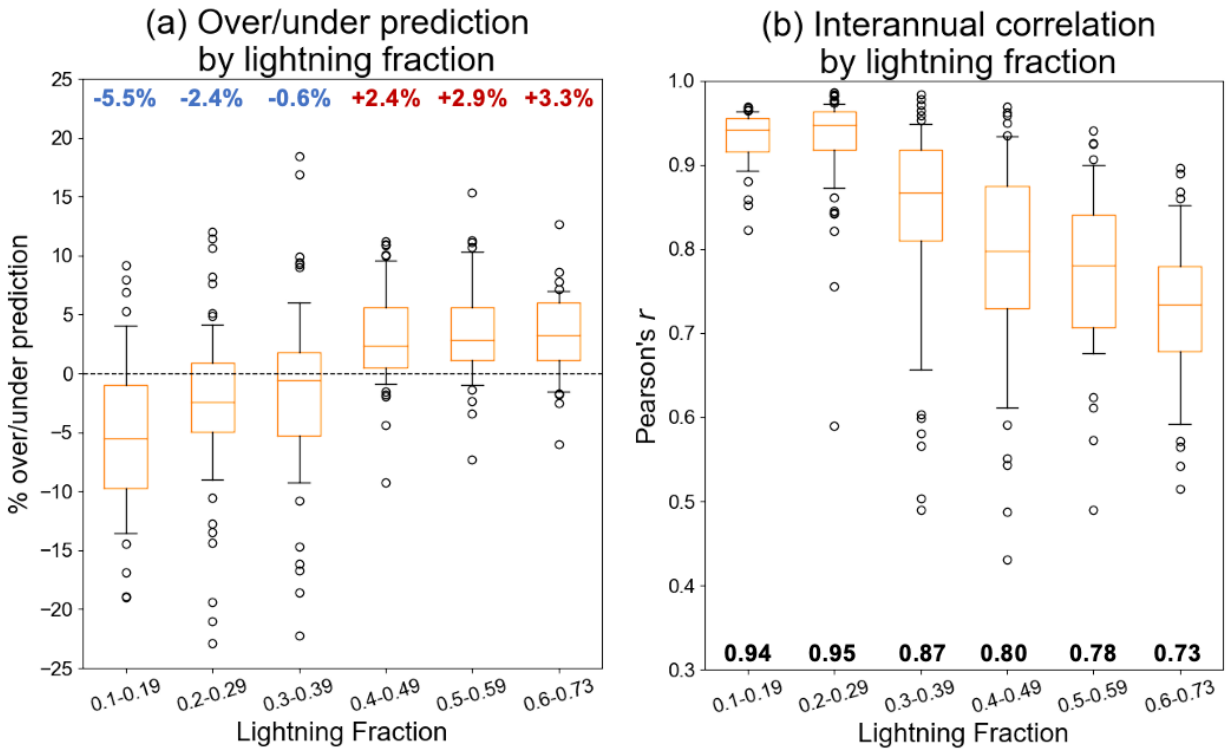

Figure S8. (a) CNN prediction error by lightning fraction with median values for each fraction bin shown above boxplots. Data corresponds to map in Figure 5b. (b) Interannual correlation by lightning fraction with median values for each fraction bin shown below boxplots. Data corresponds to map in Figure 5c.

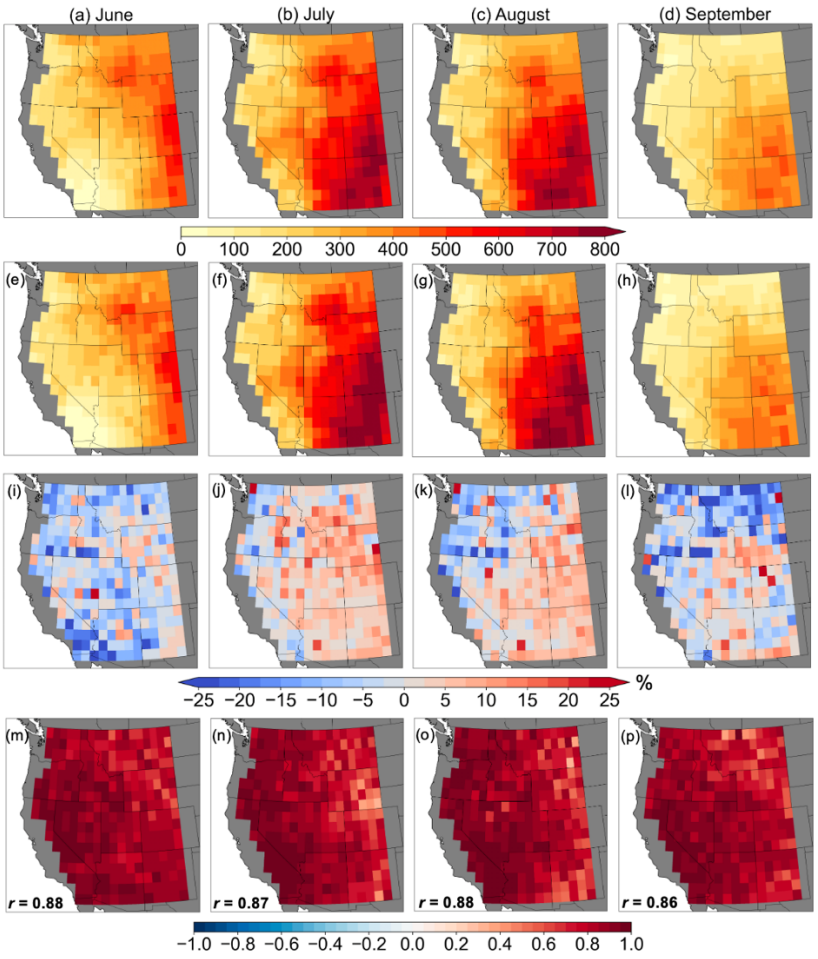

Figure S9. (a-d) For each month, the total number of observed lightning days over 1995-2022, (e-h) total number of CNN-predicted lightning days, (i-l) the corresponding prediction error compared to observations, and (m-p) interannual correlation between actual and predicted lightning days, with inset text showing domain medians for that month.

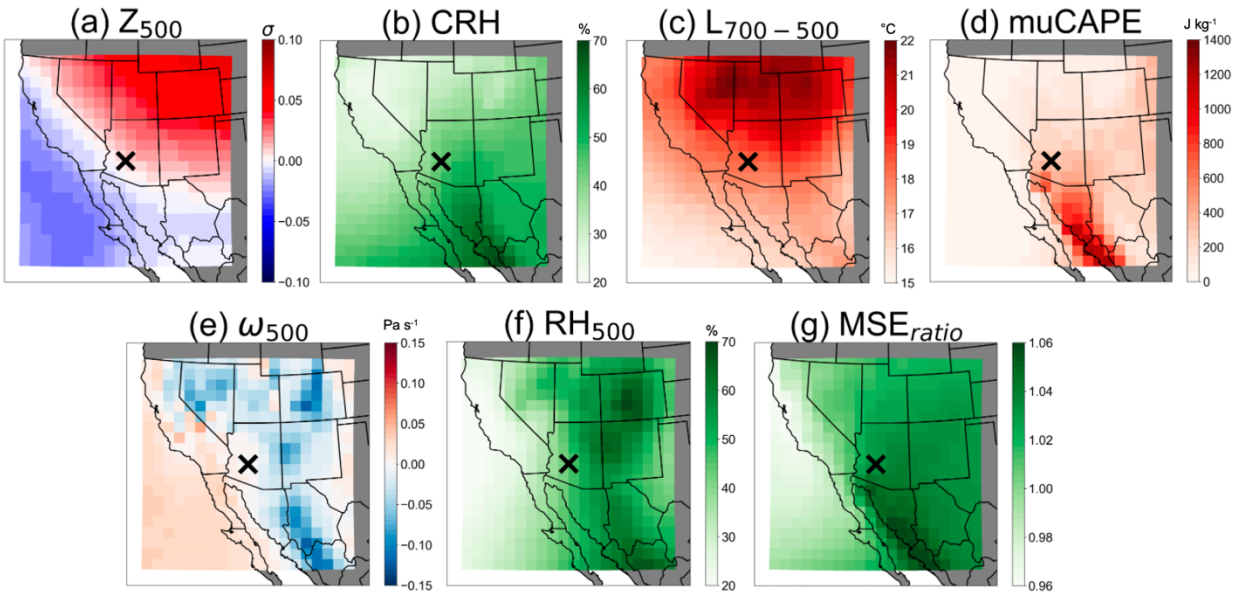

Figure S10. Composites of meteorological variables on false positive days (when lightning was predicted but did not occur) for the CNN with maximum overprediction (black marker), corresponding to the grid cell in Arizona shown in Figure 5 (Cell 4; 33.5N, 112.5W). Differences from true positive days at this grid cell are shown in Figure 6.

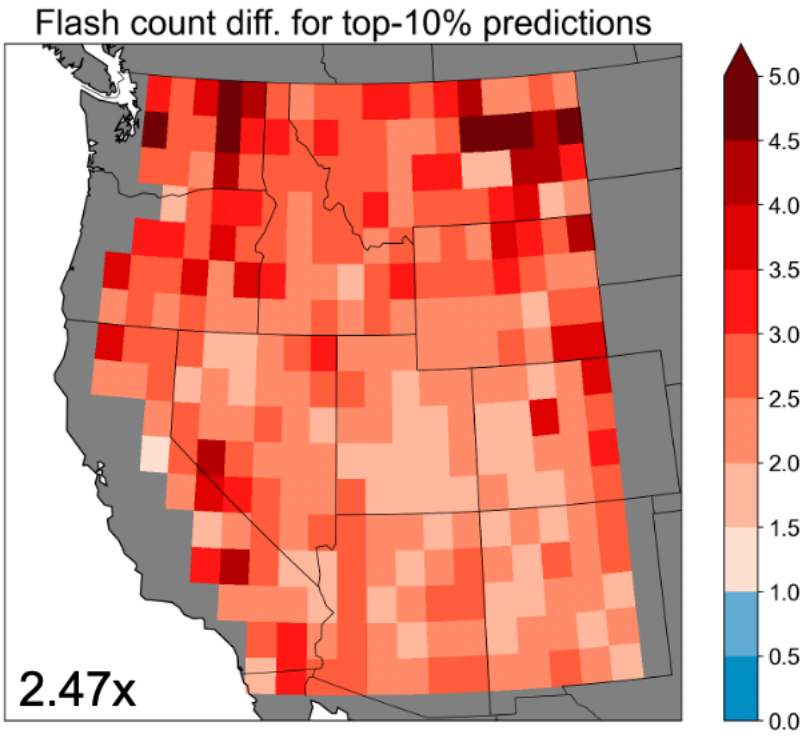

Figure S11. Enhancement of cloud-to-ground lightning flash counts for the top-10% highest probability lightning-day predictions at each grid cell, versus all other lightning-day predictions. Inset text shows domain-median enhancement.

Variable name	Variable abbreviation	Units
500 hPa geopotential height	Z_{500}	Standardized anomalies (σ)
Column-integrated relative humidity	CRH	%
700-500 hPa lapse rate	$L_{700\text{-}500}$	°C
Most unstable convective available potential energy	muCAPE	J kg^{-1}
500 hPa vertical velocity	ω_{500}	Pa s^{-1}
500 hPa relative humidity	RH_{500}	%
Ratio of surface moist static energy (MSE) to free-troposphere saturation MSE	MSE_{ratio}	Unitless

Table S1. Meteorological variables used predict the occurrence of cloud-to-ground lightning.

Hyperparameter	Values tested
Number of convolutional filters	[8,16,32]
Number of dense layers	[1,2,3]
L2 “ridge” regularization	[0.00001,0.0001,0.001,0.01,0.1,0.5,1]
Dropout rate	[0.1,0.2,0.3,0.4,0.5]
Learning rate	[0.00001,0.0001,0.001,0.01,0.1,0.5,1]
Batch size	[32,64,128,256,512,1024]
Class weights	10 equally spaced increments between 1 and the inverse of class imbalance

Table S2. Tuned hyperparameters and the range of values over which optimization is conducted.